



**PREDICTION OF FAILURE ENVELOPES OF
FOUNDATIONS USING MACHINE LEARNING
ALGORITHM AND FINITE ELEMENT LIMIT
ANALYSIS**

BY

MR. DUY TAN TRAN

**A THESIS SUBMITTED IN PARTIAL FULFILLMENT OF THE
REQUIREMENTS FOR THE DEGREE OF DOCTOR
DEPARTMENT OF CIVIL ENGINEERING
FACULTY OF ENGINEERING
THAMMASAT UNIVERSITY
ACADEMIC YEAR 2025**

**PREDICTION OF FAILURE ENVELOPES OF
FOUNDATIONS USING MACHINE LEARNING
ALGORITHM AND FINITE ELEMENT LIMIT
ANALYSIS**

BY

MR. DUY TAN TRAN

**A THESIS SUBMITTED IN PARTIAL FULFILLMENT OF THE
REQUIREMENTS FOR THE DEGREE OF DOCTOR
DEPARTMENT OF CIVIL ENGINEERING
FACULTY OF ENGINEERING
THAMMASAT UNIVERSITY
ACADEMIC YEAR 2025**

THAMMASAT UNIVERSITY
FACULTY OF ENGINEERING

THESIS

BY

MR. DUY TAN TRAN

ENTITLED

PREDICTION OF FAILURE ENVELOPES OF FOUNDATIONS USING
MACHINE LEARNING ALGORITHM AND FINITE ELEMENT LIMIT
ANALYSIS

was approved as partial fulfillment of the requirements for
the degree of Doctor of Engineering

on March 12, 2025

Chairman



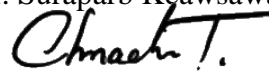
(Assoc. Prof. Cherdsak Suksiripatanapong, Ph.D)

Member and Advisor



(Assoc. Prof. Suraparb Keawsawasvong, Ph.D)

Member



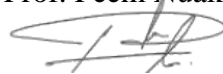
(Assoc. Prof. Chanachai Thongchom, Ph.D)

Member



(Assist. Prof. Peem Nuaklong, Ph.D)

Member



(Dr. Penpichcha Sanit-in, Ph.D)

Dean



(Prof. Dr. Sanya Mitaim, Ph.D)

Thesis Title	PREDICTION OF FAILURE ENVELOPES OF FOUNDATIONS USING MACHINE LEARNING ALGORITHM AND FINITE ELEMENT LIMIT ANALYSIS
Author	DUY TAN TRAN
Degree	Doctor of Engineering (Civil Engineering)
Major Field/Faculty/University	Civil Engineering Faculty of Engineering Thammasat University
Thesis Advisor	Assoc. Prof. Dr. Suraparb Keawsawasvong
Academic Year	2025

ABSTRACT

This thesis is concerned with the V - H - M failure envelopes for strip, ring, and conical foundations under combined loadings on anisotropic clay. The study employs the finite element limit analysis (FELA) technique and utilizes the well-established Anisotropic Undrained Shear (AUS) failure criteria. The focus of the study is on evaluating the influences of the geometric footing (r_i/r_o , β) and the anisotropic factor (r_e) on the bearing capacity of foundations subjected to external forces of vertical force (V), horizontal force (H), and moment (M). The combinations of V - H , V - M , and H - M load spaces are analyzed using dimensionless output parameters, and the various characteristics of failure mechanisms of the foundations are examined. Throughout this thesis, examining predicted foundation failure mechanisms is given importance. This research aims to take a holistic approach to foundation analysis, linking foundation capacity to the corresponding collapse mechanism in the soil to improve the understanding of foundation behavior. Alongside FELA, the study introduces an innovative machine learning approach using Artificial Neural Network (ANN) and hybrid ANN (ABC, ALO, ICA), Categorical Boosting (CATBoost), Extreme Gradient Boosting (XGBoost), and Gradient Boosting Machine (GBM) to evaluate the correlation between input parameters and their outcomes. The proposed machine learning models are rigorously verified and validated with the machine learning model,

(2)

showing exceptional agreement with numerical results, as demonstrated by an impressive R^2 value. The present study is a practical and efficient method for evaluating the 3D failure envelope of foundations on anisotropic clay under general loading conditions in $(V-H-M)$ space.

Keywords: 3D Failure envelope, Foundations, Anisotropic, Machine learning



ACKNOWLEDGEMENTS

First and foremost, I would like to thank my supervisor Assoc. Prof. Dr. Suraparb Kaewsawasvong invaluable guidance and patient advice throughout the course of this research. When I started my PhD, my supervisor endeavored to pass on some of his extensive knowledge, which has pushed me to be a better researcher and writer. I also thank my supervisor for encouraging me to enter the global PBL-CEP at Shibaura Institute of Technology in Japan, the resulting experiences have been some of my most memorable. For insight and help along the way, I would like to especially thank the Fully Funded Scholarship of the Department of Civil Engineering, Thammasat School of Engineering, Thammasat University.

My gratitude goes to my committee members for their insightful remarks and recommendations on this thesis.

The friendship and advice I received from my friends in the Research Unit in Sciences and Innovative Technologies for Civil Engineering Infrastructures, Department of Civil Engineering, Thammasat School of Engineering, Thammasat University is gratefully appreciated.

Finally, I would like to express my thanks to my family for all the support they have given me.

Duy Tan Tran

TABLE OF CONTENTS

	Page
ABSTRACT	(1)
ACKNOWLEDGEMENTS	(3)
LIST OF TABLES	(7)
LIST OF FIGURES	(8)
LIST OF ABBREVIATIONS	(15)
CHAPTER 1 INTRODUCTION	1
1.1 Background	1
1.2 Problem definition detail	4
1.3 Objective	6
1.4 Scope of study	7
1.5 Expected benefits	11
CHAPTER 2 LITERATURE REVIEW	12
2.1 Loading conditions	12
2.2 Bearing Capacity analysis	17
2.3 Capacity under combined loading	23
2.4. Anisotropic undrained shear (AUS)	29
CHAPTER 3 METHODOLOGY	32
3.1 The numerical method	32

	(5)
3.2 Machine learning approach	37
3.3 Parametric study	42
CHAPTER 4 FAILURE ENVELOPES OF STRIP FOUNDATIONS	47
4.1 Introduction	47
4.2 Problem statement	48
4.3 Methodology	51
4.3.1 Finite element limit analysis (FELA)	51
4.3.2 Artificial Neural Networks (ANNs)	52
4.4 Result and comparison	53
4.4.1 Verification	53
4.4.2 FELA result	54
4.4.3 ANN result	58
4.5 Conclusion	61
CHAPTER 5 FAILURE ENVELOPES OF RING FOUNDATIONS	62
5.1 Introduction	62
5.2 Problem statement	63
5.3 Methodology	65
5.4 Result and comparison	71
5.5 Conclusion	81
CHAPTER 6 FAILURE ENVELOPES OF CONICAL FOUNDATIONS	82
6.1 Introduction	82
6.2 Problem statement	84
6.3 Methodology	85
6.4 Result and comparison	92
6.5 Conclusion	100

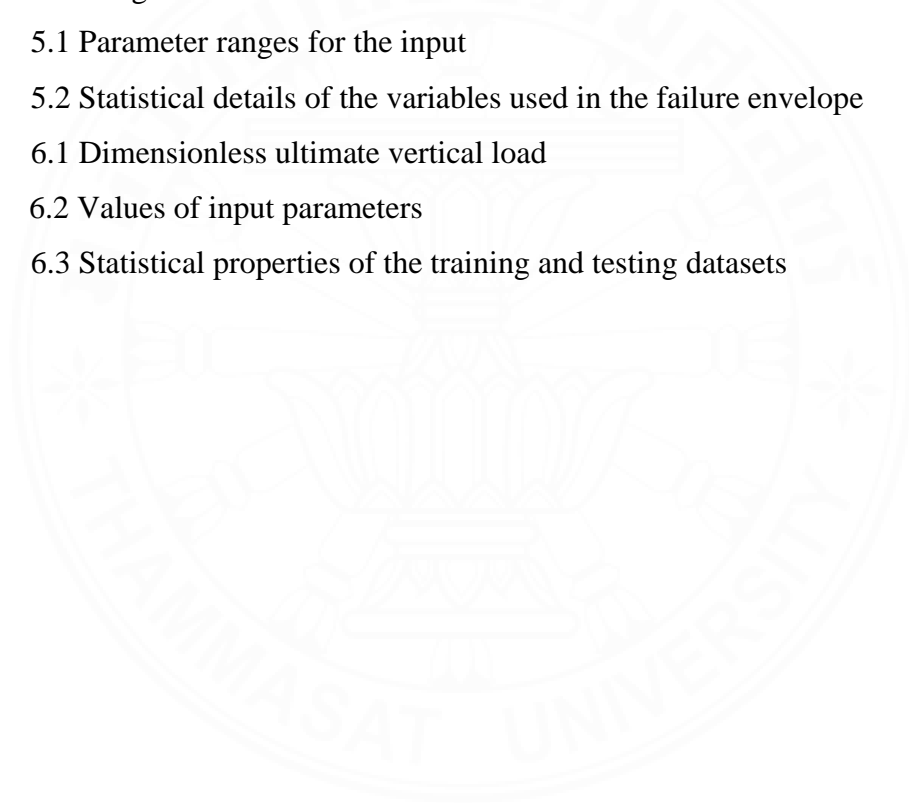
(6)

CHAPTER 7 CONCLUSION	102
7.1 Summary	102
7.2 Suggestion	103
REFERENCES	104
BIOGRAPHY	126



LIST OF TABLES

Tables	Page
3.1 Parametric studies for all cases in failure envelope of strip footing	43
3.2 Parametric studies for all cases in failure envelope of ring footing	45
3.3 Parametric studies for all cases in failure envelope of conical	46
4.1 Ranges of input parameters	52
4.2 Weights and Bias of the ANN model for full-tension cases	59
4.3 Weights and Bias of the ANN model for no-tension cases	59
5.1 Parameter ranges for the input	67
5.2 Statistical details of the variables used in the failure envelope	72
6.1 Dimensionless ultimate vertical load	86
6.2 Values of input parameters	87
6.3 Statistical properties of the training and testing datasets	90



LIST OF FIGURES

Figures	Page
1.1 The typical of offshore foundation (after Poulos, 1988)	1
1.2 A typical of gravity platform (after Eller, 1982)	2
1.3 A model of conical foundation (after Tan, 1990)	2
1.4 An example of ring foundation (after Andersen, 2005)	3
1.5 Environment force on offshore foundation (after Selnes, 1982)	5
1.6 Environmental load component in plane on offshore structure (after Tan, 1990)	6
1.7 Scope of work for failure envelope of strip footing on plain strain condition force	8
1.8 Scope of work for failure envelope of ring foundation on plain strain condition force	9
1.9 Scope of work for failure envelope of conical foundation on plain strain condition	10
2.1 Implementation of combined loading by the classical bearing equation (after Vesic, 1975)	12
2.2 Effective areas concept for shallow foundation (after Brinch Hansen, 1970)	13
2.3 V:M interaction loci deduced from traditional bearing capacity method (after Vesic, 1975)	15
2.4 Cigar shaped V-H-M failure surface (after Butterfield and Ticof, 1979)	17
2.5 Undrained triaxial test showing Mohr' circles of stress and undrained shear strength	18
2.6 Failure envelope for combined loading (after Martin, 1994)	19
2.7 Numerical swipe and probe test for strip foundation	20
2.8 Surface and embedded foundations with undrained shear strength assumption (after Tan, 1990)	21

	(9)
2.9 Tresca and von Mises failure criterion in a three-dimensional stress space	22
2.10 Normalised failure envelopes (Martin and Houlsby, 2000)	25
2.11 Failure envelope of circular footing on homogenous clay (Taiebat and Carter, 2000)	25
2.12 Comparison studies of Taiebat and Carter, 2000 with finite element result (Gourvenec, 2007)	26
2.13 Upper bound wedge scoop failure mechanisms (Gourvenec, 2003)	26
2.14 Failure envelopes for strip footing (Ukritchon, 1998)	27
2.15 Numerical result for smooth square foundation (Gourvenec et al, 2006)	28
2.16 Shaped effects on combined load failure envelopes (Gourvenec, 2007)	28
2.17 Effect of soil heterogeneity on combined load failure envelopes (Gourvenec and Randolph, 2003)	29
2.18 Typical stress-strain behaviour in triaxial compression (TC) and triaxial extension (TE)	30
2.19 Undrained strength envelopes of AUS model for different $r_e = s_{ue}/s_{uc}$ (after Krabbenhoft et al., 2019)	30
3.1 Comparison between solid and skirted footing in normally consolidated soil (Bransby and Yun, 2009)	34
3.2 Linear element used in limit analysis of upper bound (Lyamin and Sloan, 2002b)	34
3.3 Upper bound simplex strain displacement elements (Makrodimopoulos and Martin, 2007)	35
3.4 Quadrant of a failure envelope found using FEA (Bransby and Randolph, 1999)	36
3.5 Example model using OptumG2 (Krabbenhoft, 2015)	36
3.6 Example model using OptumG3 (Krabbenhoft, 2018)	37
3.7 Structure of a decision tree (Zhou et al., 2015)	38

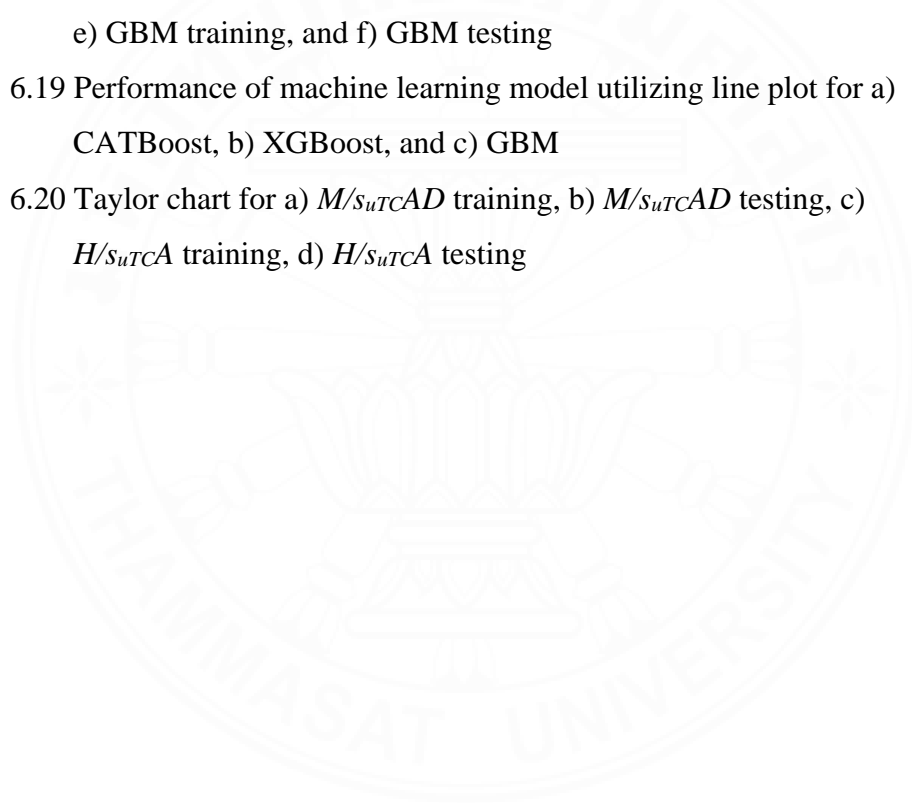
3.8 GBM algorithm calculations (Chen et al., 2022)	38
3.9 An example of the XGBoost algorithm structure	41
3.10 A typical structure and operation of ANN	41
3.11 Problem for failure envelope of strip footing	42
3.12 The typical of offshore foundation (after Poulos, 1988)	43
3.13 A numerical model of finding the failure envelope of strip footing	44
3.14 A numerical model of finding the failure envelope of ring foundation	44
3.15 Problem for failure envelope of conical foundation	45
3.16 A numerical model of finding the failure envelope of conical foundation	46
4.1 Problem definition of finding failure envelope of strip footing	48
4.2 The formations of the AUS model with various r_e values	49
4.3 3D failure envelope through dimensionless variables (V/V_0 , H/s_{uTCB} , M/s_{uTCB}^2)	50
4.4 Establishing the 2D failure envelope for a specified value of V/V_0	50
4.5 FELA model of a strip footing under general loading in OptumG2	52
4.6 An adaptive mesh pattern and boundary conditions	52
4.7 The architecture of multi-layer networks	53
4.8 The process of backpropagation	53
4.9 A comparison of determining failure envelope of strip footing in isotropic clay between the current study and the results from Ukritchon et al. (1998)	54
4.10 Failure envelope of strip footings with $r_e = 0.5$	54
4.11 Failure envelope of strip footings with $r_e = 0.6$	55
4.12 Failure envelope of strip footings with $r_e = 0.7$	55
4.13 Failure envelope of strip footings with $r_e = 0.8$	55
4.14 Failure envelope of strip footings with $r_e = 0.9$	55
4.15 Failure envelope of strip footings with $r_e = 1$	56
4.16 Examples of 3D failure envelopes	56

4.17 Failure patterns of strip footings with no-tension interface, where $V/V_0 = 0.4$	57
4.18 Failure patterns of strip footings with full-tension interface, where $V/V_0 = 0.4$	57
4.19 Examples of failure mechanisms of a strip footing	58
4.20 The Mean Square Error (MSE) and Coefficient of determination (R^2) of the number of selected hidden neurons for full-tension cases	58
4.21 The Mean Square Error (MSE) and Coefficient of determination (R^2) of the number of selected hidden neurons for no-tension cases	59
4.22 The comparison between the results of ANN predictions and FELA results for the full-tension cases	60
4.23 The comparison between the results of ANN predictions and FELA results for the no-tension cases	60
5.1 Ring foundation as an offshore structure	62
5.2 Problem definition of ring foundation under general loadings	64
5.3 Problem domain showing adaptive mesh design and boundary conditions	66
5.4 Illustration of V-H, V-M, and H-M loadings	66
5.5 Analysis of the 2D failure envelope for a given V/V_0 value	67
5.6 Examination of the failure mechanisms for H–M loading with (a) scoop, (b) scoop-wedge, (c) Brinch Hansen (1970), and (d) asymmetric wedge	68
5.7 Model architecture for an ANN (Artificial Neural Network)	69
5.8 Flow diagram showing the development of an ANN-hybrid model	70
5.9 Comparison of the results with those of existing studies on ring foundations resting on isotropic clay	72
5.10 Comparison of the V–H–M failure envelopes between the current study and those in Birid and Choudhury (2022) with (a) V–H loading, (b) V–M loading, and (c) H–M loading	72

5.11 Failure envelope under V-H loadings with (a) $r_i/r_o = 0$, (b) $r_i/r_o = 0.2$, (c) $r_i/r_o = 0.4$, (d) $r_i/r_o = 0.6$	73
5.12 Failure envelopes under V-M loadings with (a) $r_i/r_o = 0$, (b) $r_i/r_o = 0.2$, (c) $r_i/r_o = 0.4$, (d) $r_i/r_o = 0.6$	74
5.13 Failure envelope of the ring footing for combined loading analysis under H-M loading for $V/V_0 = 0.5$ and (a) $r_i/r_o = 0$, (b) $r_i/r_o = 0.2$, (c) $r_i/r_o = 0.4$, and (d) $r_i/r_o = 0.6$	74
5.14 2D diagram representation of the combined failure loads for a ring foundation with $r_i/r_o = 0.2$ and (a) $r_e = 0.5$, (b) $r_e = 0.7$, (c) $r_e = 0.9$, (d) $r_e = 1$	75
5.15 3D diagram representation of the combined failure loads for a ring foundation with $r_i/r_o = 0.4$ and (a) $r_e = 0.5$, (b) $r_e = 0.6$, (c) $r_e = 0.8$, (d) $r_e = 1$	76
5.16 3D diagram representation of the combined failure loads for a ring foundation with $r_e = 0.7$ and (a) $r_i/r_o = 0$, (b) $r_i/r_o = 0.2$, (c) $r_i/r_o = 0.4$, (d) $r_i/r_o = 0.6$	76
5.17 Failure mechanism of a 2D failure envelope of a ring foundation under general loading for $r_e = 0.9$, $r_i/r_o = 0$, and $V/V_0 = 0.75$	77
5.18 Failure mechanism of a 2D failure envelope of a ring foundation for $r_e = 0.8$, $V/V_0 = 0.5$ and (a) $r_i/r_o = 0.2$, (b) $r_i/r_o = 0.4$, (c) $r_i/r_o = 0.6$	78
5.19 Comparison of actual FELA results with those from ANN for M/s_{uTCAB} with a) train ANN-ABC, b) test ANN-ABC, c) train ANN-ICA, d) test ANN-ICA, e) train ANN-ALO, f) test ANN-ALO	79
5.20 Comparison of actual FELA results with those from ANN for H/s_{uTCA} with a) train ANN-ABC, b) test ANN-ABC, c) train ANN-ICA, d) test ANN-ICA, e) train ANN-ALO, f) test ANN-ALO	80
5.21 Taylor diagrams for a) M/s_{uTCAB} training, b) M/s_{uTCAB} testing, c) H/s_{uTCA} training, and d) H/s_{uTCA} testing	80

6.1 The application of conical foundation on ocean engineering systems	82
6.2 Problem definition of determining the failure envelope of a conical foundation subjected to general loading conditions	84
6.3 The issue area features an adaptive mesh structure and boundary limitations	86
6.4 Examination of combined loading patterns involving V-H, V-M, and H-M loadings (after Birid and Choudhury, 2022)	87
6.5 Examination of the failure mechanisms for H-M loading with (a) scoop, (b) reverse scoop, (c) slide, (d) scoop-slide	88
6.6 The architecture of the boosting models	90
6.7 Correlation heatmap for (a) M/s_{uTCAD} , (b) H/s_{uTCA}	91
6.8 Comparison of results with those by Keawsawasvong (2022) and Houlsby and Martin (2003): (a) anisotropic clay and (b) isotropic clay	92
6.9 Comparison of results with published solutions: (a) V-H loadings, (b) V-M loading, (c) H-M loading	93
6.10 The failure envelope of conical footing under V-H loadings: (a) $\beta = 180^0$, (b) $\beta = 150^0$, (c) $\beta = 120^0$, (d) $\beta = 90^0$	93
6.11 The conical footing failure envelope under V-M loadings: (a) $\beta = 180^0$, (b) $\beta = 150^0$, (c) $\beta = 120^0$, (d) $\beta = 90^0$	94
6.12 The failure envelope of conical footing under H-M loadings at $V/V_0 = 0.25$ with (a) $\beta = 90^0$, (b) $\beta = 120^0$, (c) $\beta = 150^0$, (d) $\beta = 180^0$	95
6.13 Two dimensions illustrating the collective failure loads for a conical foundation with $\beta = 150^0$ and (a) $r_e = 0.6$, (b) $r_e = 0.8$, (c) $r_e = 0.9$, (d) $r_e = 1$	95
6.14 A three-dimensional graphical depiction illustrating the combining failure loads for a conical footing with $\beta = 120^0$, and (a) $r_e = 0.5$, (b) $r_e = 0.7$, (c) $r_e = 0.8$, (a) $r_e = 1$	96

6.15 A three-dimensional graphical depiction illustrating the combining failure loads for a conical footing with $r_e = 0.6$, and (a) $\beta = 90^\circ$, (b) $\beta = 120^\circ$, (c) $\beta = 150^\circ$, (d) $\beta = 180^\circ$	96
6.16 The typical of offshore foundation (after Poulos, 1988)	97
6.17 Failure mechanism of a 2D failure envelop of the conical footing under general loading for $r_e = 0.9$, $V/V_0 = 0.5$, with (a) $\beta = 90^\circ$, (b) $\beta = 120^\circ$, (c) $\beta = 150^\circ$	98
6.18 Comparison of the FELA with those from: a) CATBoost training, b) CATBoost testing, c) XGBoost training, d) XGBoost testing, e) GBM training, and f) GBM testing	99
6.19 Performance of machine learning model utilizing line plot for a) CATBoost, b) XGBoost, and c) GBM	100
6.20 Taylor chart for a) M/s_{uTCAD} training, b) M/s_{uTCAD} testing, c) H/s_{uTCA} training, d) H/s_{uTCA} testing	100



LIST OF ABBREVIATIONS

Symbols/Abbreviations	Terms
<i>FELA</i>	Finite Element Limit Analysis
<i>ALO</i>	The artificial lion optimization
<i>ICA</i>	The imperialist competitive algorithm



CHAPTER 1

INTRODUCTION

1.1 Background

The increasing demand for oil and gas, exploration and production has moved ever more into the offshore foundations. A wide range of foundation is used in the offshore oil and gas industry and in the offshore wind industry. Offshore foundations are commonly found in clay. There are many types of offshore foundations after Poulos (1988) such as gravity, jack up, piled, compliant platform, jacket on caisson foundation (see in Figure 1.1). Reservoirs of oil and gas are located in geological structures offshore as well as onshore. The development of some offshore fields has posed huge engineering problems because of the water depth and the sometimes severe loading conditions.

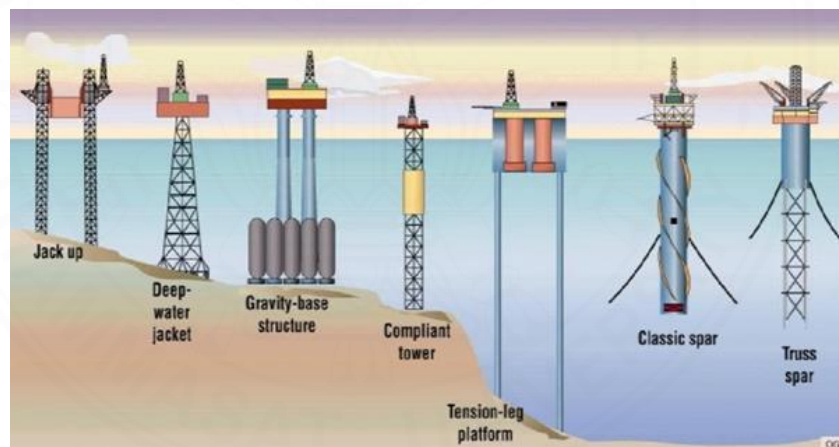


Figure 1.1 The typical of offshore foundation (after Poulos, 1988)

Figure 1.2 illustrates clearly a typical of concrete gravity platform. There are different shaped of gravity foundation such as strip footing, rectangular footing, square footing or circular footing. Gravity structures and their foundations are an order of magnitude larger than platforms previously built, and achieve stability through their own weight after Eller (1982). Gravity platform depend on their own weight to provide foundations stability against the vertical and horizontal loads imposed by the environment conditions.

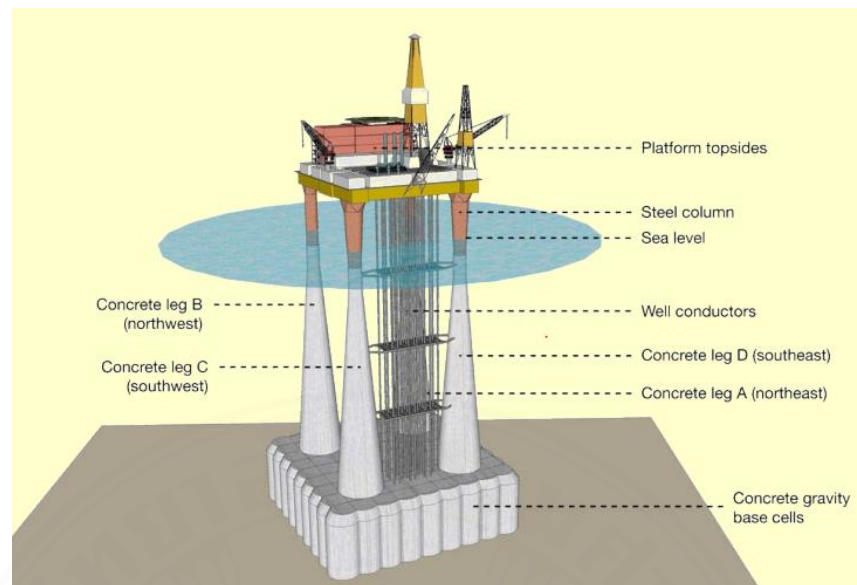


Figure 1.2 A typical of gravity platform (after Eller, 1982)

The new type foundation for the onshore wind turbine was proposed, which was called conical foundation, as shown in Figure 1.3. For the conical foundation, mainly used in mountainous areas, gravels produced during excavation can be the part of the foundation. For the isolation layer with flexible rubber in cone-shaped foundation, it can reduce bending moment acting on the foundation and the stability of superstructure can be guaranteed. The conical foundation had been successfully applied for patent in geotechnical engineering.

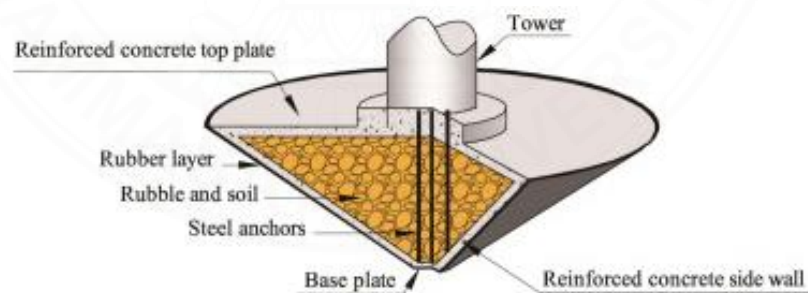


Figure 1.3 A model of conical foundation (after Tan, 1990)

Ring foundations are also widely used offshore to anchor floating structures such as spars. Foundations consists of a ring plated based attached to the jacket leg Tan (1990). The ring plated base is connected to a perimeter skirt which, when installed, penetrates into the seabed. Figure 1.4 shows an example of the ring foundations. Self-weight causes a ring to partially embed when it is lowered into position Andersen et al. (2005). The vertical and horizontal components of the mooring load can vary and

are particularly dependent on the type of mooring system, loading from catenary mooring systems is predominantly horizontal.



Figure 1.4 An example of ring foundation (after Andersen, 2005)

Offshore structures are subjected to gravity and environment loads. Gravity loads correspond to the weight of the structure and act vertically. Environmental loads consist of wave, wind and current components and laterally producing horizontal and moment loads at the foundation Poulos (1988). Offshore structures of all types are subjected to a combination of environmental forces such as waves, currents, wind and possibly earthquakes. In foundation design, it is essential to consider all types of loads that a structure will exert on the foundation. This includes vertical load, horizontal load, and bending moment load. Here is a brief explanation of each:

1) Vertical load: This refers to the downward force exerted by the weight of the structure, including its permanent elements and live loads such as people, furniture, and equipment. The foundation must be designed to withstand the vertical load, distribute it evenly over the soil, and prevent excessive settlement or heave.

2) Horizontal load: This refers to the lateral force exerted on the foundation by external factors such as wind or seismic activity. The foundation must be designed to resist horizontal loads by providing adequate lateral support, such as shear walls or bracing.

3) Bending moment load: This refers to the rotational force exerted on the foundation by uneven loads or irregularities in the structure's shape. Bending moment loads can cause the foundation to deform or crack, so it is crucial to design the foundation to resist bending moment loads by providing sufficient reinforcement and support.

Ignoring any of these loads can lead to inadequate foundation design, which can result in structural failures, such as excessive settlement, uneven foundation, or even collapse. Therefore, it is crucial to consider all types of loads, including vertical, horizontal, and bending moment loads, when designing foundations to ensure their stability, durability, and safety. The combined load is the total load that the foundation will have to support. The failure envelope helps to evaluate the combined effect of these loads and determine the maximum allowable load that the foundation can withstand without failure. By considering the failure envelope of a foundation under combined loading, structural engineers can optimize the design of the foundation to ensure its stability and safety. They can determine the appropriate dimensions, shape, and reinforcement of the foundation, as well as the most suitable soil properties and bearing capacity.

1.2 Problem definition detail

The design of offshore foundations consists of two main stages including stability analyses and deformation analyses. In the preliminary analysis of foundation stability, semi-empirical bearing capacity formulae such as Meyerhof (1956), Hansen (1970), Vesic (1975) are usually used to take into account the footing shape, footing embedment depth and the load inclination and eccentricity.

The problem with analyses using both semi-empirical formulae and rigorous finite element analyses is argued by Butterfield (1981). Butterfield (1993) further suggested an alternative approach called interaction diagrams or bearing capacity envelopes in the $V, H, M/B$ space. Note that a similar approach was suggested by Roscoe and Schofield (1956). In the same way as the yield surface is used in the plasticity theory, the bearing capacity envelope defines a boundary surface for combine load in the load space V, H, M . This approach is discussed in more detail in Chapter 2.

Another concern about the bearing capacity formulate is that they are primarily intended for use for conventional shallow foundations, while offshore foundations are subjected to large horizontal and moment loads, and sliding failure is frequently critical. The predictions of vertical, horizontal and rotational moments are usually made using either a simple hand method which employs the theory of elasticity,

the finite element method Poulos (1988). Also, there is lack of solutions for embedded or conical footings which are usually used in offshore foundations.

In addition, the usual approach does not allow accurate analyses in which the interaction between soil and structure is taken into consideration. A numerical model for the behaviour of shaped foundations on an undrained clay under combined loads based on the work hardening plasticity theory is proposed by Martin (1994). Foundations must be designed to withstand applied loads without experiencing bearing failure. The offshore environment can subject foundations to arduous loading conditions, primarily as a result of waves, wind and currents, as shown in Figure 1.5. In addition to the structural self-weight and thermally-induced axial loads. The applied loads may be two dimensional, or can be simplified as acting in plane. This enables a more straightforward plane strain assessment as shown in Figure 1.6. However, significant loading acting in three dimensions may be imposed on the foundation, leading to the application of vertical (V), horizontal (H) and moment (M) loads. In addition, applied loads may be cyclic in nature which can add further complexity (Andersen, 2009).

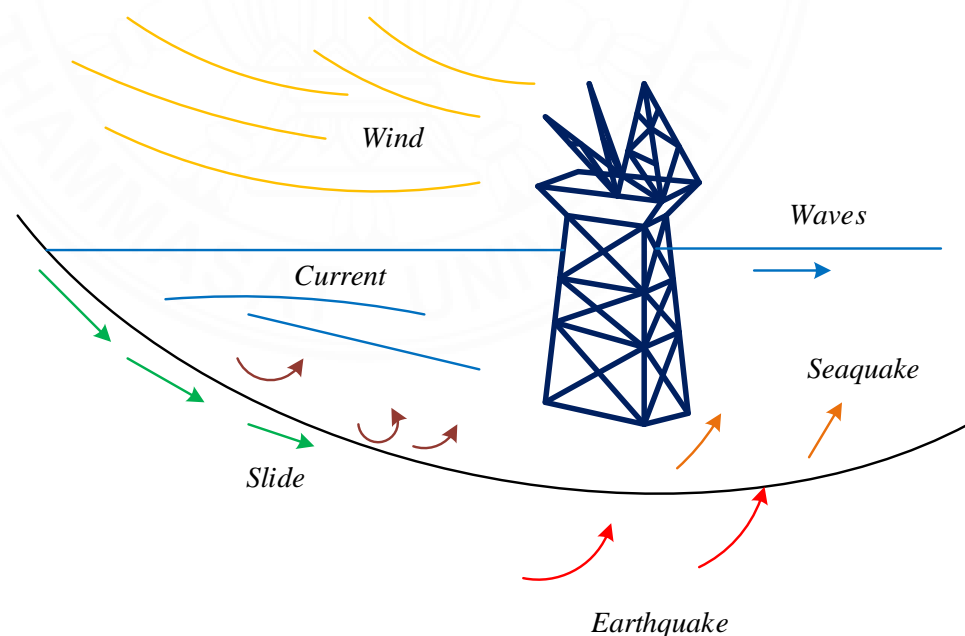


Figure 1.5 Environment force on offshore foundation (after Selnes, 1982)

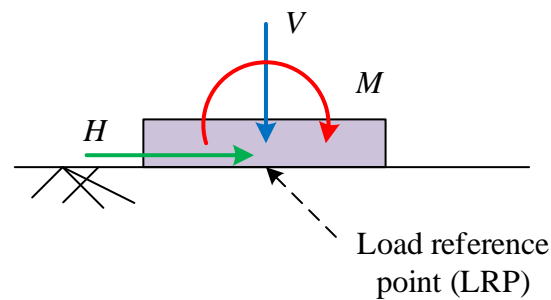


Figure 1.6 Environmental load component in plane on offshore structure (after Tan, 1990)

1.3 Objective

This thesis has used the failure envelope approach to determine the bearing capacity of regularly shaped shallow foundations such as strip, ring, and conical foundations. The focus of the research in this thesis is to examine the bearing capacity of shallow foundations under combined loading within the framework of V-H-M failure envelopes.

This thesis has taken the form of numerical analysis to explore the shape of the failure envelope and the stability of offshore foundations under combined loading. This thesis contributes to research into novel numerical modeling techniques and to research into ultimate limit state analysis of offshore foundations. More information is currently available on the implementation of 3D FELA. Thus, this research aims to describe the method and its advantages or disadvantages for foundation capacity analysis. In this thesis, OptumG2 and Optum G3 are benchmarked against analytical solutions. The application of FELA to offshore foundations is described in detail. This research demonstrates that FELA with adaptive mesh refinement is a viable preliminary design tool.

The finite element limit analysis method is used to address a wide range of problems with different boundary conditions, footing geometry, and soil profiles. The anisotropy characteristic of soil has been evaluated. The influence of design parameters such as radius ratio, interface conditions, and load angle on capacity will be quantified, and the optimal load location will be determined for an extensive range of foundations.

The most common features of offshore foundations, such as footing cone angle and embedment, are addressed.

Throughout this thesis, examining predicted foundation failure mechanisms is given importance. This research aims to take a holistic approach to foundation analysis, linking foundation capacity to the corresponding collapse mechanism in the soil to improve the understanding of foundation behavior.

In addition, the machine learning (ML) algorithm provides a potential solution to understand the complex interaction among factors that influence failure envelopes. The tools provided in this study would contribute to practical designs.

1.4 Scope of study

This thesis contains the failure envelope problem of foundations under combined loading for undrained clay with AUS criterion. The AUS criterion is anisotropic with the anisotropic strength ratio r_e .

The early chapter provide context to the analysis problems considered later in the thesis.

Chapter 2 is literature review, provides background information on the undrained analysis of foundations in soil and capacity analysis studies of shallow foundation under combined loading as well as machine learning algorithm.

Chapter 3 is methodology research, reviews of numerical techniques, the FELA implementation and discuss parametric studies.

Chapter 4, the failure envelope of strip footing under combined loading are analysis, the AUS criterion and the interface between footing and soil are considered. The effect of combined loading on failure envelopes is assessed. The failure envelope of strip footing problem in anisotropic clay for plain strain condition are defined in Figure 1.7. The analysis performs parametric studies of failure envelope of strip footing using FELA, OptumG2 Krabbenhoft et al. (2015).

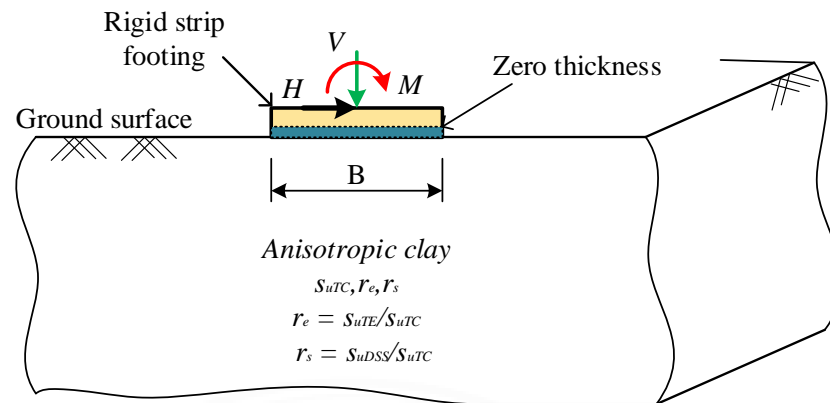


Figure 1.7 Scope of work for failure envelope of strip footing on plain strain condition force

- 1) Base width and base thickness of strip footing (B) and ($T = 0.2B$), B is assumed to be 1 unit
- 2) Anisotropic strength ratio (r_e) should be in the range of 0.5 to 1
- 3) Three anisotropic undrained shear strength obtained from triaxial compression (s_{uTC}), triaxial extension (s_{uTE}), and direct simple shear (s_{uDSS}) are the input strengths parameter.
- 4) Two anisotropic strength ratios for anisotropic clays can be defined as $r_e = s_{uTE}/s_{uTC}$ and $r_s = s_{uDSS}/s_{uTC}$
- 5) The interfaces are assumed to be full tension or no tension, where no tension means that the feature of tension cut-off is activated at the interface between soil and structure.
- 6) Combined loadings include vertical load (V), bending moment (M) and horizontal load (H).
- 7) The machine learning (ML) is also applied to build predictive models and relationships in large amounts of data that may not be immediately apparent through traditional analytical methods.

Chapter 5, the failure envelope of ring foundation under combined loading are analysis, the AUS criterion and the size of the ring foundation are considered. The effect of combined loading on failure envelopes is assessed. The failure envelope of ring foundation problem in anisotropic clay is defined in Figure 1.8. The analysis performs parametric studies of failure envelope of ring footing using finite element limit analysis.

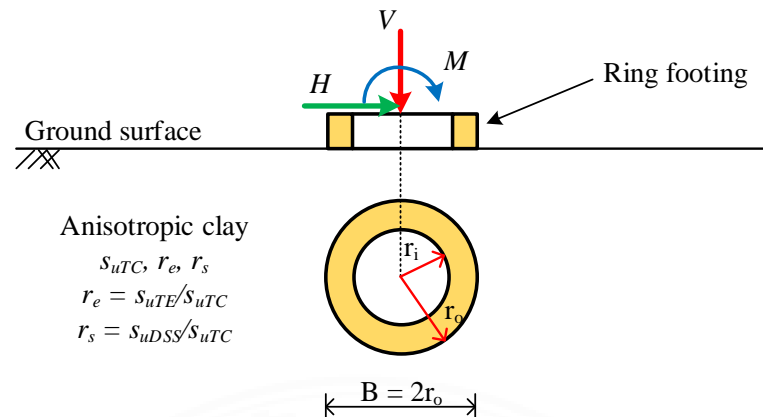


Figure 1.8 Scope of work for failure envelope of ring foundation on plain strain condition force

- 1) The ratio between internal and external radii (r_i/r_o) should be in the range of 0 to 0.6
- 2) Anisotropic strength ratio (r_e) should be in the range of 0.5 to 1
- 3) Three anisotropic undrained shear strength obtained from triaxial compression (s_{uTC}), triaxial extension (s_{uTE}), and direct simple shear (s_{uDSS}) are the input strengths parameter.
- 4) Two anisotropic strength ratios for anisotropic clays can be defined as $r_e = s_{uTE}/s_{uTC}$ and $r_s = s_{uDSS}/s_{uTC}$
- 5) The interface between the bottom of the ring foundation and the soil was assumed to be fully rough, ensuring complete bonding between the footing and the soil.
- 6) Combined loadings include vertical load (V), bending moment (M) and horizontal load (H).
- 7) The machine learning (ML) is also applied to build predictive models and relationships in large amounts of data that may not be immediately apparent through traditional analytical methods.

Chapter 6, the failure envelope of conical foundation under combined loading are analysis, the AUS criterion and the cone apex angle varies by adjusting cone height while keeping the footing diameter constant are considered. The effect of combined loading on failure envelopes is assessed. The failure envelope of conical foundation problem in anisotropic clay for plain strain condition are defined in Figure 1.9. The analysis performs parametric studies of failure envelope of conical foundation using finite element limit analysis.

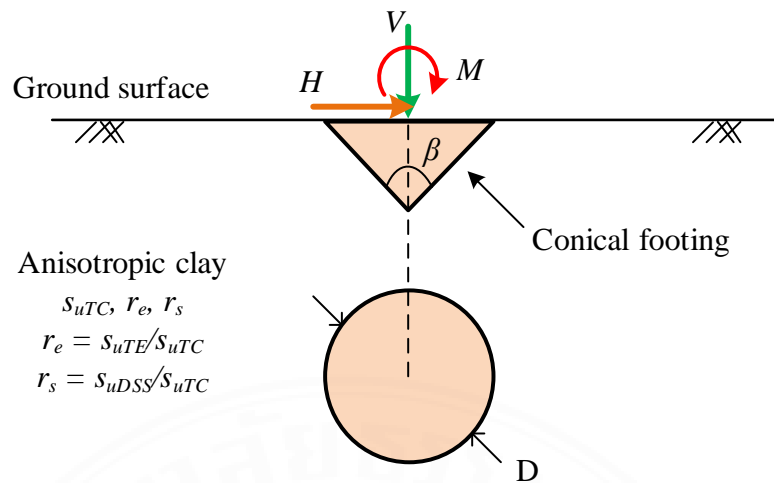


Figure 1.9 Scope of work for failure envelope of conical foundation on plain strain condition

- 1) A variable cone apex angle (β) ranging from 90^0 to 180^0
- 2) Anisotropic strength ratio (r_e) should be in the range of 0.5 to 1
- 3) Three anisotropic undrained shear strength obtained from triaxial compression (s_{uTC}), triaxial extension (s_{uTE}), and direct simple shear (s_{uDSS}) are the input strengths parameter.
- 4) Two anisotropic strength ratios for anisotropic clays can be defined as $r_e = s_{uTE}/s_{uTC}$ and $r_s = s_{uDSS}/s_{uTC}$
- 5) The interface between the bottom of the ring foundation and the soil was assumed to be fully rough, ensuring complete bonding between the footing and the soil.
- 6) Combined loadings include vertical load (V), bending moment (M) and horizontal load (H).
- 7) The machine learning (ML) is also applied to build predictive models and relationships in large amounts of data that may not be immediately apparent through traditional analytical methods.

Chapter 7 will discuss and conclusion about the failure envelope of foundation under combined loading as well as the effect of soil anisotropic. The use of machine learning in predicting the failure envelope of foundations can help engineers to make more informed decisions about foundation design and construction, ultimately leading to safer and more reliable structures. In regards to the machine learning model applications, machine learning models were used to build realistic engineering tools for

the construction of failure envelopes in both two dimensions ($H-M$) and three dimensions (V, H , and M). Comparisons among the boosting models have demonstrated that machine learning is the most efficient method in predicting the 3D failure envelope of foundations on anisotropic clay under combined loadings ($V-H-M$), achieving high accuracy. It is important to emphasize that this thesis focuses on the failure envelope capacity of foundations due to the absence of design equations predicting the failure envelope of footings using machine learning methods. Failure envelopes of strip, ring and conical foundations in anisotropic clay under general loadings ($V-H-M$) have been effectively studied in this thesis using advanced finite element limit analysis (FELA) as well as the machine learning methods of ANN, ANN-ICA, ANN-ALO, ANN-ABC, CATBoost, XGBoost and GBM. It further enables the establishment of a failure envelope for footings under combined loading conditions, which can be valuable for practitioners in the field. The present study underscores the novelty and importance of its significance in foundation designs.

1.5 Expected benefit

The numerical model may be used to examine the failure envelope of foundations, the stability of foundations, the extent failure in the event of a collapse.

Designed charts, tables and equation are represented by an interaction diagram in the $V-H-M$ space consisting of dimensionless variables using the concept of dimensional analysis to predict the failure envelope of foundations.

To instruct by applying finite element limit analysis in software to address the failure envelope problems under differences soil media.

The machine learning algorithms demonstrate promising results in terms of predictive accuracy, resilience, and computational efficiency across various practical scenarios, enabling the establishment of a failure envelope for foundations under combined loading conditions (vertical, horizontal, and moment), which can be valuable for practitioners assessing the capacity of foundations under combined loading conditions.

CHAPTER 2

LITERATURE REVIEW

2.1 Loading conditions

2.1.1 Central vertical loading

There are only a few specific bearing capacity problems for which analytical solutions have been derived. Prandtl (1921) solved the problem of a strip footing on a weightless, perfectly plastic material. The axisymmetric case was solved by Shield (1955) for a Tresca material and by Cox et al. (1961) for a weightless Mohr-Coulomb material. Cox (1962) extended the solution of Cox et al. (1961) to include Mohr-Coulomb material with self-weight, but results were not generated for a wide range of friction angle values. Terzaghi (1943) used the results of Prandtl to develop the well-known semi-empirical bearing capacity formula for shallow strip footings.

A number of assumptions are made in the solution of the bearing capacity problem. The foundation material is assumed to be rigid perfectly plastic (shown in Figure 2.1).

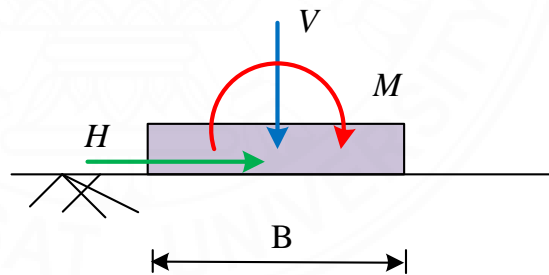


Figure 2.1 Implementation of combined loading by the classical bearing equation
(after Vesic, 1975)

Investigations by Tan (1990) led to similar conclusions but differences were detected for the case of sharp cones on dense sand. The finite element method has been used to predict bearing capacity loads, failure envelopes and in some cases the results have been in agreement with traditional bearing capacity predictions by Griffiths (1982), Simonini (1993), Gourvenec (2007).

2.1.2 Combined loading – Vertical: Horizontal failure surface

Combinations of vertical and horizontal load can be modelled as a single load, with an inclination angle α to the vertical, acting at the centre of the footing as shown in Figure 2.2. Meyerhof (1953) noted that the bearing capacity reduced to zero and that sliding failure occurred when the inclination angle approached the soil-footing friction angle. The following relationship, which describes a V - H failure surface for a circular footing on sand, can be deduced from Meyerhof's formulae as

$$\frac{V}{V_m} = \left[1 - \frac{\tan^{-1}(H/V)}{\phi} \right]^2 \quad (2.1)$$

where V is the vertical load, V_m is the bearing capacity under a central load, H is the horizontal load, and ϕ is the friction angle of the sand. Corresponding relationships can be derived from Brinch Hansen's bearing capacity formula

$$\frac{V}{V_m} = \frac{1}{3} \left[5 - \left(1 - 0.7 \frac{H}{V} \right)^5 \right] \left(1 - 0.7 \frac{H}{V} \right)^5 \quad (2.2)$$

and from Vesic formula

$$\frac{V}{V_m} = \left[1 - \frac{H}{V} \right]^{5/2} \quad (2.3)$$

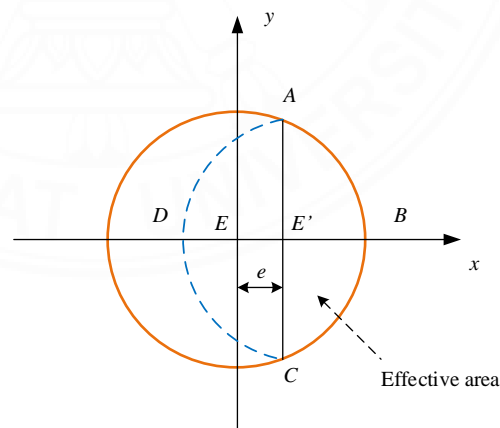


Figure 2.2 Effective areas concept for shallow foundation (after Brinch Hansen, 1970)

Tan (1990) investigated the V - H failure surface of flat circular and conical footings using a geotechnical centrifuge apparatus. Tan's tests were performed on medium dense and loose sand at w/R ratios of 0.2 to 1.8. Tan (1990) normalised the results by the maximum vertical load previously experienced by the footing. Tan (1990)

found that a $V-H$ failure surface, for a particular ratio of w/R , could be traced in one test by subjecting a footing to a horizontal displacement whilst maintaining a constant vertical displacement.

Martin (1994) performed a comprehensive series of the displacement- controlled tests in which the combined load failure surface of a spudcan footing on clay was defined. His sideswipe tests indicated that h_0 was equal to 0.127 at a V/V_0 value of 0.464. As with Tan (1990), Martin used V_0 values to normalise his results since his sideswipe tests were performed on a soft material.

2.1.3 Combined loading – Vertical: Moment failure surface

The bearing capacity of footings subjected to vertical and moment loads has traditionally been calculated using the statically equivalent eccentric load and effective area concept that is shown in Figure 2.1 and 2.2. The following $V-M$ interaction equation can be derived using the aforementioned procedure in combination with Meyerhof (1963) method.

$$\frac{V}{V_m} = \frac{A'B'}{AB} \left[\frac{1 + 0.1 \tan^2(45 + \phi/2)(B'L')}{1 + 0.1 \tan^2(45 + \phi/2)} \right] \quad (2.4)$$

where the prime indicates an effective dimension. Moment load is incorporated into Equation 2.4 via the effective dimensions that are functions of the load eccentricity. A similar equation can be deduced using the methods of Brinch Hansen (1970) and Vesic (1975),

$$\frac{V}{V_m} = \frac{A'B'}{3AB} \left[5 - 2 \frac{B'}{L'} \right] \quad (2.5)$$

Normalised failure surfaces obtained using Equations 2.4-2.5 are compared in Figure 2.3. The curves are all approximately parabolic and thus similar to the $V-H$ failure surfaces. The most notable difference being the lower magnitude of the peak normalized moment load as compared to that in $V-H$ space. Ingra and Baecher (1983) suggest a relationship for an eccentricity factor based on statistical analysis of available data. Their method predicts a peak normalized moment load of 0.084 at $V/V_m = 0.446$. This is greater than that predicted by the methods shown in Figure 2.3. It is widely accepted that the equivalent area method is conservative. Most of the researchers

mentioned in the previous review of V - H surfaces also addressed the V - M problem. The main difference between V - M and V - H surfaces being the smaller size of the V - M surfaces, when normalized by V , and using the $M/2R$ convention.

$$\frac{m}{m_0} = 4\nu(1-\nu) \quad (2.6)$$

where $m = M/2RV$, and m_0 is the peak normalised moment load. Butterfield and Ticof (1979) found that a peak normalised moment load of 0.1, occurring at $V/V_m = 0.5$, was representative of model footing tests on sand. Recent research conducted by Butterfield and Gottardi (1994) and Montrasio and Nova (1997) on strip footings suggests a lower peak value of 0.0875. Montrasio and Nova (1997) also found that the size of the normalised failure surface increased with footing embedment and suggested that $m_0 = 0.125$ at $w/R = 1$. Sand density and footing roughness were found not to affect the V - M failure surface.

$$m_0 = -0.039 \ln \left(\frac{V_{0i}}{V_m} \right) + 0.07 \quad (2.7)$$

The V - M sideswipe tests of Gottardi and Houlsby (1995) shown that the changes in the vertical displacement that occurred during the sideswipe tests are accounted for in the values of V_0 . The peak normalised moment load seems to be dependent on the value of V_0 . This is consistent with V - H behaviour. The following expression is used to fit the V_0/V_m data.

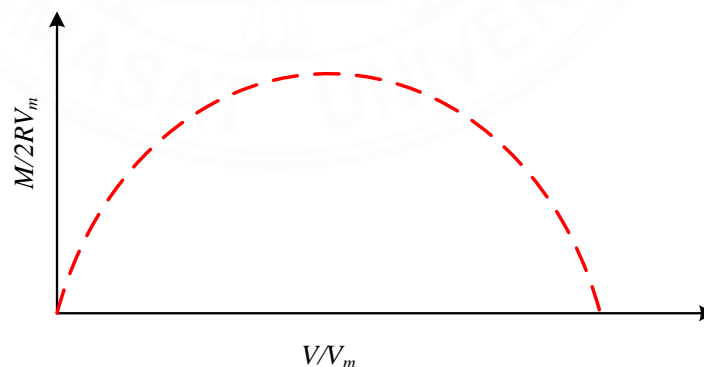


Figure 2.3 V:M interaction loci deduced from traditional bearing capacity method
(after Vesic, 1975)

2.1.4 Combined loading – Vertical: Horizontal: Moment failure

The V - H - M problem can be modeled using the traditional bearing capacity methods and an equivalent inclined load centred on a reduced footing area as shown in Figure 2.2 and described in Meyerhof (1963) method may be used to derive the following V - H - M failure surface.

$$\frac{V}{V_m} = \frac{A'B'}{AB} \left[\frac{1 + 0.1 \tan^2(45 + \phi/2)(B'L')}{1 + 0.1 \tan^2(45 + \phi/2)} \right] \left[1 - \frac{H}{V} \right] \quad (2.8)$$

Similarly, the theory of Brinch Hanse, (1970) gives

$$\frac{V}{V_m} = \frac{A'B'}{3AB} \left[5 - 2 \left(1 - 0.7 \frac{H}{V} \right)^5 \frac{B'}{L'} \right] \left(1 - 0.7 \frac{H}{V} \right) \quad (2.9)$$

And theory of Vesic (1975) gives,

$$\frac{V}{V_m} = \frac{A'B'}{3AB} \left[5 - 2 \frac{B'}{L'} \right] \left(1 - \frac{H}{V} \right)^{m+1} \quad (2.10)$$

It should be noted that Equations 2.8-2.10 are only valid in the 1 and 3 quadrants of H - M space. The degrading effect that a horizontal load has on the moment capacity at $V/V_m = 0.5$, and vice versa, is evident.

Butterfield and Tiof (1979) used the results of numerous combined load tests of strip footings on sand to derive parabolic shaped V - H and V - M surfaces. They also postulated a cigar shaped V - H - M surface as shown in Figure 2.4. The cigar shaped V - H - M failure surface has been verified by Georgiadis and Butterfield (1988) and Nova and Montrasio (1991) for strip footings on sand, and by Dean et al. (1992) for conical footings on sand. Butterfield and Gottardi (1994) and Gottardi et al. (1997) have since verified the applicability of a cigar shaped failure surface to both positive and negative combinations of horizontal and moment load, for strip and circular footings respectively.

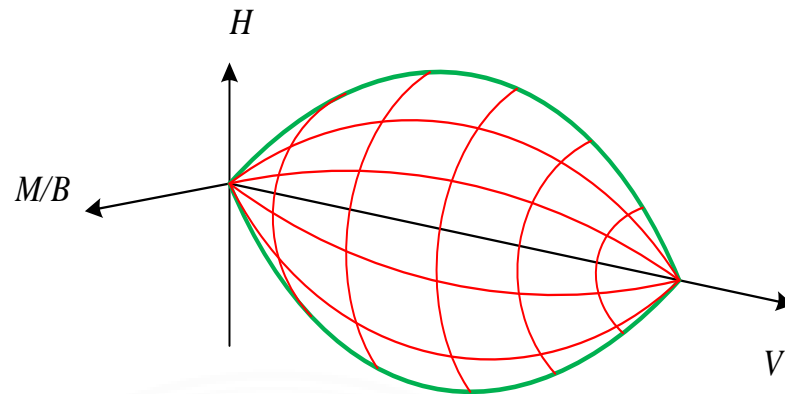


Figure 2.4 Cigar shaped V-H-M failure surface (after Butterfield and Ticof, 1979)

2.2 Bearing Capacity analysis

2.2.1 Theory of bearing capacity

Capacity analysis is undertaken in order to find the maximum load or combinations of loads that can be applied to a foundation before the soil is expected to fail in shear. For the analysis of offshore foundations, consideration must be given to the rate of load application when compared with the rate of water movement in the soil, as this will determine whether the response of the soil is likely to be drained or undrained. Clays and silts, commonly found in deep waters and considered in this study, typically have low permeability. When foundation loading is sufficiently rapid, it can be assumed that the soil remains undrained for foundation capacity analysis, such that a total stress analysis is appropriate and the undrained shear strength s_u is the governing soil strength parameter.

Interface shear strength and tension capacity need consideration at foundation/soil boundaries. In undrained capacity analysis the available shear strength at an interface is commonly modelled as a roughness factor, αs_u . A fully rough foundation can utilize the full shear strength of the adjacent soil, $\alpha = 1$ while a fully smooth foundation has no shear resistance at the interface, $\alpha = 0$. This can be achieved by imposing a tension cut-off on the interface.

Undrained triaxial tests can be undertaken on clay samples to determine undrained shear strength. In this test, a confining pressure is applied to

cylindrical sample of soil with cross sectional area. Axial loading is then applied to the sample until failure occurs.

$$s_u = \frac{\sigma_1 - \sigma_3}{2} \quad (2.11)$$

For an unconsolidated undrained test, the undrained shear strength is not dependent on the confining pressure and typically a series of tests at a range of confining pressures are undertaken to estimate s_u , shown in Figure 2.5. In situ tests can also be used to find s_u , such as the shear vane test or more commonly offshore, the cone penetration test CPT.

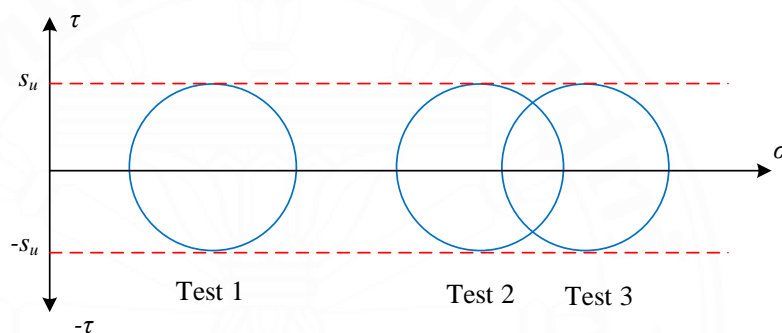


Figure 2.5 Undrained triaxial test showing Mohr' circles of stress and undrained shear strength

Shallow foundation bearing capacity is commonly assessed using a modified version of the classical Terzaghi bearing capacity equation Terzaghi (1943). The soil is assumed to act as a rigid-plastic Mohr-Coulomb material in drained conditions, or as a rigid-plastic Tresca material in undrained conditions. With the inclusion of these factors, the ultimate capacity q_u for a footing of width B is given by

$$q_u = cN_c s_c d_c i_c + qN_q s_q d_q i_q + 0.5\gamma B N_\gamma s_\gamma d_\gamma i_\gamma \quad (2.12)$$

where N_c , N_q and N_γ are bearing capacity factors corresponding to cohesion c , surcharge pressure at footing level q , and soil unit weight below footing level γ . The bearing capacity factors are each a function of the friction angle, ϕ . Equation 2.12 is written in a general form and can be applied to assess both drained and undrained capacity.

In Equation 2.12 the shape and depth modification factors are given by s_q , s_γ , s_c and d_c , d_q , d_γ respectively. Load inclination modification factors, i_q , i_γ and i_c

are used to account for the effects of horizontal loading. Several different expressions for the modification factors have been proposed, including those by Meyerhof (1953), Brinch Hansen (1970) and Vesic (1973).

2.2.2 Failure envelopes

An alternative to the classical bearing capacity equation is to consider bearing capacity directly within a three-dimensional V - H - M load space by defining the envelope of the failure surface in this space (see in Figure 2.6). The failure envelope shows how the foundation capacity varies with different loading combinations. Load combinations located on or outside the envelope result in foundation failure, whilst load combinations within the envelope can be considered stable.

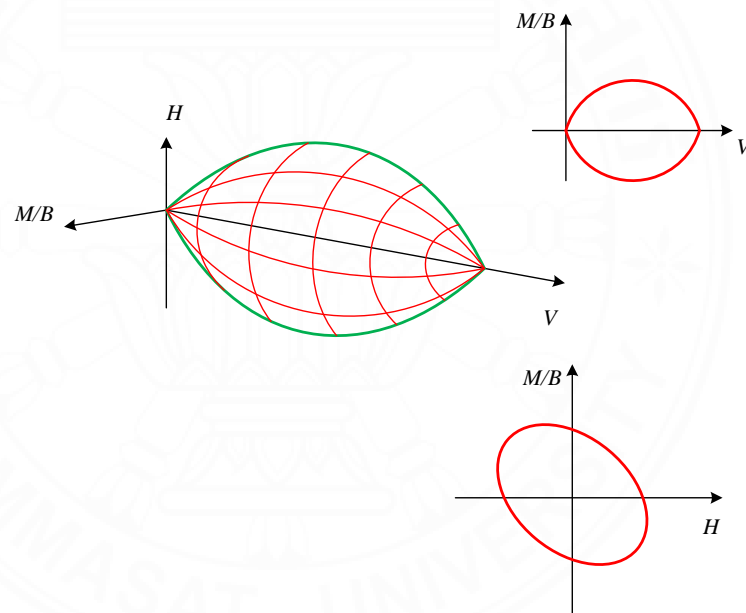


Figure 2.6 Failure envelope for combined loading (after Martin, 1994)

A number of studies have been undertaken to investigate the shape of the failure envelope for strip and circular footings on both clay and sand. Failure envelopes for foundations on clay have been determined by fitting curves to experimental results, or by using numerical or theoretical techniques Martin (1994), Murff (1994), Bransby and Randolph (1998), Ukritchon et al. (1998), Taiebat and Carter (2000), Gourvenec and Randolph (2003), Gourvenec (2007). Failure envelopes for foundations on sand have mostly been derived based on experimental results Nova and Montrasio (1991), Butterfield and Gottardi (1994), Gottardi et al. (1999), Byrne

(2000). The form of failure envelopes has generally been found to be approximately parabolic in the $H:V$ and $M/B:V$ load space, and elliptical in the $M/B:H$ load space (Figure 2.6). The elliptical $M/B:H$ failure envelope for clay has been found to have a positive eccentricity (as defined by the sign convention shown in Figure 2.6) whilst for sand the eccentricity has been shown to be negative.

The shape of failure envelopes can be defined experimentally or numerically using swipe tests, displacement-controlled probe tests, or load-controlled probe tests. An illustration of exploring the failure envelope numerically using these approaches is given in Figure 2.7. This figure shows finite element analysis results in the V - H load space for a rough strip footing of width B (Bransby and Randolph, 1998).

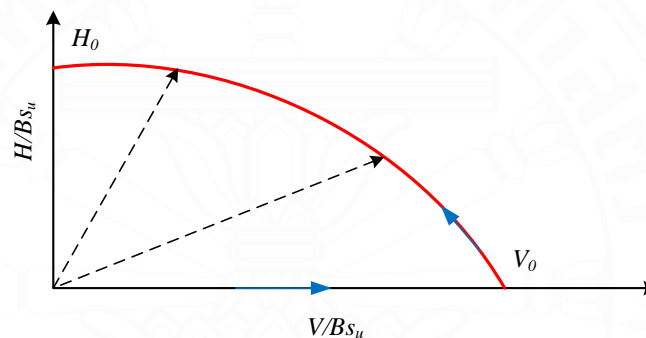


Figure 2.7 Numerical swipe and probe test for strip foundation

Swipe tests are carried out by first loading the foundation vertically until a failure load V_0 is reached (Figure 2.7). The vertical displacement is then kept constant, and when the foundation is translated or rotated it has been found the load path will track closely along the failure envelope Tan (1990), Martin (1994). Probe tests are undertaken by applying a fixed ratio of displacement or load until failure occurs. For load-controlled probes, when failure is reached a single point will be defined on the failure envelope, and the corresponding incremental displacement vector obtained. Figure 2.7 shows that the failure envelope defined by these three types of tests matches the theoretical solution for this case given by Green (1954). A number of expressions have been proposed to describe the shape of failure envelopes determined numerically or experimentally as a function of the loads V , H and M . It has been found that different expressions are required for different foundation configurations and soil types.

A failure envelope is defined in load space and describes the ultimate capacity of a foundation under the simultaneous action of two or more load

components. This approach is advantageous as it allows for the exploration of foundation capacity under different loading combinations, see Gottardi and Butterfield (1993). Loading combinations which are located within the envelope are viable and outside are unviable. Numerous failure envelopes have previously been determined by fitting expressions to experimental Tan (1990), Martin (1994), Gottardi et al. (1999) or numerical results Taiebat and Carter (2005), Gourvenec (2008), and Feng et al. (2014).

2.2.3 Bearing capacity of foundation in undrained condition

The bearing capacity of foundations in undrained conditions is a primary focus of this thesis and is reviewed in further detail in this section. Consideration has been given to both surface and embedded foundations as shown in Figure 2.8. Foundation embedment is commonly achieved offshore by the use of thin-walled skirts beneath the foundation base which penetrate into the seabed. The skirts improve foundation capacity by trapping the soil within the skirted compartment such that it can act as a solid embedded foundation with loads transferred to the foundation base.

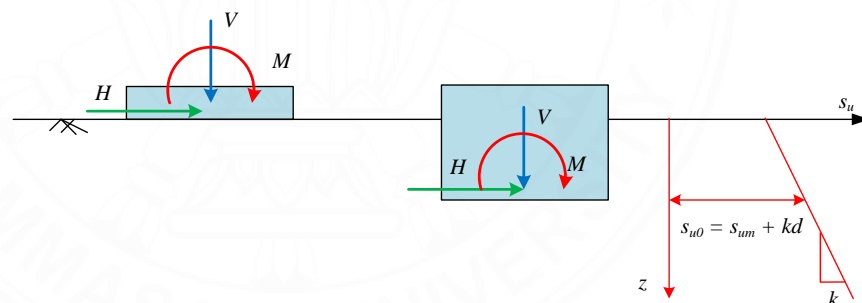


Figure 2.8 Surface and embedded foundations with undrained shear strength assumption (after Tan, 1990)

In undrained conditions the soil friction angle ϕ is taken to be zero and the variation of undrained shear strength s_u with depth is a key parameter. For ease of assessment in bearing capacity calculations the soil strength profile variation is often assumed to be either homogeneous or to increase linearly with depth such that

$$s_u = s_{um} + kz \quad (2.13)$$

where s_{um} is the undrained strength at the soil surface (often referred to as mudline), k is the rate of strength increase with depth, and z is the depth below the

soil surface (Figure 2.8). In the case of homogeneous soil $k = 0$. For normally consolidated (NC) soils a linearly increasing soil strength profile with zero mudline strength, $s_{um} = 0$, can often give a good approximation of the soil strength variation with depth. The strength profile for over consolidated (OC) soils is typically less linear in its variation with depth, but often a reasonable linear approximation can still be made. In other case assuming a constant homogeneous profile ($k = 0$) might provide an adequate approximation.

2.2.4 Yield function

The Tresca model is a special case of the Mohr-Coulomb criterion and is applied in the classical undrained bearing capacity solution. The model adopts the failure criterion given by Equation 2.14 as a yield surface such that the yield function becomes

$$f = \sigma_1 - \sigma_3 - 2s_u = 0 \quad (2.14)$$

In three-dimensional principal stress-space the Tresca yield function plots as a hexagonal cylinder, with the space diagonal (where $\sigma_1 = \sigma_2 = \sigma_3$) as its axis (Figure 2.9). When plotted in the deviatoric plane, the vertices of the hexagon correspond to triaxial compression and extension points.

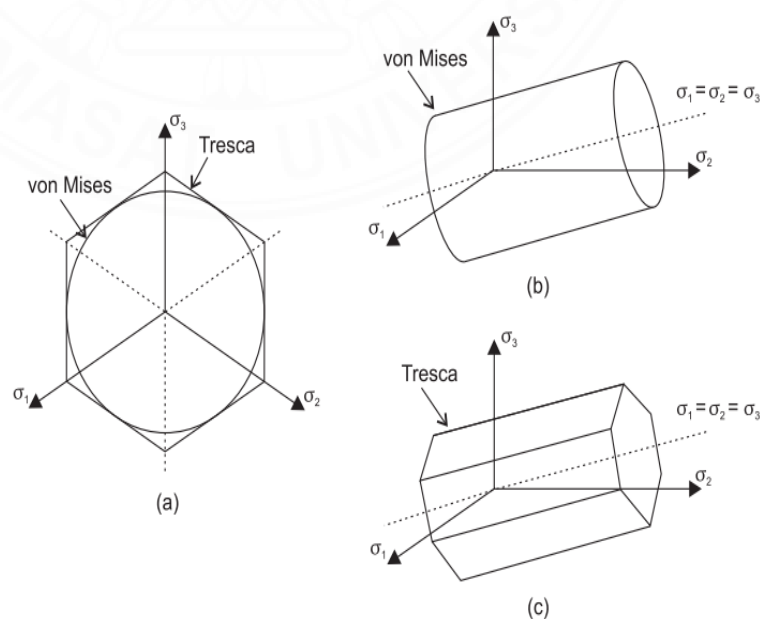


Figure 2.9 Tresca and von Mises failure criterion in a three-dimensional stress space

In finite element analysis (FEA) the Tresca model is a common choice of constitutive model for the analysis of undrained problems. A disadvantage of the Tresca model in FEA is that the yield and plastic potential surface corners can create implementation problems and numerical difficulties for the analysis software. When using FELA, 3D analysis of Tresca materials requires semi definite programming, which is a more challenging class of numerical optimization than SOCP.

2.3 Capacity under combined loading

2.3.1 Classical approach

Combined loading is incorporated into the classical approach using an inclination factor (for horizontal loading) and the effective width principle (for moment loading). Based on the classical approach, the DNV (1992) guidelines suggest the following expression to be used for undrained foundation capacity under combined loads.

$$V_{\max} = F \left(N_c s_{u0} + \frac{kB'}{4} \right) (1 + s_{ca} + d_{ca} - i_{ca}) A \quad (2.15)$$

where F is a correction factor to account for interface roughness and the degree of heterogeneity Davis and Booker (1973), N_c is the bearing capacity for a strip on homogeneous soil is 5.14, and B' is the effective width of the foundation. The shape factor s_{ca} can be calculated as follows

$$s_{ca} = s_{cv} (1 - 2i_{ca}) \frac{B'}{L} \quad (2.16)$$

and is dependent on the coefficient s_{cv} which is a function of the strength heterogeneity. In homogeneous soil $s_{cv} = 0.2$. The depth factor is given by

$$d_{ca} = \frac{s_{u1}}{s_{u2}} 0.3 \tan^{-1} \left(\frac{d}{B'} \right) \quad (2.17)$$

where s_{u1} is the average undrained shear strength above base level and s_{u2} is the equivalent shear strength below base level which is described by

$$s_{u2} = \frac{1}{5.14} \left(5.14 s_{u0} + \frac{kB'}{4} \right) \quad (2.18)$$

The inclination factor i_{ca} is given by

$$i_{ca} = 0.5 - 0.5 \sqrt{1 - \frac{H}{A' s_{u0}}} \quad (2.19)$$

For purely vertical loading on homogeneous soil Equation 2.6 reduces to $V_{max} = 5.14A s_{um}$ which matches the exact solution for a surface strip foundation. For circular and square surface foundations on homogeneous soil, the equation becomes $V_{max} = 6.17A s_{um}$. When horizontal loading is introduced, the inclination factor i_{ca} is equivalent to the solution by Green (1954) and so is accurate for the case of a strip foundation on homogeneous soil (see Figure 2.2), but does not take into account change for other foundation geometries. These are close to solutions for a strip found from plasticity analysis of about $M_{max} = 0.66AB s_{um}$ by Houlsby and Puzrin (1999).

Whilst Equation 2.6 is seen to provide a reasonable match with analytical solutions for the case of inclined loading ($V-H$) or eccentric loading ($V-M$) on homogeneous soil, this is less the case for heterogeneous soil, as described in Randolph et al. (2005) for example. Furthermore, loading cases where inclined and eccentric loading occur in combination ($V-H-M$) are also not handled well.

2.3.2 Failure envelopes

Failure envelopes for undrained conditions have been investigated by experimentally, numerically, and analytically using plasticity solutions. Martin (1994) undertook an experiment by conducting swipe tests on model circular foundations on clay, as shown in Figure 2.10. The envelope indicates that no tension can be sustained. It also shows that as the vertical load approaches zero the horizontal capacity approaches zero. Martin and Houlsby (2000) suggested that undrained loading conditions may not have been maintained at this loading condition due to the shallow nature of the sliding failure mechanism. Noted that the equation describing the model failure envelope in dimensionless terms is as follows Martin and Houlsby (2000), Martin and Houlsby (2001).

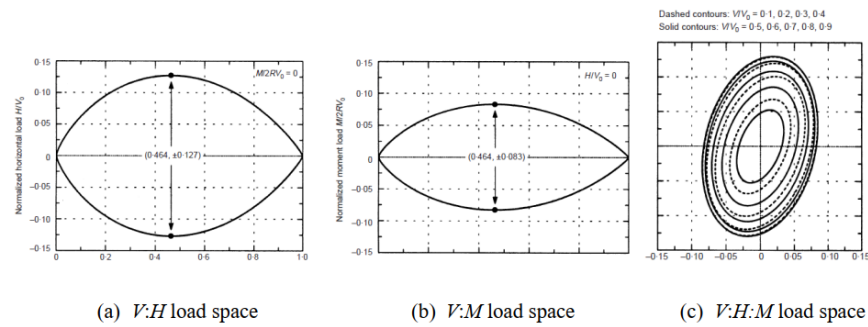


Figure 2.10 Normalised failure envelopes (Martin and Houlsby, 2000)

A number of numerical studies have been undertaken using FEA to map out the shape of failure envelopes under $V:H:M$ loading by Bransby and Randolph (1998), Ukritchon et al. (1998), Taiebat and Carter (2000), Gourvenec and Randolph (2003), Gourvenec and Barnett (2011). Taiebat and Carter (2000) undertook FEA of a surface circular foundation on homogeneous soil. Different load combinations were applied to the foundation and used to define the failure envelope as shown in Figure 2.11.

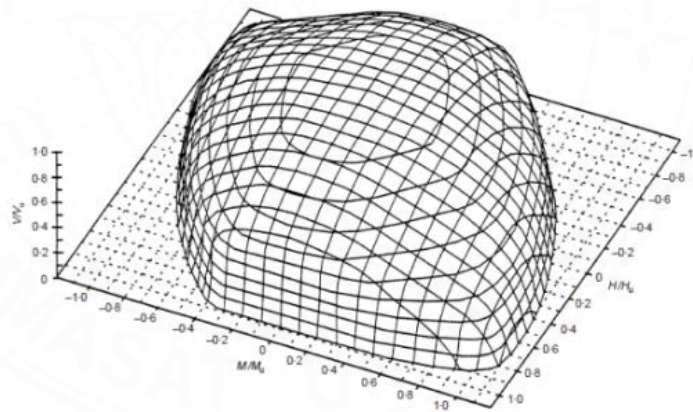


Figure 2.11 Failure envelope of circular footing on homogenous clay (Taiebat and Carter, 2000)

Gourvenec (2007b) undertook finite element analysis of the same problem and compared the results to the failure envelope approximation given by Taiebat and Carter (2000). The comparison is given in Figure 2.12 and shows that there is a reasonable match.

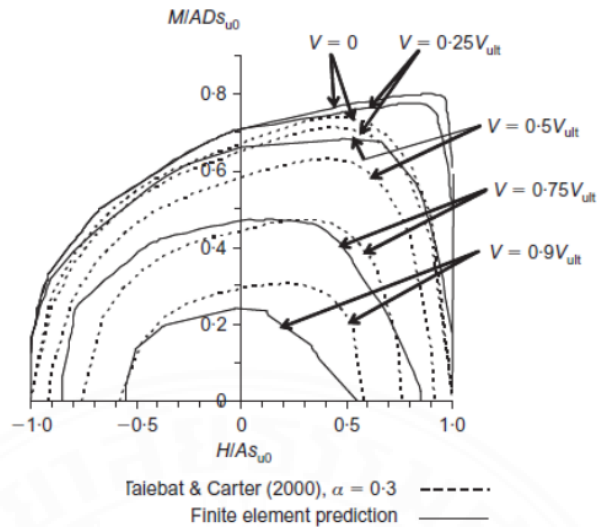


Figure 2.12 Comparison studies of Taiebat and Carter, 2000 with finite element result (Gourvenec, 2007)

In addition, plasticity theory has been used as another approach to investigate undrained failure envelopes Bransby and Randolph (1998), Houlsby and Puzrin (1999), Randolph and Puzrin (2003). Bransby and Randolph (1998) used upper bound plasticity calculations to estimate upper bound failure envelopes for a surface strip foundation under combined loading with full tension capacity. The mechanisms adopted were informed from the results of FEA for different load combinations. Each mechanism was derived from either ‘scoop’ or ‘wedge’ components (see in Figure 2.13).

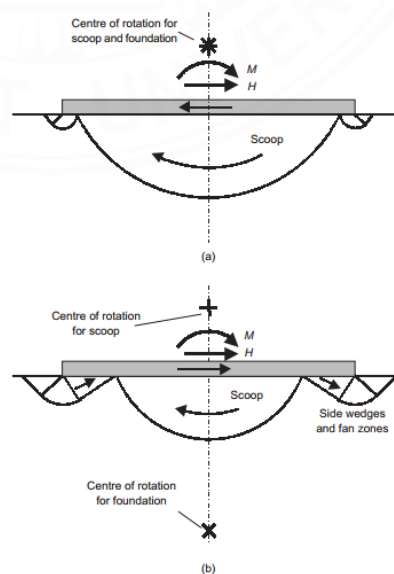


Figure 2.13 Upper bound wedge scoop failure mechanisms (Gourvenec, 2003)

2.3.3 Effective foundation tension capacity

Several studies have investigated the impact that the tension capacity of a foundation has on its performance under combined loading Salencon and Pecker (1995a), Salencon and Pecker (1995b), Michalowski and You (1998), Houlsby and Puzrin (1999). The bounding cases are for a foundation sustaining either full or zero-tension capacity (the latter is imposed when adopting the effective width rule). Ukritichon et al. (1998) considered these two cases by undertaking finite element limit analysis of a strip foundation where both full and zero-tension soil-foundation interfaces were modelled. Figure 2.14 shows the V - H - M failure envelope obtained from the analysis. The results illustrate that there is reduced moment capacity for the case where no tension is sustained.

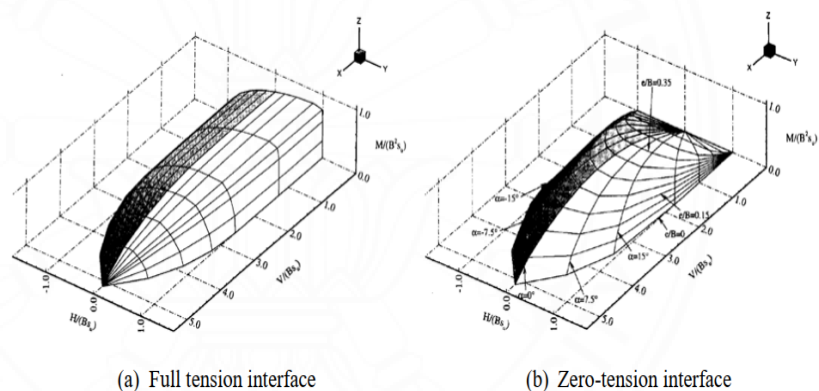


Figure 2.14 Failure envelopes for strip footing (Ukritichon, 1998)

2.3.4 Effective foundation shape

Figure 2.15 gives displacement contours from FEA undertaken by Gourvenec et al. (2006) for comparison. It is seen that diagonal symmetry is also obtained, although the shape of the failure mechanism implied by the displacement profile is different since it does not taper appreciably towards the corners. Four symmetry planes were obtained.

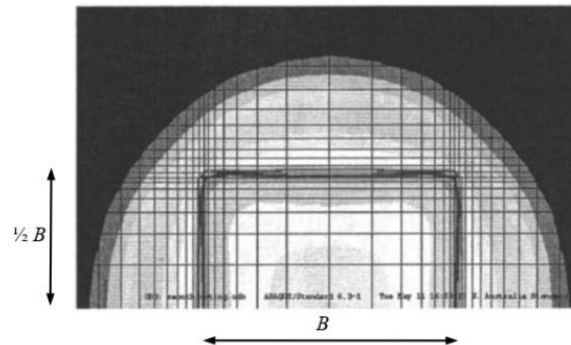


Figure 2.15 Numerical result for smooth square foundation (Gourvenec et al, 2006)

The combined loading of strip foundations can be assessed in plane strain which makes the analysis more straightforward. Previous studies have also addressed circular foundations, and less commonly square and rectangular foundations. Gourvenec (2007b) undertook FEA of strip, circular and square foundations to investigate the effect of foundation shape on bearing capacity under combined loading (Figure 2.16).

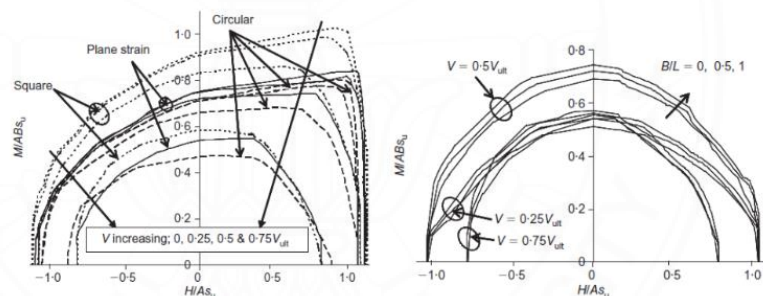


Figure 2.16 Shaped effects on combined load failure envelopes (Gourvenec, 2007)

The results show that bearing capacity determined under plane strain conditions may not be reliably applied for the case of circular and square foundations. When full interface tension was permitted, the normalised moment capacity of a square foundation was found to be significantly larger than a strip (by about 30%), whilst the capacity of a circular foundation was similar, although slightly lower (Figure 2.16). For a zero-tension interface, the moment capacity of a square foundation ($B/L = 1$) was only marginally greater than that of a strip foundation ($B/L = 0$).

2.3.5 Theory of bearing capacity

Gourvenec and Randolph (2003) undertook FEA to investigate the effect of soil strength heterogeneity on bearing capacity of strip and circular

foundations under combined loading. The shape of the failure envelope in the $V:H$ plane was found to be independent of the degree of heterogeneity. In the $H:M$ plane the degree of heterogeneity was found to have a significant effect on the shape of the failure envelope. When normalised by As_{u0} , the failure envelope expands with heterogeneity due to increasing moment capacity (Figure 2.17). When normalised by the peak capacities H_0 and M_0 , the failure envelope is seen to contract in the positive quadrant.

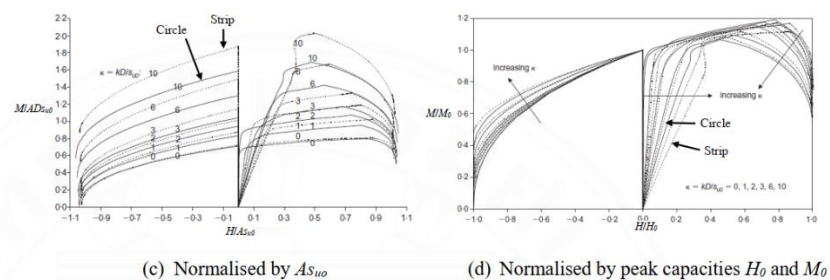


Figure 2.17 Effect of soil heterogeneity on combined load failure envelopes (Gourvenec and Randolph, 2003)

2.4 Anisotropic Undrained Shear (AUS)

The Anisotropic Undrained Shear (AUS) model can be thought as a progression from the Generalized Tresca model. It is a comprehensive stress model for clays and related materials. Anisotropic shear behavior may be seen in natural clays which depends on the shearing mode obtained from laboratory tests. There are three unequal undrained strengths of anisotropic clays that can basically be obtained from triaxial compression (s_{uc}), triaxial extension (s_{ue}), and direct simple shear (s_{us}), which can be represented as a function of the plasticity index of clays.

The usual behavior of clays and related materials under undrained triaxial compression and extension is broadly shown in Figure 2.18. In the triaxial compression test, an initial state given by $\sigma_a = \sigma_r = P_0$ is first established. The axial stress is then increased by an amount $\Delta\sigma_a$ until failure is reached at $\sigma_a - \sigma_r = 2s_{uc}$. In the triaxial extension test, the same initial state is used, but the axial stress is now released by an amount $\Delta\sigma_a$ until failure is reached at $-(\sigma_a - \sigma_r) = 2s_{uc}$. The failure strengths in the two cases, measured by half the difference in axial and radial stress are the undrained shear strengths, s_{uc} and s_{ue} , respectively

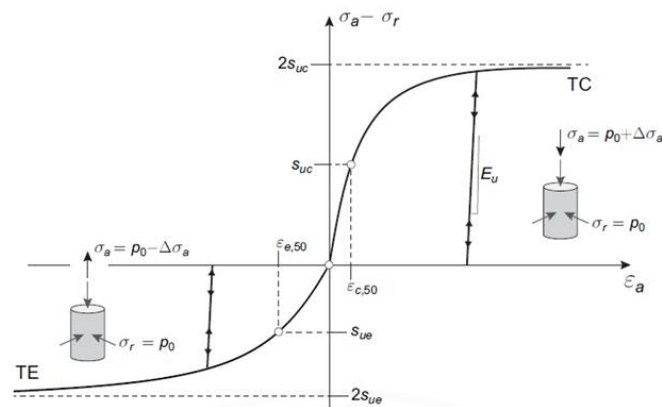


Figure 2.18 Typical stress-strain behaviour in triaxial compression (TC) and triaxial extension (TE).

Two anisotropic strength ratios, namely $r_e = s_{ue}/s_{uc}$ and $r_s = s_{us}/s_{uc}$, are employed as the input dimensionless parameters for FELA. These ratios represent the degree of undrained strength anisotropy of clay. According to the assumption of a harmonic mean relation by Krabbenhoft et al. (2019), the suggested relationships of s_{uc} , s_{ue} , s_{us} , r_e , and r_s are carried out, which can be written as shown below.

$$r_s = \frac{2r_e}{1 + r_e} \quad (2.20)$$

Where $r_e = s_{ue}/s_{uc}$ and $r_s = s_{us}/s_{uc}$

It is usually observed that the undrained shear strengths in triaxial compression (s_{uc}), triaxial extension (s_{ue}) and simple shear (s_{us}) are related to each other by $s_{uc} < s_{us} < s_{ue}$

For the isotropic strength option, the Generalized Tresca surface is used as shown in Figure 2.19 and the triaxial compression and extension strengths are the basic strength parameters.

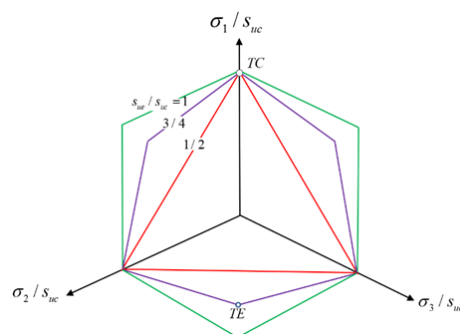


Figure 2.19 Undrained strength envelopes of AUS model for different $r_e = s_{ue}/s_{uc}$ (after Krabbenhoft et al., 2019)

This model comes with the limitation that shown in equation 2.21

$$0.5 < \frac{s_{ue}}{s_{uc}} < 1 \quad (2.21)$$

With s_{ue} and s_{uc} specified, the strength in simple shear follows as:

$$s_{us} = \left(\frac{1}{2} s_{ue}^{-1} + \frac{1}{2} s_{uc}^{-1} \right)^{-1} = \frac{2s_{ue}s_{uc}}{s_{ue} + s_{uc}} \quad (2.22)$$

It is important to note that r_e has a range of 0.5 to 1. For r_e below 0.5 the yield surface becomes non-convex and while ratios of r_e up to 2 in principle could be accommodated and may resulted in a computation error.



CHAPTER 3

METHODOLOGY

3.1 The numerical method

3.1.1 Limit analysis theory

Limit analysis refers to the use of the lower bound (LB) and upper bound (UB) plasticity theorems, which together place limiting values on the theoretical plastic collapse load of a foundation or other structure subject to live loading. The plasticity theorems were developed by Drucker et al. (1952) and Gzodev (1960), amongst other. Assumptions such as perfect plasticity and an associated flow rule are required in order to apply these theorems. Once these assumptions have been made, the method is rational and consistent and the bound theorems can be used to obtain foundation collapse loads directly, without intermediate steps.

To satisfy the LB theorem, a stress field must be found which satisfies the equations of equilibrium, the boundary conditions, and is everywhere below yield. The UB theorem requires an admissible velocity field, mechanism with compatible plastic deformation, no gaps or overlaps, a rate of external work equal to or exceeding the rate of internal plastic energy dissipation, and for deformations to satisfy the associated flow rule.

3.1.2 Finite element limit method

Finite element limit analysis (FELA) refers to numerical implementations of the LB and UB theorems through a finite element discretization of the problem stress and velocity fields. The LB and UB are independent problems but can be formulated using the same element discretization, although different element types are used. Plasticity bound analyses are undertaken using the following general steps:

Step 1 is the problem domain is discretised into elements

Step 2 is the constraints required by the LB and UB theorem are enforced within and between connected elements.

Step 3 is the variables and constraints are arranged as an optimization problem. In general, this problem will involve both linear and nonlinear constraints.

Step 4 is a numerical optimization technique is used to find the optimal LB or UB collapse load multiplier, or load factor.

Lower bound FELA

To implement LB FELA, a piecewise continuous stress field is usually introduced in the elements of discretised domain. An early implementation of LB FELA was undertaken by Belytschko and Hodge (1970). Belytschko and Hodge used quadratic triangle elements, which can cause difficulty in enforcing the yield criterion throughout the element. Analysis undertaken by Lysmer (1970) used linear triangle elements, which have the advantage that the yield criterion will be satisfied everywhere in the element if it is enforced at the vertices

Commercially available limit analysis software, OptumG2 Krabbenhoft et al. (2015), formulates analysis based on the implementation outlined in Krabbenhoft (2007). OptumG2 has recently been used for LB and UB analysis of plane strain and axisymmetric geotechnical problems (Keawsawasvong and Ukritchon (2016), Ukrit-chon and Keawsavong (2016), Keawasavong et al. (2021).

Upper bound FELA

When implementing UB FELA it is often difficult to ensure that the associated flow rule is satisfied throughout the discretised domain. Constant strain elements, three-noded triangles with linear variation of velocity have been used to satisfy this requirement e.g. Bottero et al. (1980), Abdi et al. (1994), Sloan and Kleeman (1995), Pastor et al. (2000) and have been combined with discontinuities in the velocity field to help to compensate for poor accuracy when using linear elements. Figure 3.1 show a linear velocities variation u with the field of constant-stress field σ . In spite of being possible to generate discrete formulations of upper-bound which do not involve the unknown stresses, yield models are restricted by means of a linear envelope.

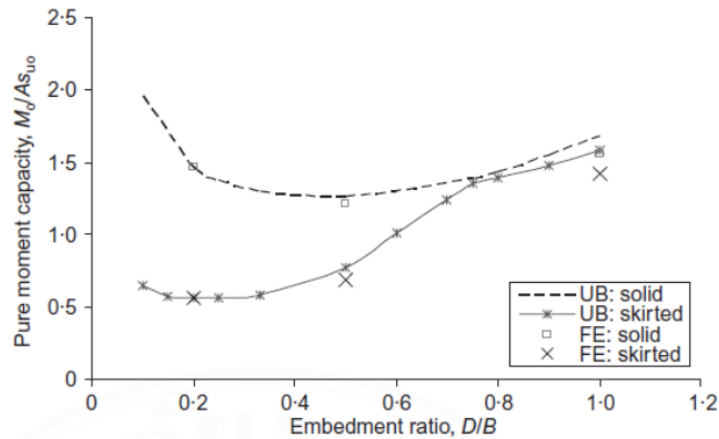


Figure 3.1 Comparison between solid and skirted footing in normally consolidated soil (Bransby and Yun, 2009)

An alternative to the constant strain element approach is outlined in Makrodimopoulos and Martin (2007), first suggested for purely cohesive material by Yu et al. (1994). It was found that six-noded triangles could be used to obtain strict UB solutions in plane strain, provided that the sides of the elements were straight. This element is termed a simplex strain element and is shown in Figure 3.2. Because the strains vary linearly, the flow rule need only be enforced at the three triangle vertices to ensure that it is satisfied throughout the triangle. This element and the method described in Makrodimopoulos and Martin (2007), is implemented in plane strain analyses.

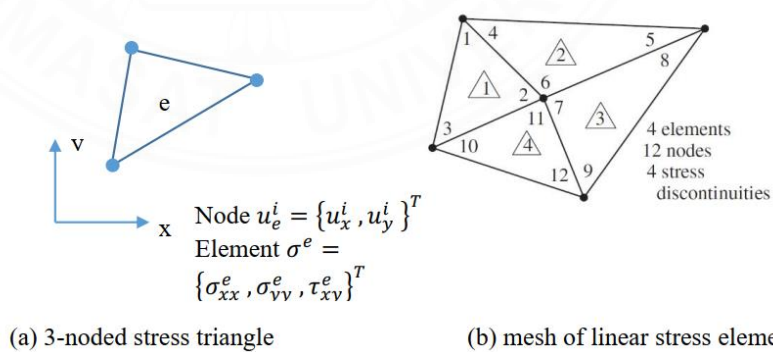


Figure 3.2 Linear element used in limit analysis of upper bound (Lyamin and Sloan, 2002b)

The optimization of UB FELA, just as for the LB, can be formulated as a SOCP problem, provided that the yield criterion can be expressed as a quadratic cone constraint.

3.1.3 The previous applications of three dimensional FELA

Axisymmetric FELA, using SOCP optimization, has recently been used to find capacities of footings caissons in clay soil obeying the Tresca criterion, such as Kumar and Chakraborty (2014), Chakraborty and Kumar (2015), Ukritchon and Keawsawasvong (2016). 3D FELA has been applied to slope stability problems for a number of years by Chen et al. (2001), Li et al. (2009), Lim et al. (2015), and Yang et al. (2003).

Salgado et al. (2004) used 3D FELA to find the vertical bearing capacity of circular, square and rectangular footings in clay. The FELA LB and UB implementations followed Lyamin and Sloan (2002). Symmetry allowed for 15 degree of the circular footing problem domain and one quarter of the rectangular footing problem domain to be analysed, as shown in Figure 3.3.

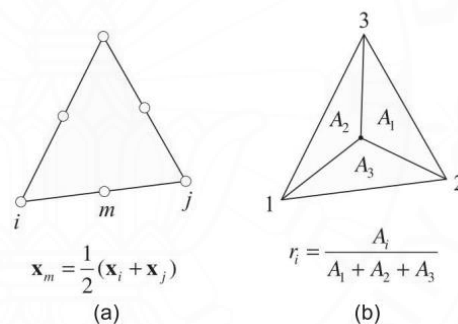


Figure 3.3 Upper bound simplex strain displacement elements (Makrodimopoulos and Martin, 2007)

Martin and Makrodimopoulos (2008) undertook 3D FELA of Mohr-Coulomb materials by using semidefinite optimization. Two example problems were considered, the compression of a square block and the expansion of a thick spherical shell. 3D FELA of Mohr-Coulomb material using semidefinite optimisation was also undertaken by Krabbenhoft et al. (2008).

Failure envelopes for combined loading are found by probing in displacement space. A number of displacement-controlled probes can be used to define a failure envelope (Figure 3.4). FEA is very popular for the analysis of offshore foundations and displacement-controlled probes are the most common method for

determining failure envelope, as highlighted by Bransby and Randolph (1999), Gourvenec (2007), Gourvenec and Barnett (2011), Feng et al. (2014).

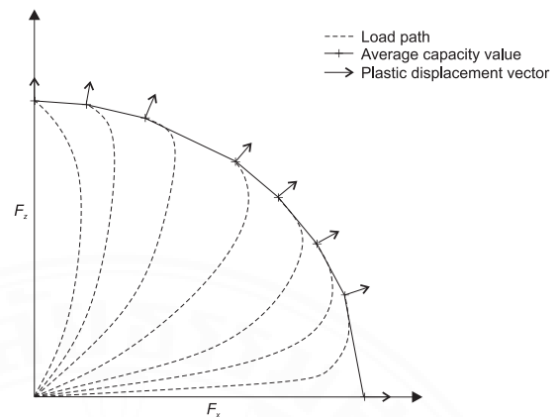


Figure 3.4 Quadrant of a failure envelope found using FEA (Bransby and Randolph, 1999)

OptumG2, Krabbenhoft (2015) is the program of finite element for analysis of strength and deformation for boundary value problems of geotechnical engineering as illustrated in Figure 3.5. Rigorous upper and lower bounds to the failure loads are possible to be calculated, by ranging the exact solution from above and below. Special features providing an exact modeling involve special elements used in modeling joints, geotextiles, walls, interfaces and anchors.

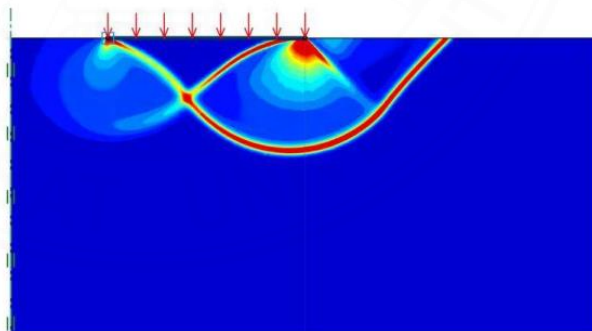


Figure 3.5 Example model using OptumG2 (Krabbenhoft, 2015)

Optum G3 Krabbenhoft (2018) is a software tool designed for analyzing and designing shallow foundations, it provides an efficient method to determine bearing capacities and the capability to perform elastoplastic analysis for settlement predictions. The application of lower and upper bound finite element analysis to geotechnical problems considering plane-strain conditions has been conducted as early as Lysmer (1970) and Bottero et al. (1980). Based on these works

many contributions enabled continuous improvement of both methods Sloan (2013). A model using OptumG3 is illustrated in Figure 3.6. The methods permit discontinuities in the stress and velocity fields, Merifield et al. (1999). Compared with traditional incremental finite element method, the procedures are very fast and straightforward to use Sloan (2005), giving the limit load directly, without the need to perform a complete incremental analysis. This is a major advantage in large-scale three-dimensional applications, where stability analysis using the conventional finite-element method is both difficult and time consuming Sloan (2013). In this study, OptumG3, Krabbenhoft (2018) is applied to perform finite-element lower and upper bound analyses.

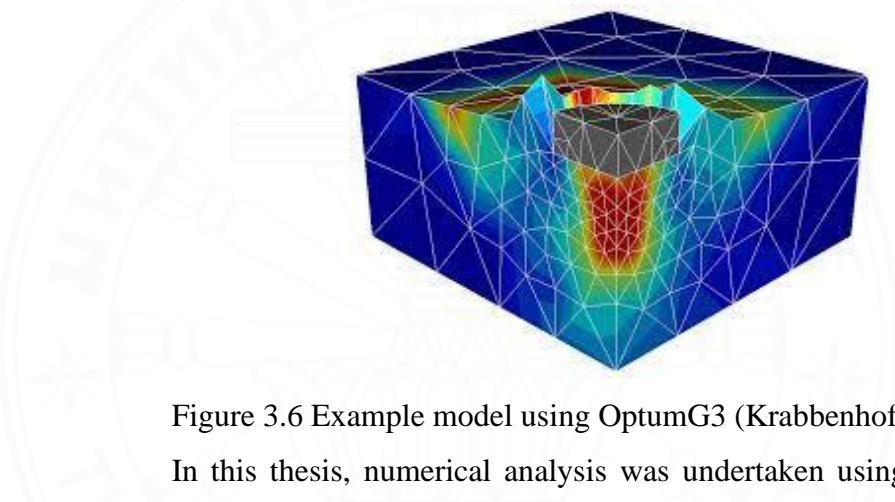


Figure 3.6 Example model using OptumG3 (Krabbenhoft, 2018)

In this thesis, numerical analysis was undertaken using the FELA program OptumG2 and OptumG3, Krabbenhoft (2015) to model some of the shallow foundation. OptumG2 and OptumG3 uses plasticity theory to generate both lower bound (LB) and upper bound (UB) collapse loads for plane strain problems. The lower bound solution requires a statically admissible stress field to be upheld and stresses associated with each element must satisfy equilibrium and not violate the yield criterion for the soil. OptumG2 and OptumG3 applies equivalent loads to the vertices of each element and generates constraints to enforce the plastic flow rule. The resulting solution requires equalising the internal and external work.

3.2 Machine learning approach

3.2.1 Gradient boosting machine (GBM) algorithm

Gradient boosting machine (GBM) is a machine learning algorithm that can be used for both regression and classification problems in a variety of fields

including geotechnical engineering Friedman (2001), Touzani et al. (2018), Zhou et al. (2016), Qi et al. (2018), Qi and Tang (2018), Roe et al. (2005). GBM aims to improve the performance of a model by combining many fitted base-learners together Natekin and Knoll (2013). Decision tree (DT) algorithm is a non-parametric supervised learning method, and it aims to create a base-learner that predicts the value of a target variable by learning simple decision rules inferred from the data features Zhou et al. (2015). A decision tree contains one root node, several internal nodes and leaf nodes (see in Figure 3.7), which can be regarded as a piecewise constant approximation. To find a single, highly accurate strong learner (i.e., a strong DT here) may be difficult sometimes, while it is easy to find many simple base-learners (Schapire, 2003). GB algorithm proposed by Friedman (2001) combines multiple base-learners to improve the model performance and avoid difficulties in finding a strong learner. A differentiable loss function is determined before the whole process of gradient boosting which is centered on the minimization of this function Qi et al. (2018). The calculation steps of the GBM algorithm are briefly introduced as follows (see Figure. 3.8).

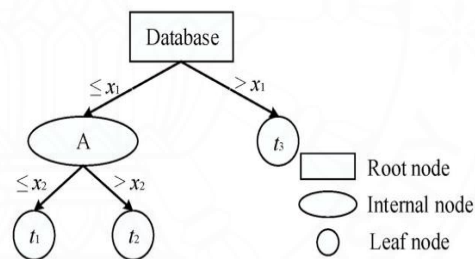


Figure 3.7 Structure of a decision tree (Zhou et al., 2015)

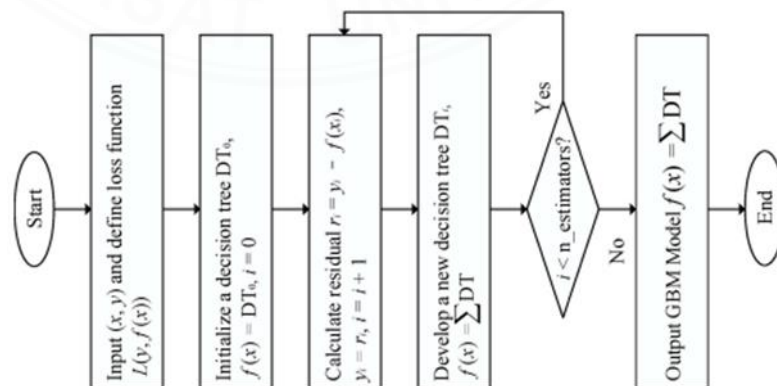


Figure 3.8 GBM algorithm calculations (Chen et al., 2022)

Previous studies Gourvenec and Barnett (2011), Ibsen et al. (2014), Liu et al. (2014), Zhang et al. (2020) showed that the failure envelope has a nearly ellipse shape in the H-M plane. The general form of an ellipse can be described as follows

$$A_1 X^2 + A_2 XY + A_3 Y^2 + A_4 = 0$$

$$\begin{cases} A_1 = a^2 \sin^2 \varphi + b^2 \cos^2 \varphi \\ A_2 = 2(b^2 - a^2) \sin \varphi \cos \varphi \\ A_3 = a^2 \cos^2 \varphi + b^2 \sin^2 \varphi \\ A_4 = -a^2 b^2 \end{cases} \quad (3.1)$$

where a and b are the lengths of the semi-major and semi-minor axes, respectively, φ is the rotation angle of the major axis.

The performance of GBM based regression model for the prediction of fitting parameters can be evaluated by regression evaluation indicators quantitatively, such as mean square error (MSE) and the coefficient of determination (R^2) which are defined by

$$MSE = \frac{1}{n} \sum_{i=1}^n (y_i^p - y_i^a)^2 \quad (3.2)$$

And

$$R^2 = \frac{\sum_{i=1}^n (y_i^p - \bar{y}^a)^2}{\sum_{i=1}^n (y_i^a - \bar{y}^a)^2} \quad (3.3)$$

where y_i^p is the i th predicted target value, y_i^a is the i th actual target value, n is the number of data and \bar{y}^a is the average value of y_i^a .

MSE reflects the average prediction error of a model, a value of MSE = 0 indicates a perfect model while a large value of MSE indicates an inferior model. The coefficient of determination R^2 is used to characterize the quality of a fit through changes in data, which normally ranges from 0 to 1. The closer it is to 1, the stronger the model in explaining the relationship between input variables and target variables Zhang et al. (2020). A prediction with a low value of MSE and a high value of R^2 indicates an excellent performance of the regression model. The goodness of fit of

fitting and predicted curves to the failure envelope can be also evaluated by such indicators Chen et al. (2022).

3.2.2 Extreme Gradient Boosting (XGBoost)

Extreme Gradient Boosting (XGBoost) has become increasingly popular since the influential research works published by Chen and Guestrin (2016) and Kim et al. (2022). This popularity is due to its combination of bagging and boosting techniques, leading to its high adaptability and efficiency. As a result, XGBoost was frequently used in successful machine learning competition solutions, particularly on platforms like Kaggle (Sheridan et al., 2016). However, its application in geotechnical engineering has been very limited, as indicated by research from Nguyen et al. (2023), Dessi et al. (2023), Tran et al. (2024), and Dong et al. (2023). XGBoost functions as an ensemble algorithm with the regression tree as its base model. Non-leaf nodes split the data space into two regions, and the leaf nodes represent these regions with assigned values (Breiman, 2017; Bharti et al., 2021). The model function is defined by Fathipour-Azar (2021) in Eq. (3.4).

$$\hat{y}_T = \sum_{t=1}^T f_t(x_i) \quad (3.4)$$

where T indicates the total number of regression trees, $f_t(x_i)$ denotes the output from the t^{th} tree, and \hat{y}_t represents the predicted value generated by the XGBoost model. The hyperparameters are identified using the *GridSearchCV* method from the scikit-learn package (Pedregosa et al., 2011). They include the number of trees, maximum tree depth, learning rate, minimum loss reduction threshold, regularization factor, and subsample ratio. Recently, the applications of the machine learning model in geotechnical engineering are seen in the works of Zhou et al. (2021), Zhang et al. (2017), Zhang et al. (2018), Zheng et al. (2019, 2020), and Lai et al. (2021a, b). For a deeper understanding of XGBoost, readers can refer to the study by Chen and Guestrin (2016).

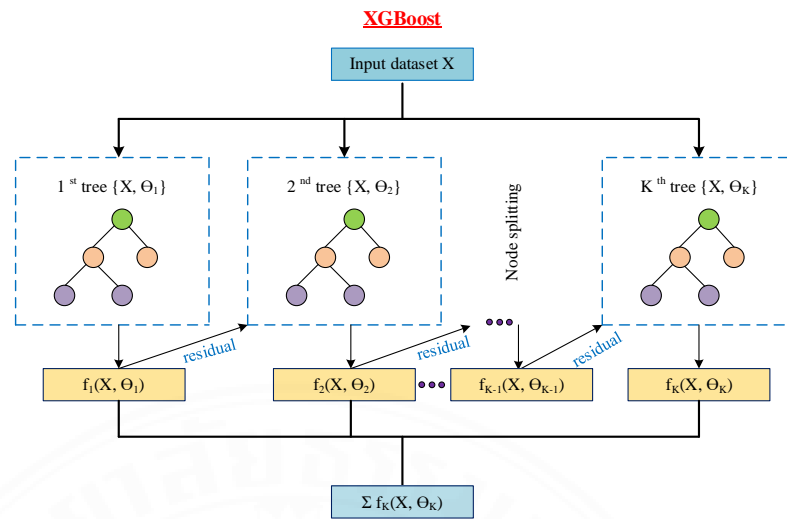


Figure 3.9 An example of the XGBoost algorithm structure

3.2.3 Artificial neural network (ANN)

Artificial neural networks (ANN) are computing methods that are based on the function of the human brain neural network (Basheer and Hajmeer, 2000). An ANN consists of an input layer, some hidden layers, and an out-put layer. All nodes in one layer are connected to all other nodes in the next layer. The design of ANN models follows several systematic steps. In general, there are five basic steps Dongare et al. (2012), including Collect data, Data preprocessing, Building a network, Training, and Model test performance.

Collecting and preparing sample data is the first step in designing an ANN model. Figure 3.10 shows the scheme of the ANN model.

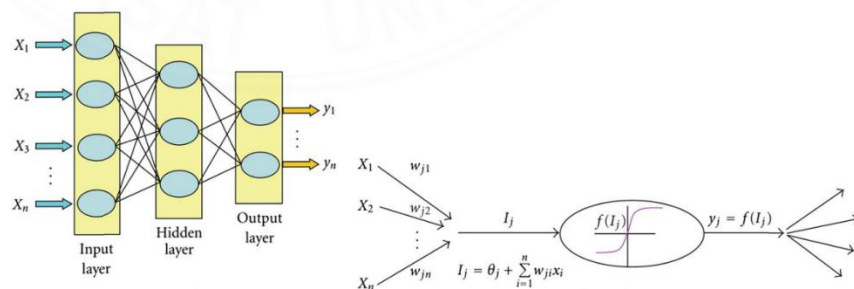


Figure 3.10 A typical structure and operation of ANN

Each layer contains computational units (neurons) connected to other neurons by weights. Each neuron can in fact calculate a weighted sum of its inputs

which is transmitted to a transfer function (f) in order to produce the outputs, Equation 3.5

$$I_j = \sum_{i=1}^n W_{ji} \times X_i + \theta_j$$

$$Y_j = f(I_j) \quad (3.5)$$

Where I_j : output value; X_i : the input value; W_{ji} : the weights of the connections; n : the number of inputs.

The most popular and commonly used ones are the sigmoid, binary step, hyperbolic tangent, and radial functions Arama (2021). This process is repeated iteratively until the desired error is reached Goutham and Krishnaiah (2021).

3.3 Parametric study

3.3.1 Parametric studies in failure envelope of strip footing

The strip footing is subjected to various loads involving vertical force (V), horizontal force (H), and bending moment (M). It is important to emphasize that the positive orientation is assigned to the vertical load in the compression condition (vertical load applied downward to the footing) in this study.

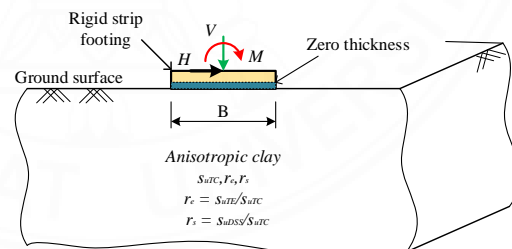


Figure 3.11 Problem for failure envelope of strip footing

In this study, a 3D failure envelope in the space of V - H - M is adopted to express the undrained capability for the strip footing in anisotropic clay under various loading conditions. For practical application, the output results (V - H - M) of the 3D failure envelope are normalized following the dimensionless approach as introduced by Butterfield (1999), as shown in Eq. (3.6):

$$\frac{V}{s_{uTC} B}, \frac{H}{s_{uTC} B}, \frac{M}{s_{uTC} B^2} = f(r_e) \quad (3.6)$$

where V/s_{uTCB} is the non-dimensional vertical load coefficient; H/s_{uTCB} is the non-dimensional horizontal load coefficient; M/s_{uTCB}^2 is the non-dimensional bending moment coefficient, and r_e represents the anisotropic ratio.

The numerical of model is shown in Figure 3.12

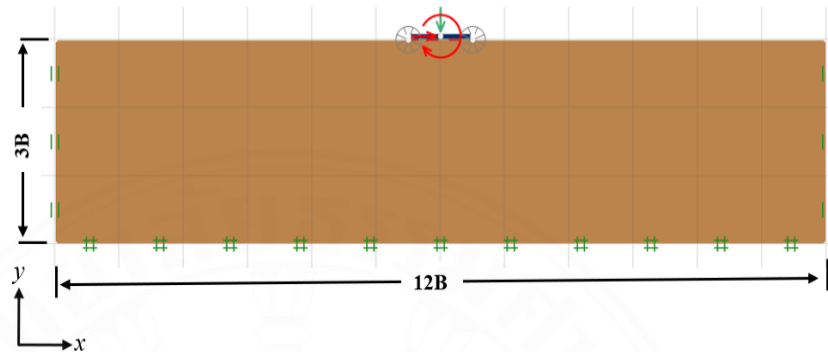


Figure 3.12 A numerical model of finding the failure envelope of strip footing

The physical properties for all cases which include the failure envelope problem in natural clay are described in Chapter 2. The parametric studies for strip footing on anisotropic clay are shown in table below, respectively.

Table 3.1 Parametric studies for all cases in failure envelope of strip footing

Parameter	Symbol	Considered range
Vertical load	V	1 unit
Bending moment load	M	1 unit
Horizontal load	H	f(M)
Anisotropic strength ratio	r_e	0.5 – 1.0
The interface		No tension or tension cut-off conditions

3.3.2 Parametric studies in failure envelope of ring foundation

The ring foundation has an internal radius (r_i) and an external radius (r_o), and it is subjected to combined $V-H-M$ loads. It is important to emphasize that the positive orientation is assigned to the vertical load in the compression condition (vertical load applied downward to the footing) in this study.

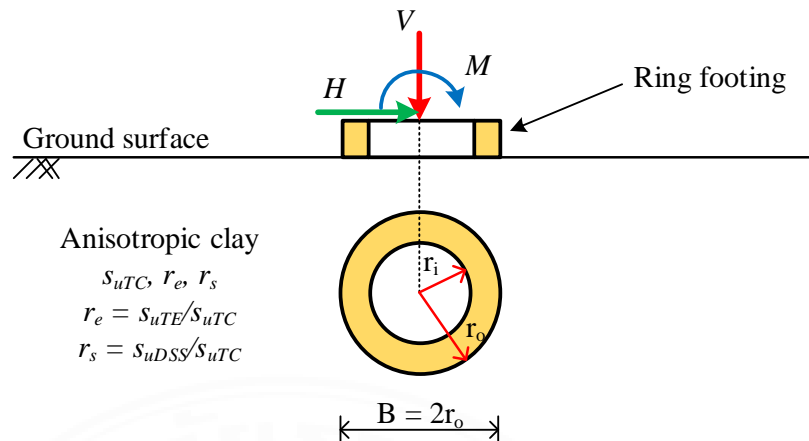


Figure 3.13 Problem for failure envelope of ring foundation

Applying Butterfield (1999) dimensionless approach reveals that two dimensionless input factors predominantly lead to the normalized output outcomes (V - H - M) represented in Eq. (3.8).

$$\frac{V}{s_{uTC}A}, \frac{H}{s_{uTC}A}, \frac{M}{s_{uTC}AB} = f\left(\frac{r_i}{r_o}, r_e\right) \quad (3.8)$$

where the radius ratio is denoted as (r_i/r_o) and the anisotropic strength coefficient is presented as (r_e). The specified dimensionless values for these parameters in the research are $r_i/r_o = 0, 0.2, 0.4, 0.6$, and $r_e = 0.5, 0.6, 0.7, 0.8, 0.9$, and 1. The numerical of the model is shown in Figure 3.14

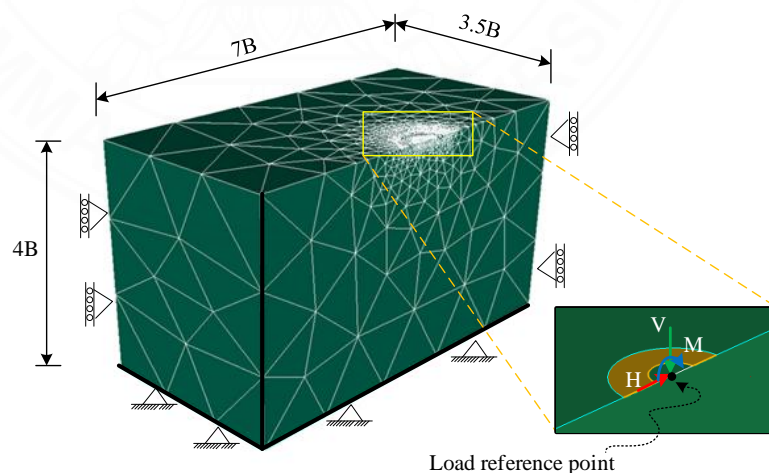


Figure 3.14 A numerical model of finding the failure envelope of ring foundation

The physical properties for all cases which include the failure envelope problem in natural clay are described in Chapter 2. The parametric studies for ring footing on anisotropic clay are shown in table below, respectively.

Table 3.2 Parametric studies for all cases in failure envelope of ring foundation

Parameter	Symbol	Considered range
Vertical load	V	1 unit
Bending moment load	M	1 unit
Horizontal load	H	$f(M)$
The radius ratio	r_i/r_o	0 - 0.6
Anisotropic strength ratio	r_e	0.5 - 1.0
The surface area	A	$\pi(r_o^2 - r_i^2)$
The interface		Rough

3.3.3 Parametric studies in failure envelope of conical foundation

The foundation is subjected to vertical force (V), horizontal force (H), and bending moment (M) for assessing the combined V - H - M failure envelope on anisotropic clay. The positive orientation is assigned to the vertical load in the compression condition (vertical load applied downward to the footing) in this study.

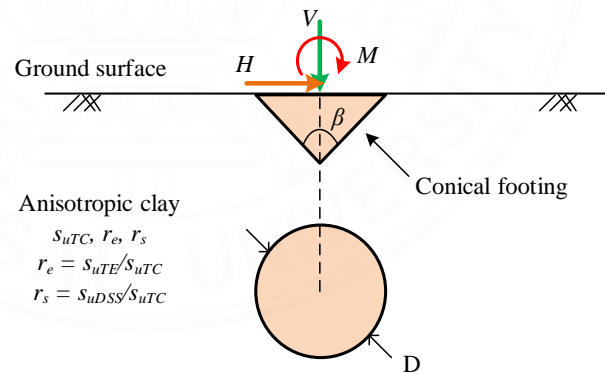


Figure 3.15 Problem for failure envelope of conical foundation

The dimensionless method introduced by Butterfield (1999) is utilized, and it enables the derivation of normalized output results (V - H - M) for conical foundations subject to various loading conditions in anisotropic clay. The formulation is based on two input parameters, as shown in Eq. (3.9).

$$\frac{V}{s_{uTC}A}, \frac{H}{s_{uTC}A}, \frac{M}{s_{uTC}AD} = f(\beta, r_e) \quad (3.9)$$

where β represents the cone apex angle and r_e denotes the anisotropic strength ratio. The study examines the effects of these parameters with the different values of β at 90, 120, 150, and 180 degrees, while r_e ranges from 0.5 to 1 in increments of 0.1. The numerical of the model is shown in Figure 3.16.

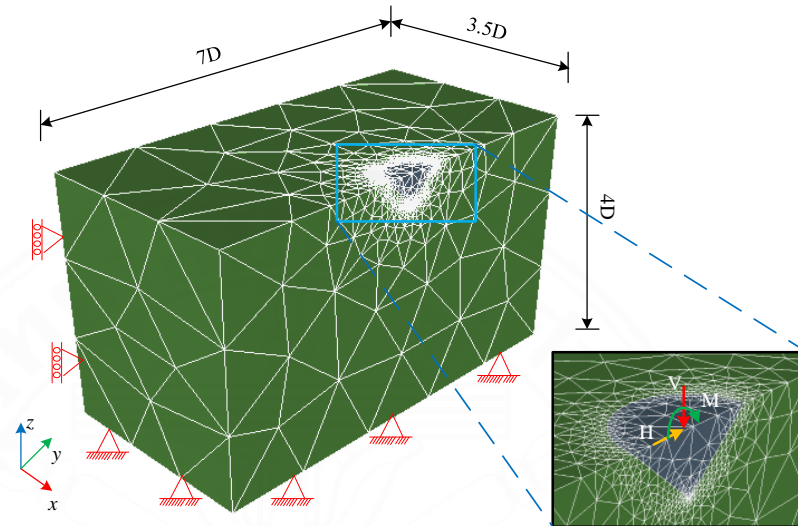


Figure 3.16 A numerical model of finding the failure envelope of conical foundation

The physical properties for all cases which include the failure envelope problem in natural clay are described in Chapter 2. The parametric studies for conical footing on anisotropic clay are shown in table below, respectively.

Table 3.3 Parametric studies for all cases in failure envelope of conical

Parameter	Symbol	Considered range
Vertical load	V	1 unit
Bending moment load	M	1 unit
Horizontal load	H	$f(M)$
The cone apex angle	β	90 -180
Anisotropic strength ratio	r_e	0.5 – 1.0
The surface area	A	$\pi D^2/4$
The interface		Rough

CHAPTER 4

FAILURE ENVELOPES OF STRIP FOUNDATIONS

4.1 Introduction

In geotechnical engineering science, the footings of offshore structures often experience general load consisting of vertical load (V), horizontal load (H), and bending moment (M). Various numerical and experimental studies have explored the behavior of different foundation types subjected to general loading in clay. These studies include the works of Bransby and Randolph (1998), Bransby and Yun (2009), Martin (1994), Martin and Houlsby (2000), Gourvenec and Randolph (2003), Gourvenec (2008), Gourvenec and Barnett (2011), Taiebat and Carter (2000), Yun and Bransby (2007), and Bolton and Lau (1993). Generally, the combined loading problems were based on the traditional bearing capacity design method, as proposed by Brinch Hansen (1970), Meyerhof (1953), Vesic (1975), and Das and Larbi (1983).

The methodology of this failure envelope was initially proposed by Roscoe and Schofield (1957). Numerous studies have explored the utility of this methodology, including previous works by Butterfield and Ticof (1979), Butterfield and Gottardi (1994), Feng et al. (2014), Martin and Houlsby (2001), Gourvenec (2007), Mana et al. (2013), Nova and Montrasio (1991), Ukritchon et al. (1998), Vulpe et al. (2013), Zhang et al. (2011), and Ibrahim et al. (2022).

It is worth noting that soils typically exhibit various levels of strength anisotropy, as highlighted in previous studies by Davis and Christian (1971), Ladd and Degroot (2003), Law (1978), Pan and Dias (2016), Reddy and Rao (1981), Su et al. (1998), Ukritchon et al. (2003), Kumar and Ghosh (2007), and Yang and Du (2016). These investigations have explored the significant impact of the anisotropic characteristics of natural clays on foundation stability.

This chapter aims to analyze the capacity of strip footings in anisotropic clays under general $V-H-M$ loading. The 3D failure envelope in ($V-H-M$) space and the 2D failure envelope in ($H-M$) spacing considering the effect of the anisotropic behavior of clay and interface interaction between soil and footing are investigated. Then, the

Artificial Neural Network (ANN) models adopted in this chapter can be helpful for practitioners to check the capacity of strip foundations subjected to combined loads (V , H , M) in natural clays.

4.2 Problem statement

The challenge of analyzing a rigid strip footing placed on an anisotropic clay subjected to various loads is illustrated in Figure 4.1. The width of a strip footing is denoted as (B) and subjected to vertical force (V), horizontal force (H), and bending moment (M). Tensile forces in the vertical direction are not considered. The clay profile underlying the strip footing is assumed to be anisotropy and weightless. The numerical models are simulated following full-tension condition and no-tension condition. Note that zero-thickness interface elements are applied to connect footing and soil.

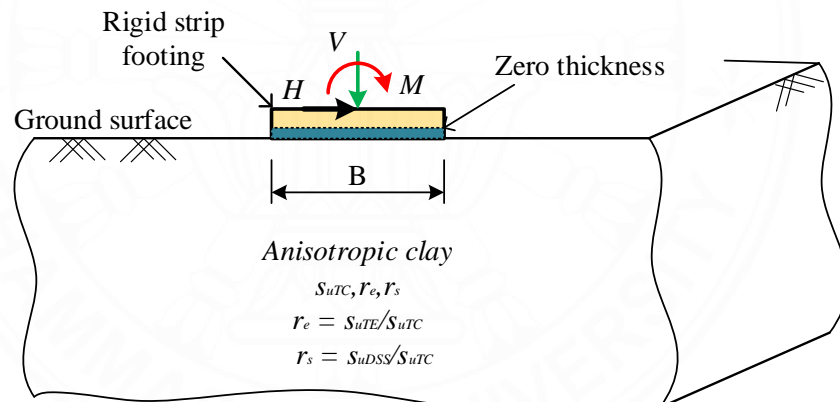


Figure 4.1 Problem definition of finding failure envelope of strip footing

In Chapter 4, the Anisotropic Undrained Shear (AUS) failure criterion and the associated flow rule (Krabbenhoft et al. 2019) are utilized to develop the criterion for anisotropic clay failure. The soil strength requirement for the AUS model is based on three distinct anisotropic undrained shear strengths, which can be acquired through triaxial compression (s_{uTC}), triaxial extension (s_{uTE}), and direct simple shear (s_{uDSS}) tests. In order to emphasize the variability in undrained strength across various directions, two anisotropic strength ratios, denoted as r_e and r_s , are introduced, where their expressions are described in Eqs. (4.1) and (4.2) as shown below:

$$r_e = \frac{s_{uTE}}{s_{uTC}} \quad (4.1)$$

and

$$r_s = \frac{s_{uDSS}}{s_{uTC}} \quad (4.2)$$

Krabbenhft et al. (2019) further explained that the harmonic mean can be derived from the relationship between r_s and r_e , expressed as Eq. (4.3) follows:

$$r_s = \frac{2r_e}{1+r_e} \quad (4.3)$$

where the variable r_e falls within the range of 0.5 to 1. As mentioned by Krabbenhft et al. (2019), altering the value of (r_e) results in a corresponding modification of the failure surface following the AUS failure criterion, as illustrated in Fig. 4.2.

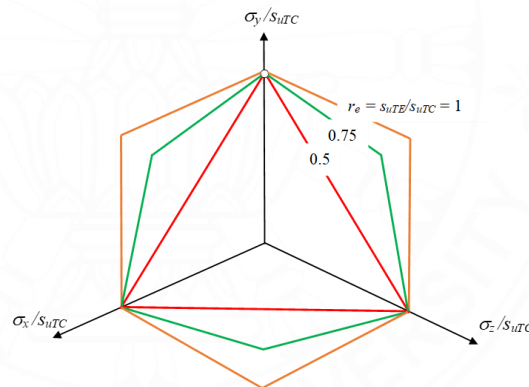


Figure 4.2 The formations of the AUS model with various r_e values

In this chapter, the output results (V - H - M) of the 3D failure envelope are normalized following the dimensionless approach as introduced by Butterfield (1999), as shown in Eq. (4.4)

$$\frac{V}{s_{uTC}B}, \frac{H}{s_{uTC}B}, \frac{M}{s_{uTC}B^2} = f(r_e) \quad (4.4)$$

where $V/s_{uTC}B$ is the non-dimensional vertical load coefficient; $H/s_{uTC}B$ is the non-dimensional horizontal load coefficient; $M/s_{uTC}B^2$ is the non-dimensional bending moment coefficient, and r_e represents the anisotropic ratio.

To build a 3D failure envelope through dimensionless variables ($V/s_{uTC}B$, $H/s_{uTC}B$, $M/s_{uTC}B^2$), the dimensionless vertical load factor, $V/s_{uTC}B$, is broken into the ratio between the levels of vertical load mobilization (V/V_0) and $V_0/s_{uTC}B$, as shown in Eq. (4.5):

$$\frac{V}{s_{uTC}B} = \frac{V}{V_0} \times \frac{V_0}{s_{uTC}B} \quad (4.5)$$

where V_0 is the ultimate load of a strip foundation under the pure vertical loading (pure V) for each of the soil profiles. The investigated 3D failure envelope ($V/s_{uTC}B$, $H/s_{uTC}B$, $M/s_{uTC}B^2$) is changed to 3D failure envelope (V/V_0 , $H/s_{uTC}B$, $M/s_{uTC}B^2$), as mentioned by Gottardi and Butterfield (1993), Houlsby et al. (1999), Taiebat et al. (2002), and Gourvenec et al. (2003).

Fig. 4.3 indicates a three-dimensional interaction plot within the (V/V_0 , $H/s_{uTC}B$, $M/s_{uTC}B^2$) space is used to express the undrained capacity of strip footings under general loading.

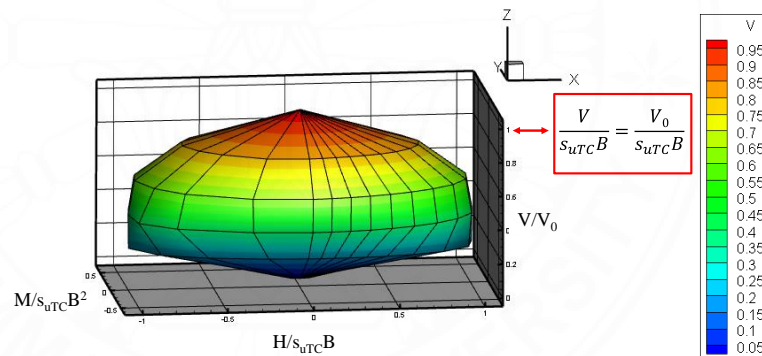


Figure 4.3 3D failure envelope through dimensionless variables (V/V_0 , $H/s_{uTC}B$, $M/s_{uTC}B^2$)

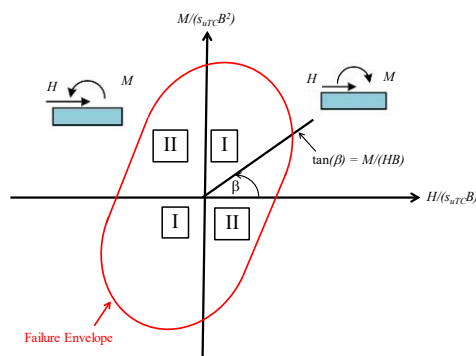


Figure 4.4 Establishing the 2D failure envelope for a specified value of V/V_0

As illustrated in Figure 4.4, two separate scenarios are analyzed for each envelope within the $(H/s_{uTC}B, M/s_{uTC}B^2)$ space, as emphasized in prior research conducted by Keawsawasvong and Ukritchon (2016). The value of β represents the angle assessed starting from the positive of the horizontal axis (refer to Fig. 4.4) (Salencon and Pecker 1995; Keawsawasvong and Ukritchon 2016). In this chapter, the value of β is selected within the ranges from 0 to 180 degrees with intervals of 10 degrees, serving as the loading constraint for the FELA.

4.3 Methodology

4.3.1 Finite element limit analysis (FELA)

In this section, numerical solutions of rigid strip footing in anisotropic clays under combined loads are calculated utilizing the OptumG2 FELA software (Krabbenhoft et al. 2015). The typical model geometry for this problem is shown in Fig. 4.5. The interaction between the soil and footing is represented in the model by incorporating “no-tension” and “full-tension” conditions. Soil elements are modeled by AUS material. Limiting boundary conditions for the model were assessed at a distance of $6B$ lateral from the footing center and $3B$ below the soil surface. The breadth (B) of the strip foundation was maintained at 1.0 m throughout the research. The right and left boundaries of the domain are specified as roller supports, permitting vertical movement while restricting lateral rotation and horizontal displacement. The top ground surface is unrestricted, allowing for movement and deformation without any imposed constraints. On the other hand, the fixed support is employed to the base boundary of the model, providing complete restraint against rotation and translation.

The auto-mesh adaptive method in OptumG2 is employed to enhance the precision and dependability of numerical solutions. In this chapter, five adaptive iterations of mesh adaptivity are employed. This study initiated this process with 5,000 elements and concluded with 10,000 elements to narrow the gap between lower and upper bounds solutions, yielding more precise and dependable outcomes. An illustration of the application of the auto-mesh adaptive method for the strip footing problem is depicted in Fig. 4.6. In total, there are 840 analysis cases considering no-tension and full-tension interface with ranges of $(r_e, V/V_0, \beta)$, as shown in Table. 4.1.

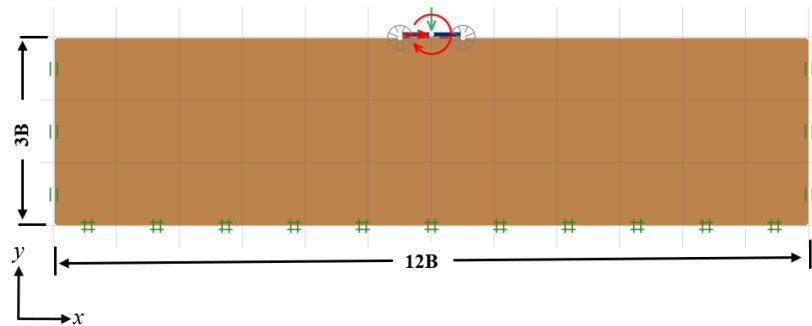


Figure 4.5 FELA model of a strip footing under general loading in OptumG2

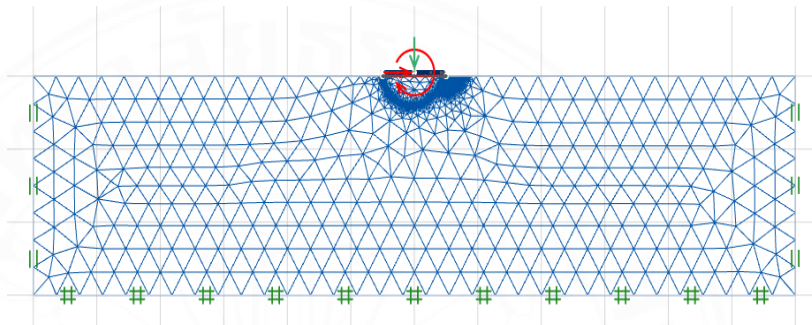


Figure 4.6 An adaptive mesh pattern and boundary conditions

Table 4.1 Ranges of input parameters

Variable	Selected values
V/V_0	0, 0.2, 0.4, 0.6, 0.8
r_e	0.5, 0.6, 0.7, 0.8, 0.9, 1
β	0, 15, 30, 40, 50, 60, 70, 80, 90, 100, 110, 120, 130, 140, 150, 160, 170, 180

4.3.2 Artificial Neural Networks (ANNs)

Artificial Neural Networks (ANNs) is a complex system inspired by human brain learning (Shams et al. 2020; Kapadia et al. 2021; Cherif et al. 2023; Saint-Fleur et al. 2023). Fig. 4.7 shows the architecture of a feed-forward, so-called multiple-layer network with the input, hidden, and output layers, respectively. Each node consists of its weights and biases, which are adjusted in the training process following the Levenberg-Madquardt backpropagation algorithm (Hagan et al. 1994).

This chapter proposes the application of artificial neural networks to determine the dimensionless horizontal load (H/s_uTCB) and bending moment factor (M/s_uTCB^2) of the strip footing on anisotropic clay under combined loading through the

correlation equations. The inputs to the ANN model include (r_e), the vertical load mobilization (V/V_0), and different (β) angles, respectively.

The ANN is implemented in MATLAB code (Beale et al. 2010), in which the size of input layer $Q \times 3$ (r_e , V/V_0 , β) and the outcomes layer $Q \times 2$ (H/s_{uTCB} , M/s_{uTCB}^2), where Q is number 420 cases. In this chapter, 420 data points are randomly allocated into three sets: 70% for training, 15% for validation (to prevent overfitting), and 15% for an independent test of network performance. As a result, optimal weight and bias are generated and applied to investigate the sensitive analysis of each parameter toward their outputs (Abdollahi et al. 2021; Ahmad et al. 2022; Kumar et al. 2023).

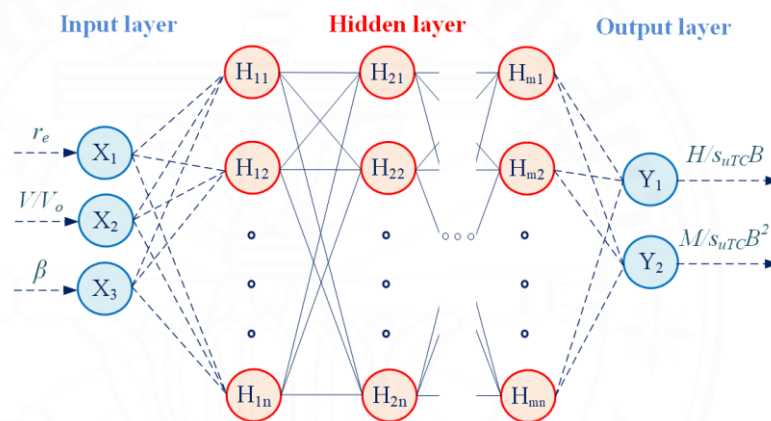


Figure 4.7 The architecture of multi-layer networks

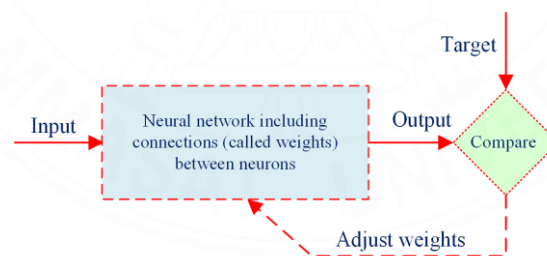


Figure 4.8 The process of backpropagation

4.4 Result and comparison

4.4.1 Verification

A comparison of failure envelopes of strip footing in clay in the (H/s_{uTCB} , M/s_{uTCB}^2) space with the cross-section of $V/V_0 = 0$ (no vertical load) between the present study and the numerical solution suggested by Ukritchon et al. (1998) has

been presented in Fig. 4.9. It is noted that the case of isotropic clays is carried out by setting $r_e = 1$, meaning that the AUS failure criterion becomes the Tresca failure criterion, respectively. The agreement between the previous solutions and the results derived from the FELA analysis in the failure envelopes in $(H-M)$ space of strip footing, is in good agreement with Ukritchon et al. (1998).

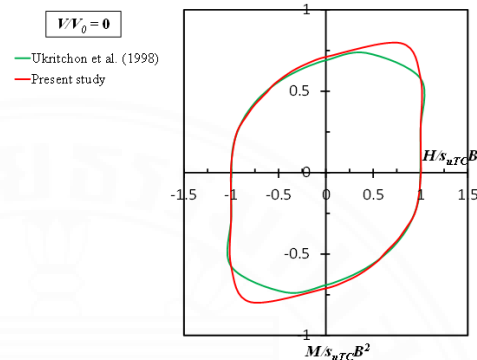


Figure 4.9 A comparison of determining failure envelope of strip footing in isotropic clay between the current study and the results from Ukritchon et al. (1998)

4.4.2 FELA result

As shown in Figs. (4.10-4.15) for cases of r_e [0.5, 0.6, 0.7, 0.8, 0.9, 1], the magnitude of the failure envelopes is most significantly impacted by the values of r_e . An increase in r_e results in an increase in the size of the failure envelope. An increase in (r_e) leads to a greater obliqueness of the failure envelopes. For full-tension cases, the case of $V/V_0 = 0$ expresses the largest $H-M$ failure envelope for all values of r_e . Note that the contour dimensions are similar in both $V/V_0 = 0$ and 0.2 in full-tension conditions

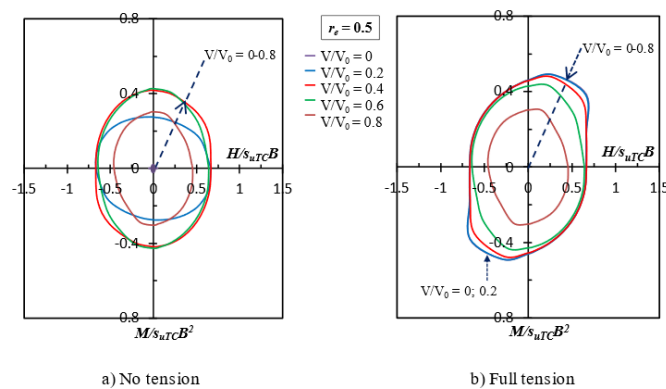
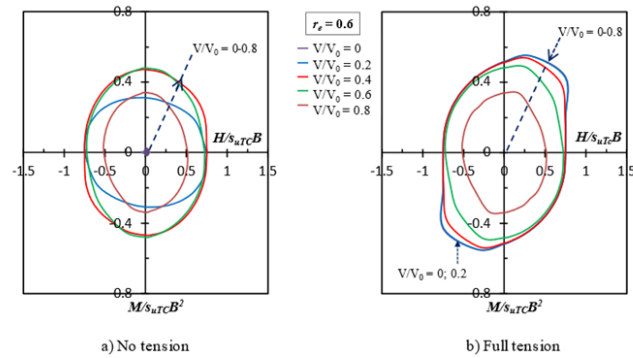
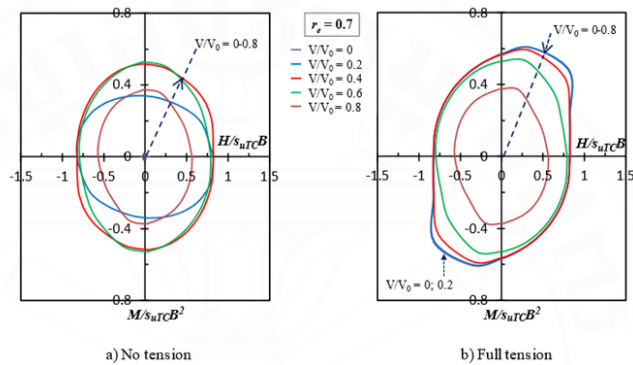
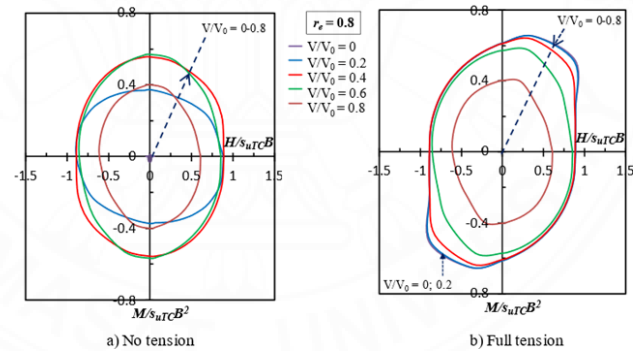
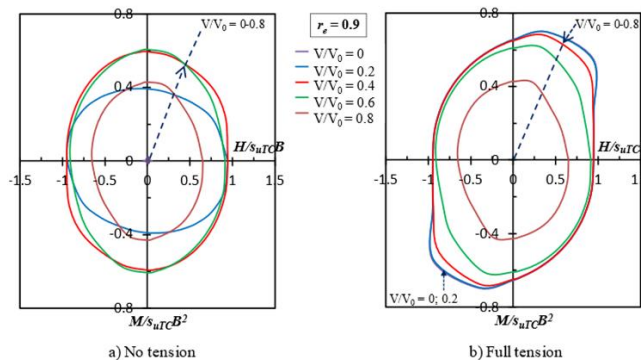


Figure 4.10 Failure envelope of strip footings with $r_e = 0.5$

Figure 4.11 Failure envelope of strip footings with $r_e = 0.6$ Figure 4.12 Failure envelope of strip footings with $r_e = 0.7$ Figure 4.13 Failure envelope of strip footings with $r_e = 0.8$ Figure 4.14 Failure envelope of strip footings with $r_e = 0.9$

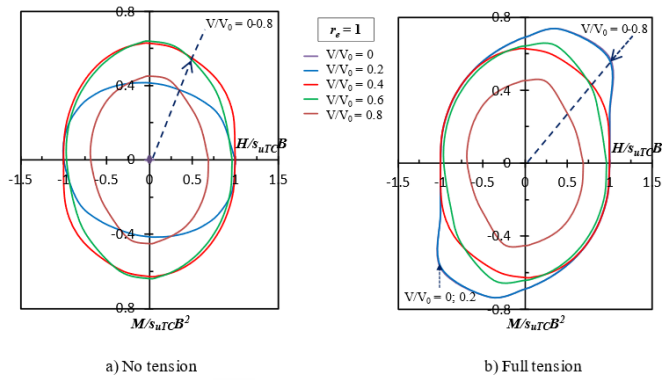


Figure 4.15 Failure envelope of strip footings with $r_e = 1$

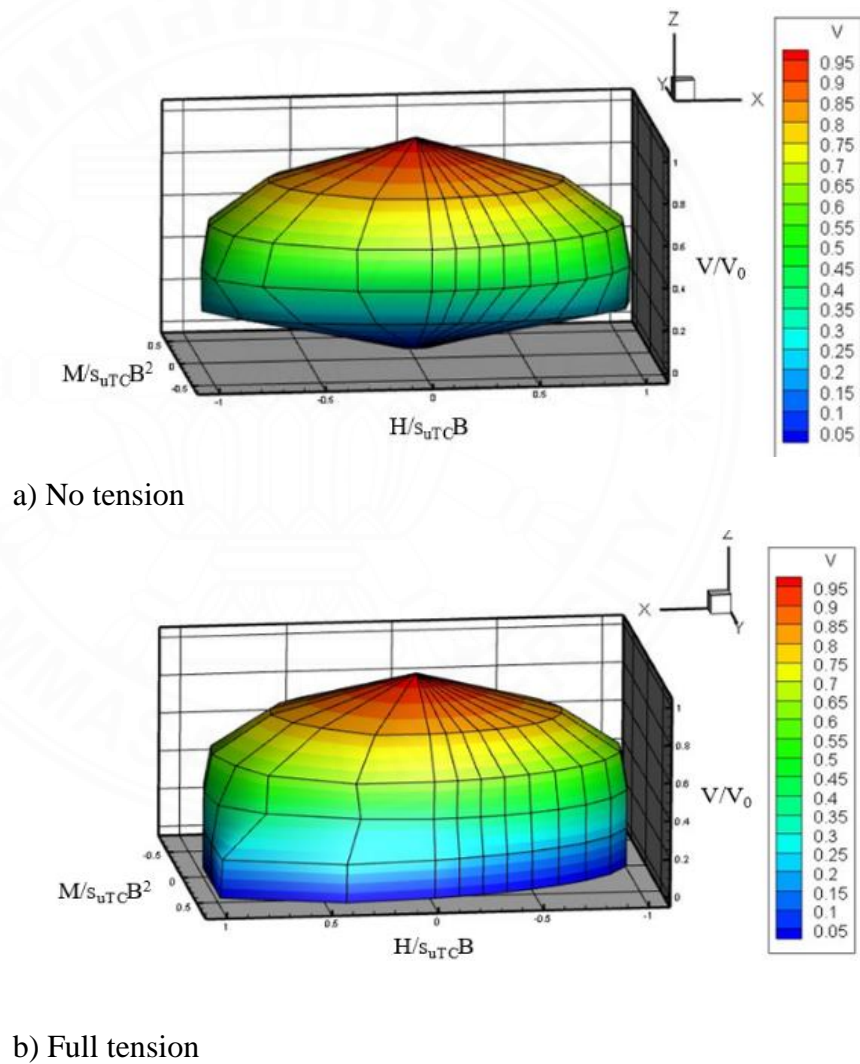


Figure 4.16 Examples of 3D failure envelopes

The size of the 3D envelope of the full-tension case is much bigger and asymmetry than another no-tension case when the value of V/V_0 is less than 0.6.

The reason for these problems can be explained through the failure mechanism, as illustrated in Figs. (4.17-4.18).

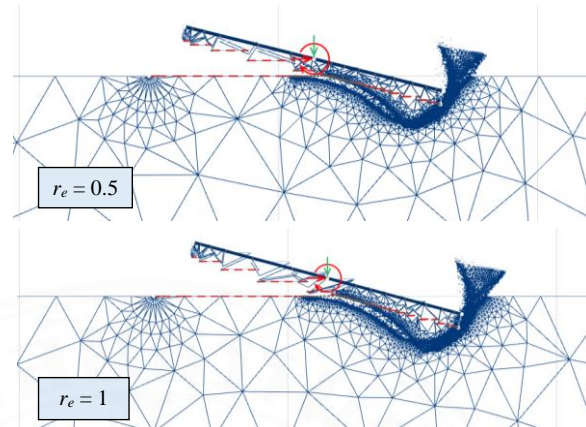


Figure 4.17 Failure patterns of strip footings with no-tension interface, where $V/V_0 = 0.4$

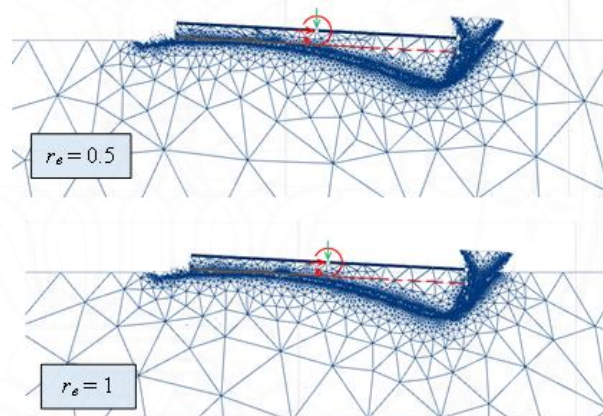


Figure 4.18 Failure patterns of strip footings with full-tension interface, where $V/V_0 = 0.4$

To enhance the understanding of the failure mechanisms, a comparison of failure mechanisms under varying combinations of horizontal load and bending moment is shown in Fig. 4.19 for cases of full-tension interface. In the first quadrant, where the (β) angle ranges from 0 to 90 degrees, the maximum moment capacity is achieved since both horizontal load and moment are applied on the footing in the same direction. The plastic zone expands as (β) approaches 90 degrees, leading to a wedge-scoop-wedge mechanism similar to the one. These results are compatible with system normalcy, and the processes produce $H-M$ plane envelopes with positive and negative gradients.

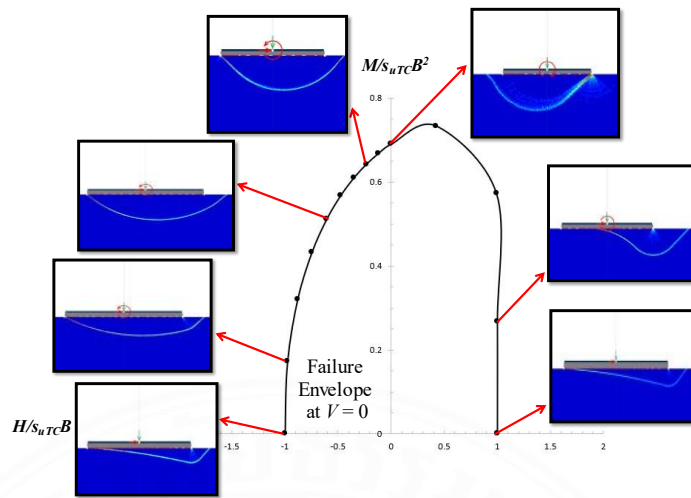


Figure 4.19 Examples of failure mechanisms of a strip footing

4.4.3 ANN result

As shown in Fig. 4.20 for full-tension cases, the number of neurons is varied from 1 to 11 to investigate the impact of a number of neurons on the value of MSE and R^2 . The optimal selection for the full-tension conditions uses 8 neurons in the hidden layer for the ANN architecture with the MSE and R^2 equal to 0.0006 and 0.9988, respectively. The analysis process will be carried out similarly in the cases of no-tension, as shown in Fig. 4.21. The optimal ANN model for cases of no-tension is also 3-8-2. After the updating weights and bias in the training process, these optimal Neural Networks Constants values are shown in Tables 4.2 and 4.3.

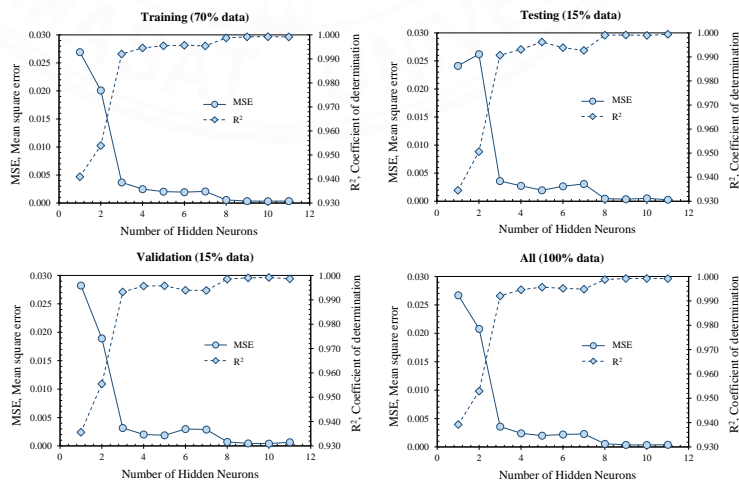


Figure 4.20 The Mean Square Error (MSE) and Coefficient of determination (R^2) of the number of selected hidden neurons for full-tension cases

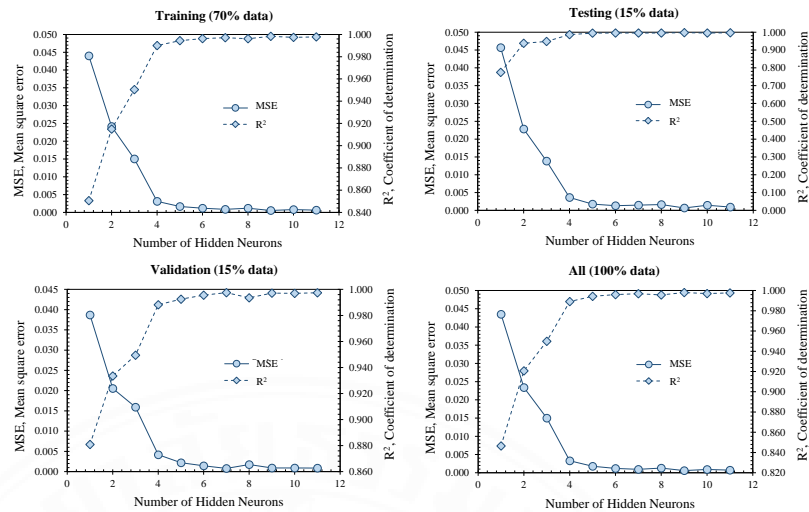


Figure 4.21 The Mean Square Error (MSE) and Coefficient of determination (R^2) of the number of selected hidden neurons for no-tension cases

Table 4.2 Weights and Bias of the ANN model for full-tension cases

Neuron	W^{12}			b^{12}	W^{23}		b^{23}	b^{23}
	Input variables				Output			
	r_e	V/V_0	β		$H/s_{uTC}B$	$M/s_{uTC}B^2$		
1	0.1797	1.9045	1.0338	-2.7454	0.5397	0.1665		
2	0.1110	0.0156	0.6109	-1.1192	-5.1610	-2.2676		
3	-0.0370	0.2793	-0.0609	0.1564	-4.2810	-8.6456		
4	-0.0467	0.8478	4.0437	2.4346	-0.1956	-0.3536		
5	0.0201	0.6080	-0.0225	0.2852	2.1402	3.9972	-1.1005	-6.2164
6	0.1289	-0.1028	-3.4743	-3.0350	1.4163	-3.9180		
7	0.0676	-0.0838	1.6644	-2.5432	2.1471	-4.0740		
8	-0.1151	0.0591	4.2550	3.6564	1.3008	-2.2507		

Table 4.3 Weights and Bias of the ANN model for no-tension cases

Neuron	W^{12}			b^{12}	W^{23}		b^{23}	b^{23}
	Input variables				Output			
	r_e	V/V_0	β		$H/s_{uTC}B$	$M/s_{uTC}B^2$		
1	-0.1113	1.3186	0.8764	-1.9487	0.5434	1.4619		
2	-0.0354	0.5096	1.2221	-1.2101	-0.5360	-6.3716		
3	0.0609	-0.8485	0.4135	-0.7521	-4.9188	-0.7339		
4	0.1039	0.5186	0.4006	0.8191	2.8575	0.1561		
5	-0.0217	0.7081	0.4908	0.4999	-2.9650	1.6990	1.9494	-5.9733
6	-0.0306	-0.2940	-2.2199	1.4255	0.2433	-2.1190		
7	-0.0054	-0.6041	0.4395	-1.0194	7.0870	-2.0440		
8	0.1035	-0.7711	1.1624	1.1374	-0.3559	2.1609		

To be more precise and applicable for practical engineering, the detailed calculation described below shows an example of calculating the predicted value of $(H/s_{uTC}B, M/s_{uTC}B^2)$ in the case of $(r_e = 0.5, V/V_0 = 0, \beta = 0)$, with full-tension condition. FELA results for the case of $(r_e = 0.5, V/V_0 = 0, \beta = 0)$ with $(H/s_{uTC}B, M/s_{uTC}B^2) = (0.6665, 0.1786)$ where ANN prediction is $(0.7003, 0.2020)$. The error between the ANN prediction and the FELA results is less than 12.00%.

According to the above calculation, all predictions for both full-tension and no-tension cases from the ANN model are compared with FELA results, as shown in Fig. 4.22 and Fig. 4.23, respectively. The prediction results agreed with the FELA results, with MSE and R^2 values of $(0.0006, 99.88\%)$ and $(0.00013, 99.57\%)$ for full-tension and no-tension conditions, respectively.

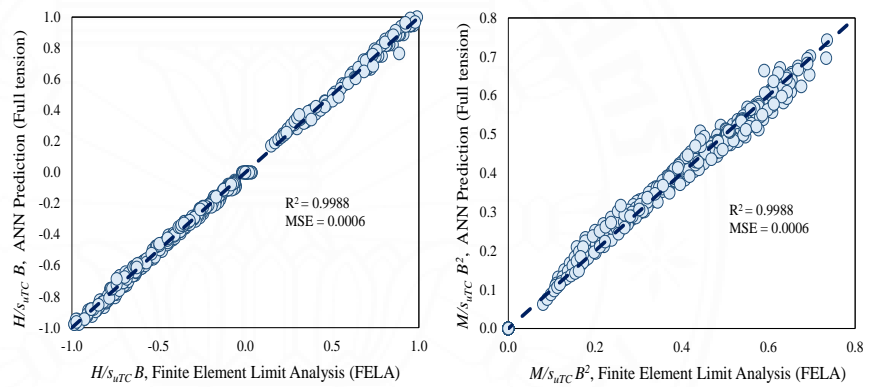


Figure 4.22 The comparison between the results of ANN predictions and FELA results for the full-tension cases

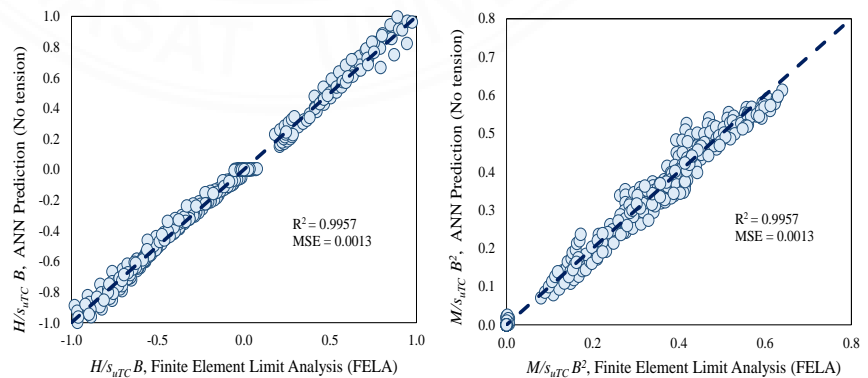


Figure 4.23 The comparison between the results of ANN predictions and FELA results for the no-tension cases

4.5 Conclusion

The failure envelopes of strip footing in anisotropic clay under general loading (V - H - M) by applying the lower bound solutions of 2D FELA and artificial neuron networks (ANN). The results of the paper are summarized as follows:

1. An increase in (r_e) makes the 2D failure envelope bigger but does not affect much on the shape failure envelope.
2. The results show that the shape of the 3D failure envelope between no-tension and full-tension cases is different. In the upper part of the 3D failure envelope where V/V_0 is larger than 0.6, 3D failure envelopes in full-tension cases are larger than those in no-tension cases.
3. The ANN model is applied in this study to propose an efficient tool for practical engineering to build 2D space (H/s_{uTCB} , M/s_{uTCB}^2) and 3D failure envelope (V/V_0 , H/s_{uTCB} , M/s_{uTCB}^2).

CHAPTER 5

FAILURE ENVELOPES OF RING FOUNDATIONS

5.1 Introduction

Ring foundations are often used for onshore applications with examples being cooling towers, storage tanks, radar stations, transmission towers, chimneys, silos, and bridge piers (Chen et al. 2021). Figure 5.1 presents a schematic of ring footing to support a wind turbine structure.

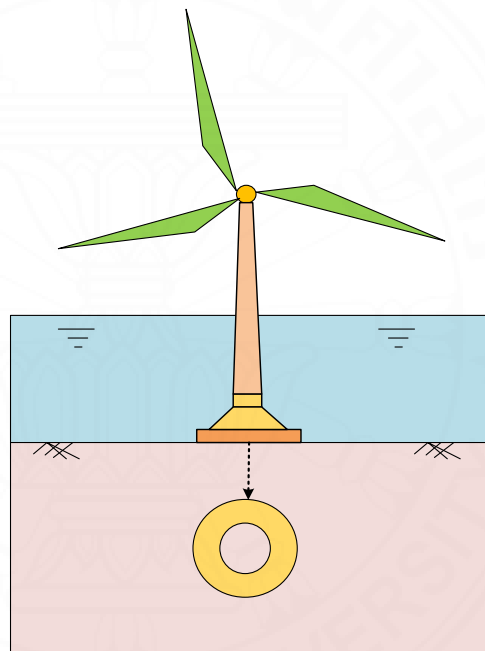


Figure 5.1 Ring foundation as an offshore structure

Early investigations into the behavior of ring foundations under individual static loads were conducted through experimental tests by several researchers, such as Saha (1978), Hataf and Razavi (2003), Boushehrian and Hataf (2003), and El Sawwaf and Nazir (2012). Other analytical studies, such as Kumar and Ghosh (2005), Zhao and Wang (2008), Remadna et al. (2017), and Kumar and Chakraborty (2015), Nayyeri et al. (2016) and Keshavarz and Kumar (2017), Benmebarek et al. (2012), Lee et al. (2016), Birid and Choudhury (2021), Keawsawasvong et al. (2022), and Yodsomjai et al. (2021a). Krabbenhoft et al. (2019) developed a novel failure criterion, termed the anisotropic undrained shear (AUS) model, akin to the formulations of Casagrande and

Carrillo (1944) and Lo (1965). Moreover, some researchers have developed new limit analysis solutions for determining the stability of foundations in anisotropic clays via the AUS model (e.g., Yodsomjai et al., 2021b; Ukritchon et al., 2020).

Although there have been comprehensive investigations into the failure envelopes of skirted shallow foundations under various loading conditions (e.g., Bransby and Randolph, 1998; Chanda et al., 2021; Gourvenec, 2008; Fiumana et al., 2019; Bransby and Yun, 2009; Mana et al., 2013; Zhuang et al., 2019; Liu et al., 2014; Shen et al., 2016; Dunne and Martin, 2017; Du et al., 2022; Liu et al., 2021; Zhao 2022 and 2024), most of them have focused on circular foundations, neglecting the effects of ring foundations under similar loading conditions.

Chapter 5 aims to study the failure envelopes of ring foundations of varying shapes and sizes placed on anisotropic clay. This research builds upon the prior work of Birid and Choudhury (2022) and Shen et al. (2016) to establish a new research framework. The failure loci developed here, termed AUS failure loci, offer valuable insights for designers to evaluate different load combinations under critical failure conditions. This chapter further utilizes artificial neural networks (ANNs) with their optimization performance through various models, such as ANN-ABC (artificial bee colony), ANN-ICA (imperialist competitive algorithm), and ANN-ALO (ant lion optimizer) (see, e.g., Le et al., 2019; Karaboga, 2005; Kumar et al., 2022; Jitchaijaroen et al., 2023; Reddy, 2017; Keawsawasvong et al., 2023; Gholami et al., 2022; Tran et al., 2023; Panomchaiyath et al., 2023). These techniques aim to develop an optimal predictive model for predicting the failure boundaries of ring foundations within complex engineering scenarios involving anisotropic clay in V - H - M space.

5.2 Problem definition

Shown in Figure 5.2 is the problem statement of a rigid ring foundation placed on the surface of an anisotropic ground. The ring foundation has an internal radius (r_i) and an external radius (r_o), and it is subjected to combined V - H - M loads. The outer diameter $B = 2r_o$, the surface area $A = \pi(r_o^2 - r_i^2)$, and the ratio between internal and external radii (r_i/r_o) would define the size of the ring foundation.

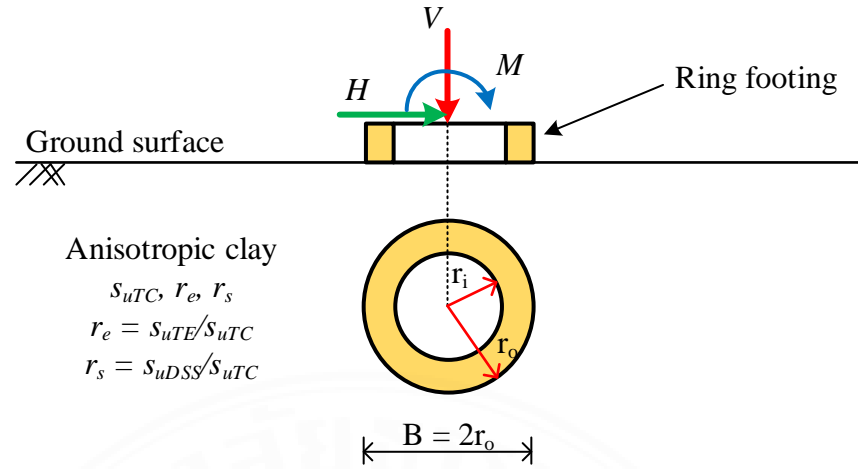


Figure 5.2 Problem definition of ring foundation under general loadings

Numerical results of V - H - M are presented as dimensionless load parameters ($V/s_{uTC}A$, $H/s_{uTC}A$, and $M/s_{uTC}AB$) throughout the paper. Various combinations of V - H , V - M , and H - M loads thus created failure boundaries for different scenarios. In cases of combined V - H - M loading, portions of the vertical capacity were distributed ($V/V_0 = 0, 0.25, 0.5, \text{ and } 0.75$) onto the ring foundation's surface, followed by varied fixed ratios of H - M loads to assess different H - M combinations at failure under varying vertical loads. This approach has been well-documented in the literature by Gourvenec and Randolph (2003), Bransby and Randolph (1998), Tan (1990), Chen et al. (2022), and Shen et al. (2016).

Applying Butterfield (1999) dimensionless approach reveals that two dimensionless input factors predominantly lead to the normalized output outcomes (V - H - M) represented in Eq. (5.1).

$$\frac{V}{s_{uTC}A}, \frac{H}{s_{uTC}A}, \frac{M}{s_{uTC}AB} = f\left(\frac{r_i}{r_o}, r_e\right) \quad (5.1)$$

where the radius ratio is denoted as (r_i/r_o) and the anisotropic strength coefficient is presented as (r_e). The specified dimensionless values for these parameters in the research are $r_i/r_o = 0, 0.2, 0.4, 0.6$, and $r_e = 0.5, 0.6, 0.7, 0.8, 0.9$, and 1.

To construct a 3D failure envelope using dimensionless variables ($V/s_{uTC}A$, $H/s_{uTC}A$, $M/s_{uTC}AB$), the dimensionless vertical load factor, $V/s_{uTC}A$, is split into two components: the ratio of vertical load mobilization levels (V/V_0) and $V_0/s_{uTC}A$, as described in Eq. (5.2).

$$\frac{V}{s_{uTC}A} = \frac{V}{V_0} \times \frac{V_0}{s_{uTC}A} \quad (5.2)$$

5.3 Methodology

5.3.1 Finite element limit analysis (FELA)

The model geometry for this problem is shown in Fig. 5.3, showcasing a half-cut view of a ring foundation on clay. The modeling involved using rigid plate elements for the ring footing and solid components to represent the clay layer. Different ring foundations are considered with varying inner-to-outer radius ratios (r_i/r_o) at 0, 0.2, 0.4, and 0.6 for the circular rigid shells. The AUS model is employed as a failure criterion for anisotropic clay. The interface between the bottom of the ring foundation and the soil was assumed to be fully rough, ensuring complete bonding between the footing and the soil. A sufficiently large domain size is used to eliminate possible boundary effects. In this case, the soil domain is 7B in width and the depth is 4B below the soil surface, providing ample area for failure mechanisms to fully take effect. The load reference point (LRP) can be positioned at the midpoint of the foundation at the ground level in the case $r_i/r_o = 0$. The side boundaries were constrained against lateral deformation but allowed free vertical displacement. The model's bottom edge was fixed to prevent lateral and vertical displacement, as indicated in Fig. 5.3. The mesh underwent three adaptive refinement steps, starting with 5000 elements and concluding with 10000 elements. This is considered as a good balance between computational efficiency and accuracy (e.g., Xiao et al., 2018; Chen and Liu, 2018; Zhang et al., 2022; Yu et al., 2018; Payan et al., 2022). Specifically, the initial and target number of elements, the number of adaptive iterations, and the adaptivity control parameter (such as shear dissipation) must be defined (Krabbenhoft et al., 2015; Ciria et al., 2008). Notably, both fixed and multiplier load concepts are essential for applying and analysing simulations using Optum G3 (Krabbenhoft et al., 2015). This methodology has been widely applied to several geotechnical stability problems by Shiau et al. (2020, 2022, 2023).

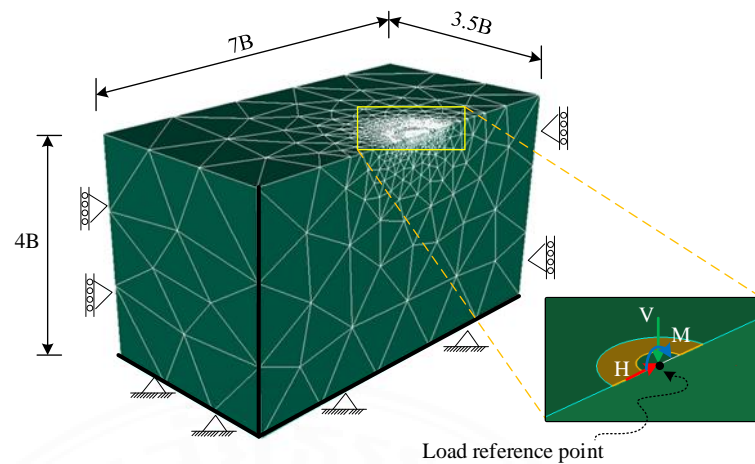


Figure 5.3 Problem domain showing adaptive mesh design and boundary conditions

In view of the computation process, the limit load (V_0) was initially assessed under a solely vertical load condition before proceeding with the V - H analysis (Tan, 1990). This process yields the limiting vertical loads (V_0) for different r_e and r_v/r_o values. The V - H load combination analysis was then followed by applying a fixed horizontal distributed load while optimizing the vertical limit load (V). Similar analyses were conducted to create V - M failure boundaries on the centreline of the footing. These solutions have been explained by Birid and Choudhury (2022). Specifically, the analyses involved applying horizontal loads in both the positive and negative directions, with the moment used solely in the positive direction to produce H - M failure, as shown in Fig. 5.4. Note that the unit moment (1 kNm/m) was applied along the centerline of the ring footing.

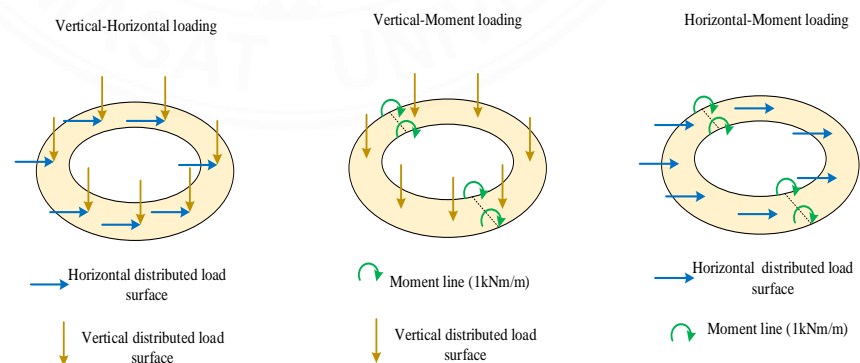


Figure 5.4 Illustration of V - H , V - M , and H - M loadings

To simulate combined V - H - M loading, a percentage of the vertical capacity ($V/V_0 = 0, 0.25, 0.5, \text{ and } 0.75$) was applied to the surface of the ring foundation as a distributed load. At a certain value of V/V_0 , it can be seen as a two-dimensional

failure envelope in the H - M space (H/s_{uTCA} , M/s_{uTCAB}). Figure 5.5 shows the analysis of two distinct situations for each envelope in the (H/s_{uTCA} , M/s_{uTCAB}) space, as highlighted in a previous study conducted by Keawsawasvong and Ukritchon (2016).

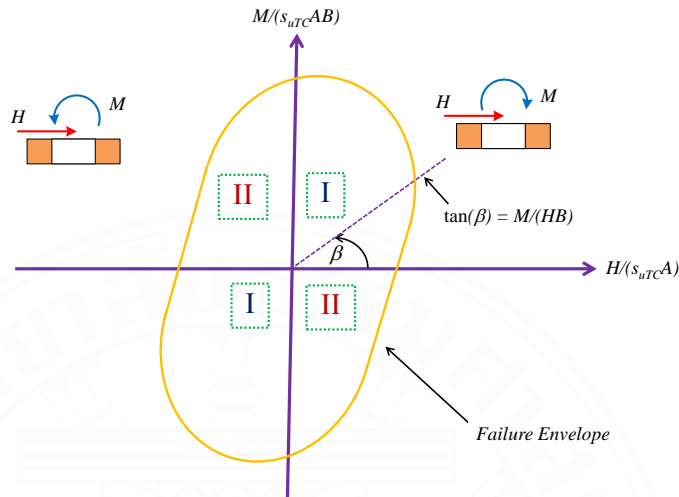


Figure 5.5 Analysis of the 2D failure envelope for a given V/V_0 value

To construct a 3D failure envelope, the initial step involves determining the 2D failure envelope for four different cross-sections of $V/V_0 = 0, 0.25, 0.5,$ and 0.75 , using the dimensionless parameters H/s_{uTCA} and M/s_{uTCAB} . This study selects the value of β as the loading limit for the FELA, which is within the range of 0 to 180 degrees. Table 2 illustrates the total number of 960 ($4 \times 6 \times 4 \times 10$) analysis cases with ranges of $(r_i/r_o, r_e, V/V_0, \beta)$ to compute $(H/s_{uTCA}, M/s_{uTCAB})$. The failure envelopes for ring foundations can be normalized as $V/V_0, H/H_0,$ and M/M_0 , respectively (Gourvenec and Randolph, 2003; Gourvenec, 2008; Birid and Choudhury, 2022). The ultimate loads refer to the loads that occur when there is pure loading, such as when $H = M = 0$ for V_0 , $M = V = 0$ for H_0 , and $V = H = 0$ for M_0 .

Table 5.1 Parameter ranges for the input

Variable	Selected values
r_i/r_o	0, 0.2, 0.4, 0.6
r_e	0.5, 0.6, 0.7, 0.8, 0.9, 1
V/V_0	0, 0.25, 0.5, 0.75
β	$0^0, 15^0, 30^0, 60^0, 90^0, 100^0, 120^0, 140^0, 160^0, 180^0$

A schematic of the scoop mechanism is shown in Fig. 5.6(a). As the horizontal load increases and the moment capacity decreases, the scoop decreases, and the wedges extend across the foundation base, transitioning into a sliding mechanism. For vertical load mobilization on a ring foundation, failure dominated by a moment rather than a horizontal load appears as a scoop–wedge mechanism (Fig. 5.6b). After the maximum moment is mobilized, a Brinch Hansen mechanism is generated, as shown in Fig. 5.6c (Brinch Hansen, 1970; Gourvenec, 2007). Failure more strongly influenced by the horizontal load than the moment results in an asymmetric wedge mechanism, as shown in Fig. 5.6d.

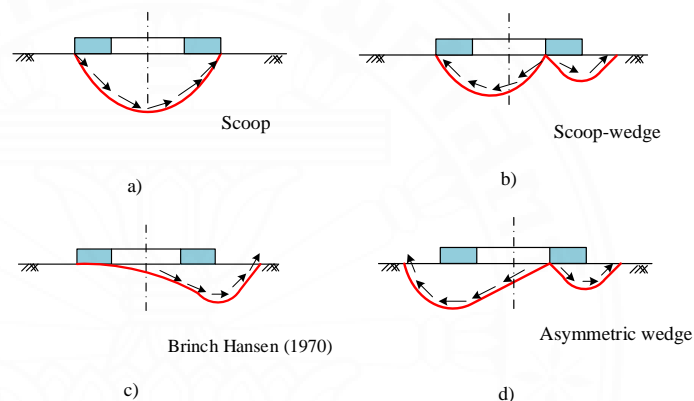


Figure 5.6 Examination of the failure mechanisms for H–M loading with (a) scoop, (b) scoop-wedge, (c) Brinch Hansen (1970), and (d) asymmetric wedge

5.3.2 Artificial Neural Network (ANN) and Hybrid ANN

Several studies, including those by Rabi et al. (2023), Nguyen et al. (2023), Kumar and Samui (2008), Armaghani et al. (2015), and Kumar et al. (2022), have highlighted the importance of using ANNs across different civil engineering applications. Figure 5.7 shows a typical structure of a feed-forward network comprising input, hidden, and output layers. Note that each node within carries its weights (W) and biases (b) that are adjusted during training via the Levenberg–Madquardt (LM) backpropagation algorithm (Hagan et al., 1994). These functions, known for enhancing convergence speed and model performance, are employed for the linear transfer functions of the hidden and output layers, respectively (Sirimontree et al., 2022). This research uses both activation functions to build artificial neural network (ANN) models according to Eq. (5.3).

$$\text{Output} = \sum_{i=1}^{N_h} W^{2,i} \text{tansig} \left(\sum_{j=1}^J W^{1,i} x^j + b^{1,i} \right) + b^{2,i} \quad (5.3)$$

In this work, artificial neural networks are used to calculate the failure envelope ($H/s_{uTC A}$, $M/s_{uTC AB}$) for a ring footing on anisotropic clay subjected to combined loading. The inputs for the ANN model consist of parameters such as (r_e), vertical load mobilization (V/V_0), the proportion angle (β), and various (r_i/r_o) radius ratios. More detailed information on the use of the Levenberg–Madquardt (LM) algorithm to train feedforward networks can be found in Marquardt (1963) and Hagan et al. (1994).

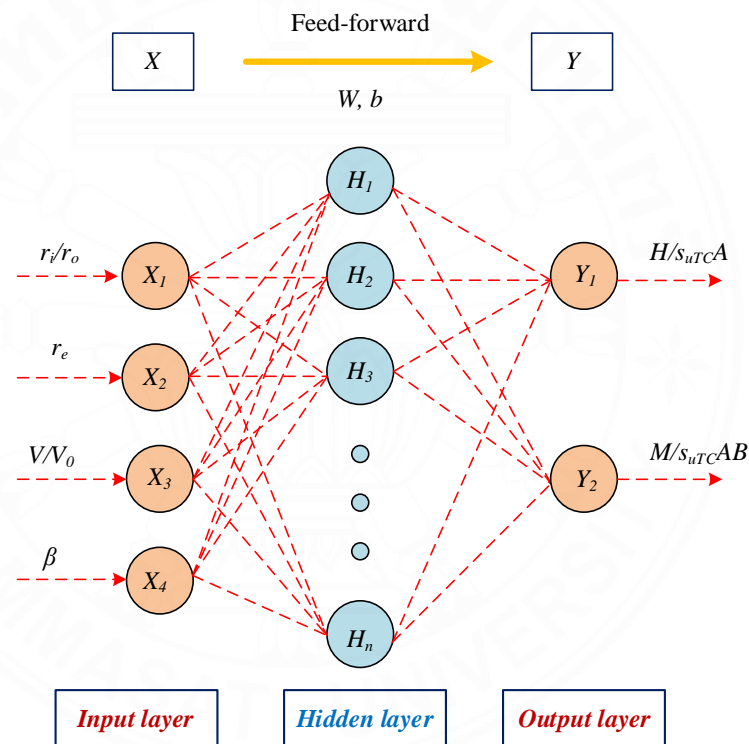


Figure 5.7 Model architecture for an ANN (Artificial Neural Network)

To optimize artificial neural network models, three unique combinations of soft computing techniques, namely, artificial neural networks with an artificial bee colony (ANN-ABC), artificial neural networks with an imperialist competitive algorithm (ANN-ICA), and artificial neural networks with an ant lion optimizer (ANN-ALO), are adopted in this paper to assess the failure contour of a ring footing on anisotropic clay. These methods have been well addressed in earlier studies by Le et al. (2019), Sangjinda et al. (2024) and Kumar et al. (2022). In brief, the ABC optimization algorithm, inspired by nature and introduced by Karaboga (2005), is a

swift and straightforward method in AI and is a metaheuristic optimization approach that handles discrete and continuous problem types.

The imperialist competitive algorithm (ICA) is a method for optimizing solutions inspired by social and political systems, particularly the dynamics between imperialist powers and their colonies (Le et al., 2019; Atashpaz-Gargari and Lucas, 2007).

The ALO algorithm draws inspiration from the distinctive behavior of antlion larvae during their food search, a concept introduced by Mirjalili (2015). The ALO method serves as a solution for complex engineering challenges, functioning as a global search optimization strategy, as highlighted by Mirjalili et al. (2017). For an in-depth understanding of the developed algorithm, interested individuals can refer to literature sources such as Mirjalili (2015) and Narasimhulu et al. (2020). The flow chart presented in Fig. 5.8 illustrates the model's development process.

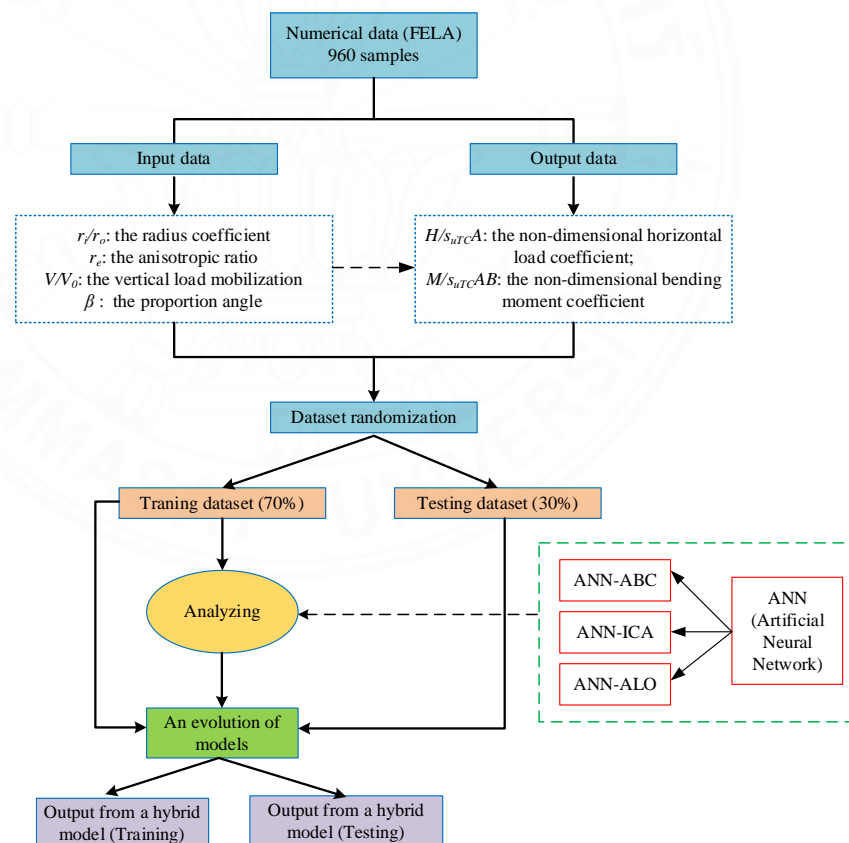


Figure 5.8 Flow diagram showing the development of an ANN-hybrid model

In this study, the numerical data are split randomly into two segments: training and testing sets, in which 70% (672 data points) of the entire dataset

is chosen randomly and 30% (288 data points) is set aside for testing the developed models (Kumar et al., 2024). The details of the descriptive statistics for the failure envelope of the ring foundation are presented in Table 5.2.

Table 5.2 Statistical details of the variables used in the failure envelope

Index	r_i/r_o	r_e	V/V_0	β	H/s_{uTCA}	M/s_{uTCAB}
Minimum	0.0	0.5	0.0	0.0	-1.204	0.0
Maximum	0.6	1	0.75	180	1.205	1.537
Mean	0.3	0.75	0.375	89.5	0.029	0.406
Median	0.3	0.75	0.375	95	-0.017	0.391
Standard Deviation	0.223	0.171	0.279	58.93	0.683	0.305
Kurtosis	-1.36	-1.27	-1.36	-1.28	-1.24	0.565
Skewness	0.0	0.0	0.0	-0.057	0.077	0.696

The ANN model employs a hidden layer (N_{HL}) with the number of hidden neurons (N_h) ranging from 5 to 10. The activation functions use a hyperbolic tangent for the hidden layer and a linear function for the output layer. The optimization algorithm is characterized by hyperparameters such as a population or swarm size (N_P) of 30, a maximum of 10,000 iterations (I_{max}), and weight and bias values constrained between -1 and 1 for both the lower and upper bounds (LB and UB).

5.4 Result and comparison

5.4.1 Verification

The validation of the calculated solutions for the vertical bearing capacity factor obtained from the present study for ring footing resting on isotropic clay ($r_e = 1$) is shown in Fig. 5.9. The verification process includes the examination of the solutions proposed by Lee et al. (2016) using the finite element method (FEM), the finite element limit approach introduced by Birid and Choudhury (2022), and the two-dimensional finite element limit analysis conducted by Keawsawasvong et al. (2022) under axisymmetric conditions. Fig. 5.9 shows that the current solutions are slightly greater than the earlier solutions by Birid and Choudhury (2022) and Keawsawasvong et al. (2022) because different mathematical types for failure criteria were employed. Nevertheless, the outcome closely corresponds to the findings of Lee et al. (2016). The

proposed method can be deemed highly effective, as it results in a percentage difference of less than 7% compared with previous investigations.

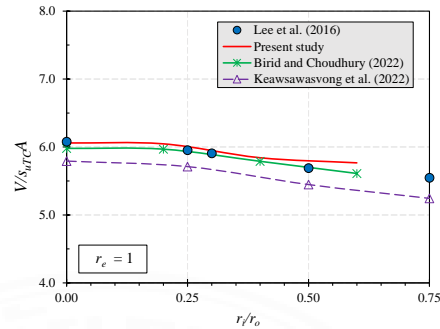


Figure 5.9 Comparison of the results with those of existing studies on ring foundations resting on isotropic clay

The first validation involves examining the V - H failure envelope of the ring footing on isotropic clay, with r_i/r_o values of 0.4 and r_e value of 1. This is shown in Fig. 5.10. The numerical results show that the present solutions are similar to those of Bird and Choudhury (2022) by approximately 2.8%. The second verification show that the present solutions are consistently greater than those of Bird and Choudhury (2022) by approximately 0.4% to 5.7%. The last verification show some discrepancy between the two solutions, mostly because different mathematical criteria are employed for determining failure. Overall, the present FELA solutions align well with those from Bird and Choudhury (2022) across all combinations of V - H , V - M , and H - M loads.

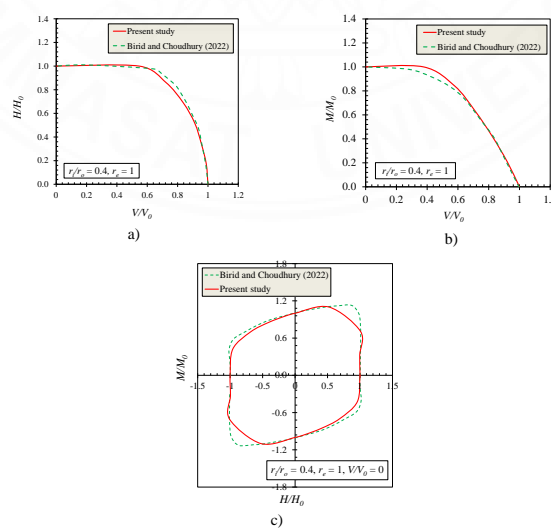


Figure 5.10 Comparison of the V - H - M failure envelopes between the current study and those in Bird and Choudhury (2022) with (a) V - H loading, (b) V - M loading, and (c) H - M loading

5.4.2 FELA results

The comprehensive solutions for the failure envelope of a ring foundation on anisotropic clay are presented in Figs. 5.11, 5.12, 5.13, and 5.14 for V - H , V - M , and H - M loading spaces, respectively. In Fig. 5.11, four different ring geometries (r_i/r_o) are investigated to explore the shape and dimensions of the failure envelopes. The maximum value of V/s_{uTCA} decreases from 6.06 to 5.77 as the ring foundation area decreases (i.e., r_i/r_o increases from 0 to 0.6).

The numerical results for the V - M loading space are presented in Fig. 5.12. This study follows the same approach as in Fig. 5.11, where four different ring geometries (r_i/r_o) are investigated for various (r_e) = 0.5 to 1.0. Notably, both the ratios of V/s_{uTCA} and M/s_{uTCAB} increase as the value of r_e increases for all the ring shapes (r_i/r_o). In addition, the value of M/s_{uTCAB} increases substantially as (r_i/r_o) increases, resulting in an expansion of the failure envelopes.

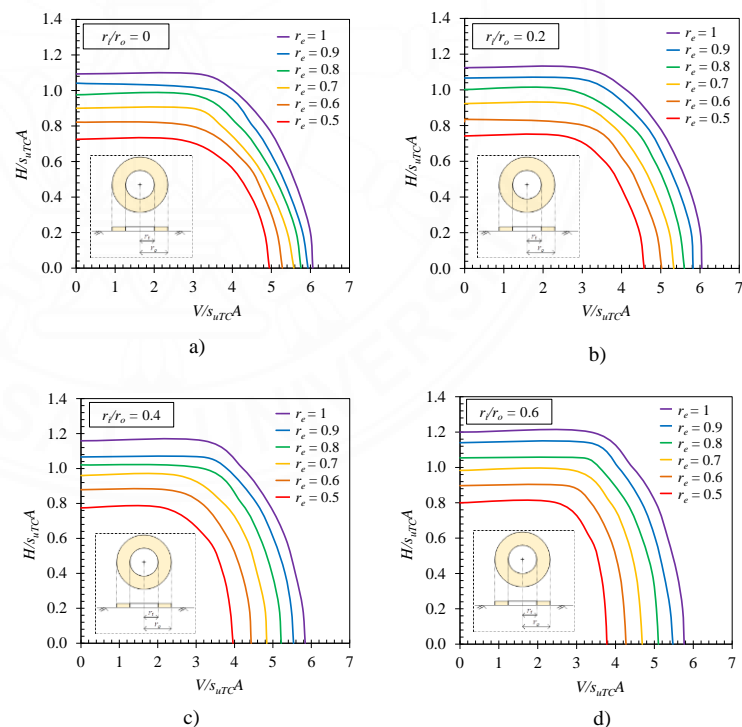


Figure 5.11 Failure envelope under V - H loadings with (a) $r_i/r_o = 0$, (b) $r_i/r_o = 0.2$, (c) $r_i/r_o = 0.4$, (d) $r_i/r_o = 0.6$

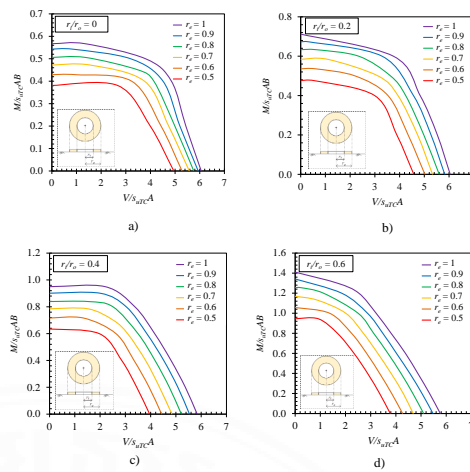


Figure 5.12 Failure envelopes under V-M loadings with (a) $r_i/r_o = 0$, (b) $r_i/r_o = 0.2$, (c) $r_i/r_o = 0.4$, (d) $r_i/r_o = 0.6$

Figure 5.13 shows the variations in the failure envelopes in the H – M loading spaces at $V/V_0 = 0.5$. Similar to Figs. 5.11 and 5.12, these variations consider ring geometries (inner to outer radius ratio, r_i/r_o) and anisotropic ratios (r_e). While symmetric failure envelopes are observed for V – H and V – M loading conditions (Figs. 5.11 and 5.12), the H – M failure envelopes exhibit an asymmetric trend when subjected to both positive and negative horizontal loads (H/s_{uTCA}). Note that the failure envelope tends to increase as the r_i/r_o ratio increases. Additionally, note that the moment capacity M/s_{uTCAB} and horizontal capacity H/s_{uTCA} increase with increasing r_e for all ring geometries.

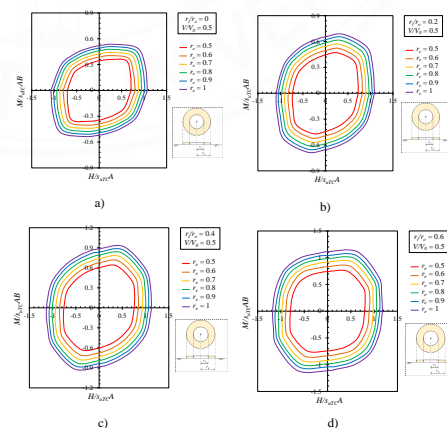


Figure 5.13 Failure envelope of the ring footing for combined loading analysis under H– M loading for $V/V_0 = 0.5$ and (a) $r_i/r_o = 0$, (b) $r_i/r_o = 0.2$, (c) $r_i/r_o = 0.4$, and (d) $r_i/r_o = 0.6$

The combined effects of V - H - M forces acting on the ring foundation are further investigated in Fig. 5.12. This analysis aims to create $(V/s_{uTC A})$ - $(H/s_{uTC A})$ - $(M/s_{uTC AB})$ failure load contours and thereafter to develop three-dimensional failure surfaces. The 2D and 3D contours for these failure loading combinations on ring foundations with $r_i/r_o = 0.2$, $r_e = 0.5, 0.7, 0.9$, and 1 are shown in Fig. 5.12(a-d), respectively. Notably, the total area of the failure envelope decreases as the value of (V/V_0) increases.

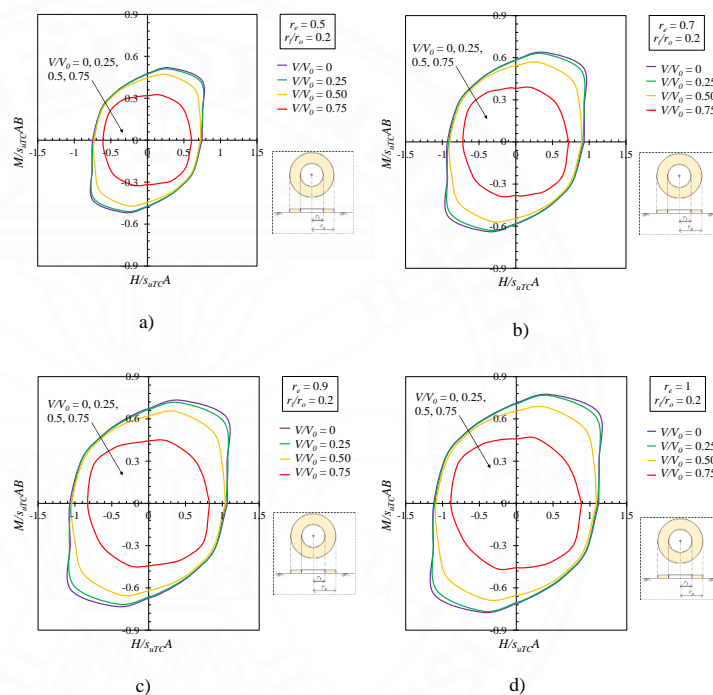


Figure 5.14 2D diagram representation of the combined failure loads for a ring foundation with $r_i/r_o = 0.2$ and (a) $r_e = 0.5$, (b) $r_e = 0.7$, (c) $r_e = 0.9$, (d) $r_e = 1$

Fig. 5.14 can be further extended to 3D failure contour envelopes, as shown in Figs. 5.15 and 5.16. Figure 5.15(a-d) illustrates the 3D failure envelope $(V/V_0, H/s_{uTC A}, M/s_{uTC AB})$ in the cases where $r_i/r_o = 0.4$ and $r_e = 0.5, 0.6, 0.8$, and 1, respectively. Increasing the value of r_e expands the 3D failure envelope, which assumes the shape of a vertically rotating ellipsoid. The plots for both $r_e = 0.5, 0.6, 0.8$, and 1 show that the size of the contour decreases as V/V_0 increases. The 3D failure surfaces for the cases $r_e = 0.7$ and $r_i/r_o = 0, 0.2, 0.4$, and 0.6 are presented in Fig. 5.14. The shape and size of the 3D failure envelope expand when the value of r_i/r_o increases. This can

be explained by the horizontal and moment capacity in the 2D failure envelope increasing with increasing r_i/r_o , as shown in Fig. 5.13.

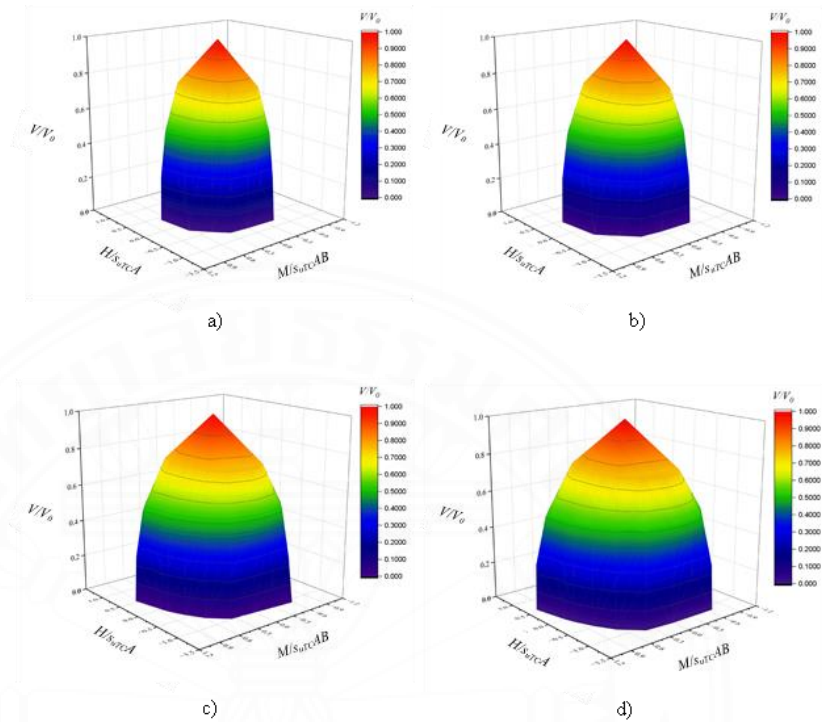


Figure 5.15 3D diagram representation of the combined failure loads for a ring foundation with $r_i/r_o = 0.4$ and (a) $r_e = 0.5$, (b) $r_e = 0.6$, (c) $r_e = 0.8$, (d) $r_e = 1$

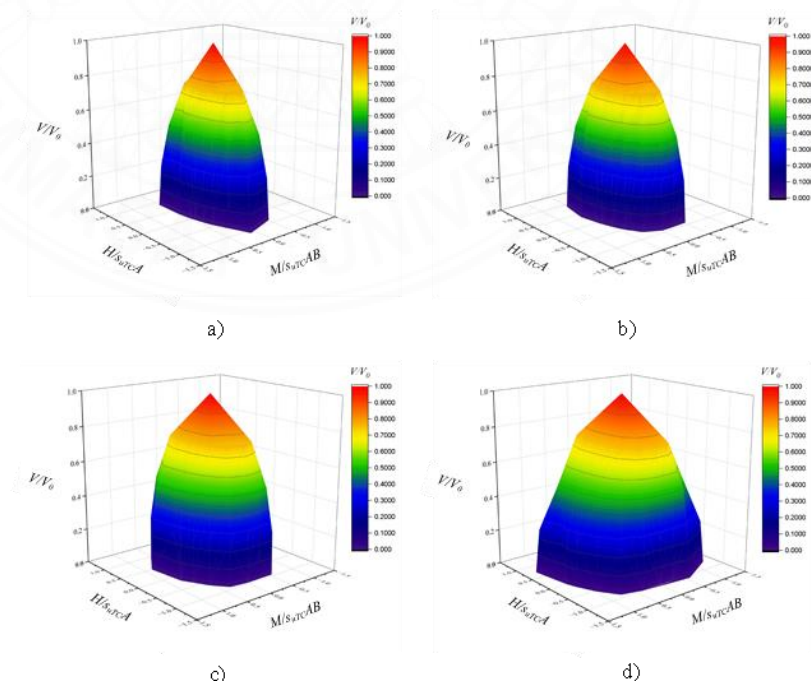


Figure 5.16 3D diagram representation of the combined failure loads for a ring foundation with $r_e = 0.7$ and (a) $r_i/r_o = 0$, (b) $r_i/r_o = 0.2$, (c) $r_i/r_o = 0.4$, (d) $r_i/r_o = 0.6$

Several demonstrations of the failure patterns (or mechanisms) are shown in Fig. 5.17 for foundations subjected to various load combinations (V - H - M). A pure bending moment failure is observed, where the ultimate moment M_0 is mobilized, whereas a pure horizontal mechanism is developed with the rigid translation of soil occurring in the back and bottom of the ring foundation, and H_0 is mobilized at $\beta = 0^\circ$.

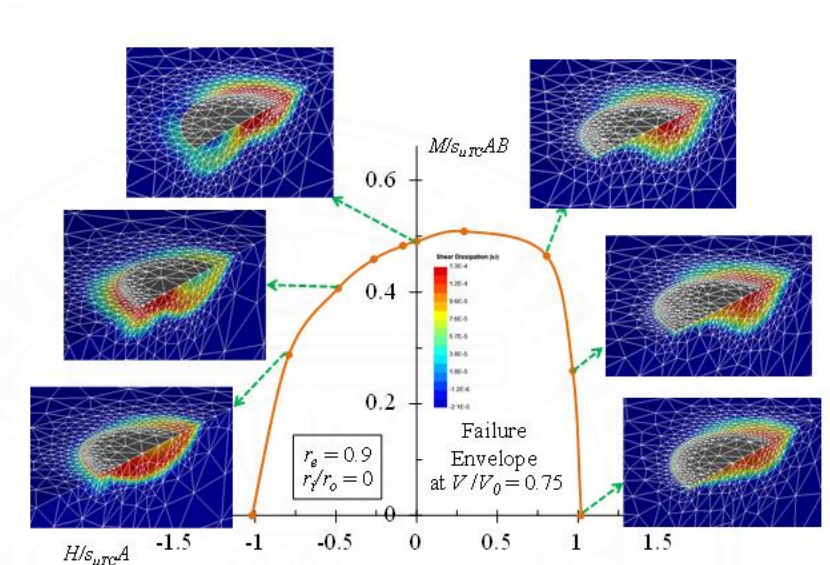


Figure 5.17 Failure mechanism of a 2D failure envelope of a ring foundation under general loading for $r_e = 0.9$, $r_i/r_o = 0$, and $V/V_0 = 0.75$

Figure 5.18(a-c) shows a comparison of failure mechanisms under different combinations of horizontal loads and bending moments, specifically for conditions where $r_e = 0.8$, $V/V_0 = 0.5$, and $r_i/r_o = 0.2, 0.4$, and 0.6 , respectively. The observed failure mechanisms result from both rotational and translational modes, providing practical insights for practical applications. At $\beta = 0^\circ$, a pure sliding mechanism occurs, where soil rigidly translates at the base of the footing due to interface conditions, and H_0 is activated. As β reaches 90 degrees, the plastic zone expands, resulting in a Brinch Hansen mechanism (see Fig. 5.6c). When β approaches 180 degrees, the shear plane transforms from Brinch Hansen mechanism to an asymmetric wedge mechanism at the back and bottom of the foundation for all the cases of $r_i/r_o = 0.2, 0.4$, and 0.6 (refer to Fig. 5.6c and 5.6d).

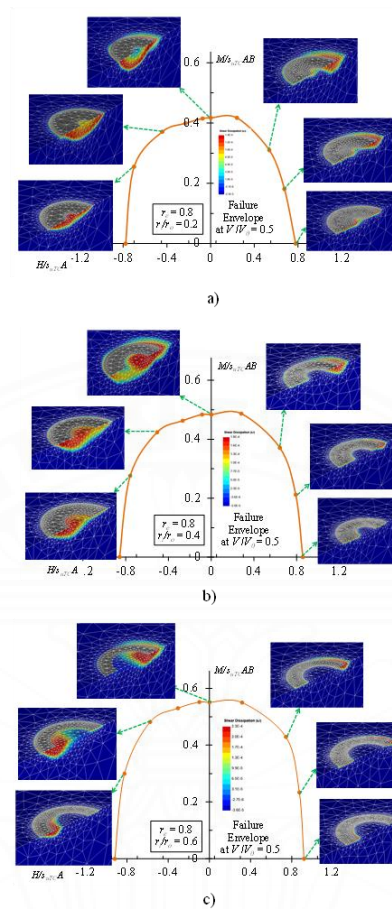


Figure 5.18 Failure mechanism of a 2D failure envelope of a ring foundation for $r_e = 0.8$, $V/V_0 = 0.5$ and (a) $r_i/r_o = 0.2$, (b) $r_i/r_o = 0.4$, (c) $r_i/r_o = 0.6$

5.4.3 ANN and ANN-hybrid optimal algorithm results

Regression plots that compare the FELA solutions and those predicted values of the dimensionless components $M/s_{uTC}AB$ and $H/s_{uTC}A$ are presented in Figs. 5.19 and 5.20 for various machine learning models (i.e., ANN-ABC, ANN-ICA, and ANN-ALO). Among the three models, the predicted values of ANN-ICA, shown as $M/s_{uTC}AB$ and $H/s_{uTC}A$, are more closely aligned with the line of equality, with $R^2 = 0.8803$ and 0.9749 , respectively. Similarly, ANN-ALO achieved R^2 values of 0.9555 for training and 0.9604 for testing $H/s_{uTC}A$, whereas ANN-ABC achieved R^2 values of 0.6175 for training and 0.6283 for testing $M/s_{uTC}AB$. Hence, the ANN-ICA model has exceptional performance $H/s_{uTC}A$ and $M/s_{uTC}AB$ in both the training and

testing stages, as evidenced by its better R^2 results. It can therefore be concluded that the ANN-ICA model possesses remarkable predictive capacity.

Taylor's diagram is a visual tool introduced by Taylor (2001) to compare various models against a reference dataset. In this chapter, Taylor's diagrams for the training and testing phases of M/s_{uTCAB} and H/s_{uTCA} are shown in Figs. 5.21(a) to (d), respectively, for the three models. While the other two models (ANN-ABC and ANN-ALO) cluster slightly farther from ANN-ICA, they still have good potential as a tremendous prediction mode, as the difference in correlation (R^2) among all the models in the training and testing phases is minor. Therefore, it can be concluded that the ANN-ICA model is considered the best performer in this study.

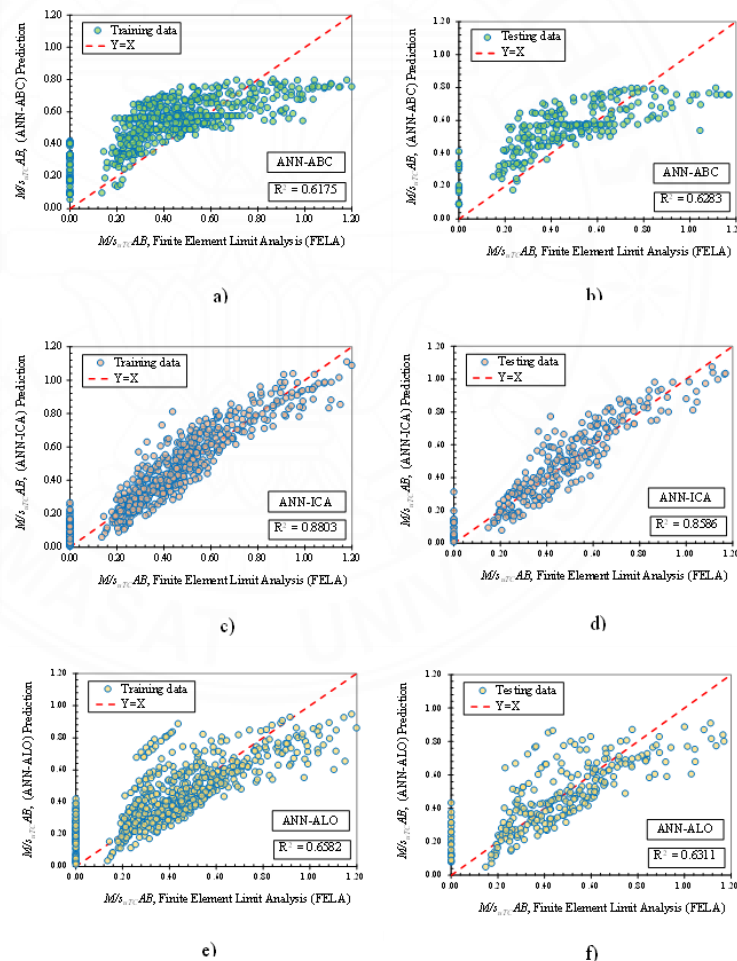


Figure 5.19 Comparison of actual FELA results with those from ANN for M/s_{uTCAB} with a) train ANN-ABC, b) test ANN-ABC, c) train ANN-ICA, d) test ANN-ICA, e) train ANN-ALO, f) test ANN-ALO

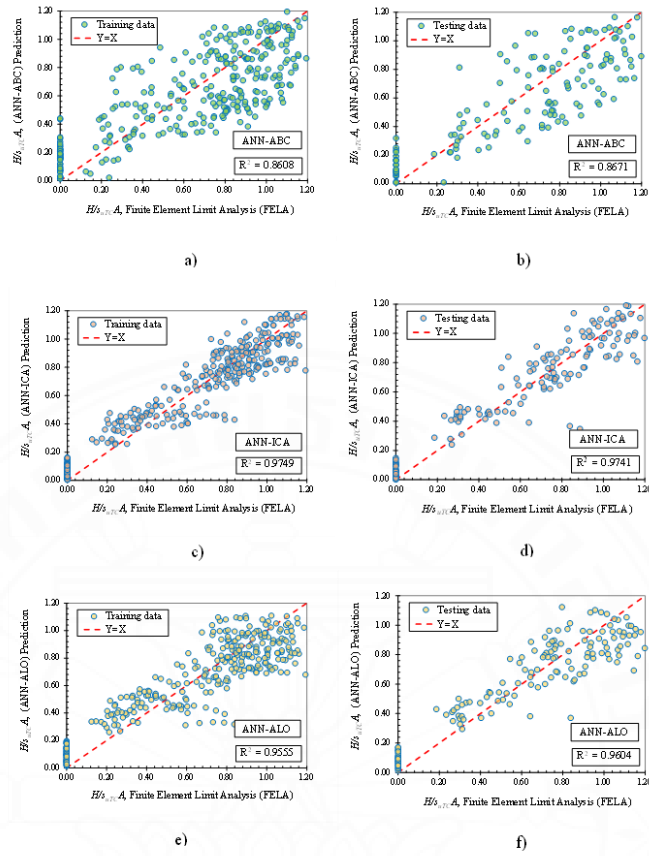


Figure 5.20 Comparison of actual FELA results with those from ANN for H/s_{uTCA} with a) train ANN-ABC, b) test ANN-ABC, c) train ANN-ICA, d) test ANN-ICA, e) train ANN-ALO, f) test ANN-ALO

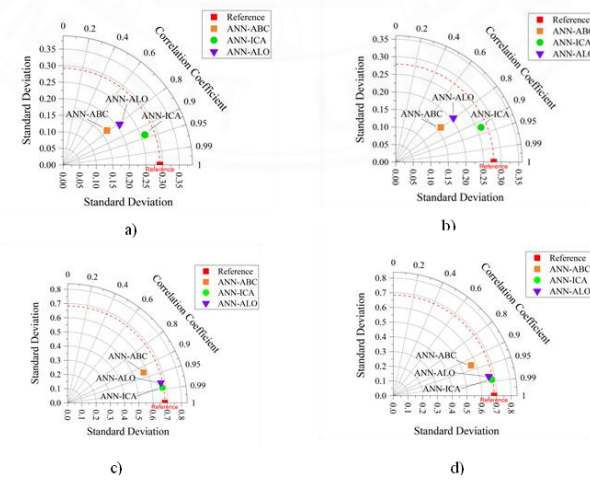


Figure 5.21 Taylor diagrams for a) M/s_{uTAB} training, b) M/s_{uTAB} testing, c) H/s_{uTCA} training, and d) H/s_{uTCA} testing

5.5 Conclusion

In general, an increase in the anisotropic ratio (r_e) or the inner and outer dimensions (r_i/r_o) would yield a larger failure envelope. The size of the H/s_{uTCA} - M/s_{uTCAB} space at various levels of vertical loading ($V/V_0 = 0, 0.25, 0.5, 0.75$) in the 3D failure envelopes increases by approximately 10% when r_e changes from 0.5 to 1 and approximately 4.2%-10.6% when r_i/r_o changes from 0.6 to 0.

A comparison of ANN models with different optimization algorithms revealed that ANN-ICA has the greatest efficiency in predicting the 3D failure envelope of ring foundations on anisotropic clay subjected to combined loadings (V - H - M) with high accuracy ($R^2 = 97.49\%$).



CHAPTER 6

FAILURE ENVELOPES OF CONICAL FOUNDATIONS

6.1 Introduction

The application of conical footings is a widely adopted practice for supporting both onshore and offshore structures. Various studies such as Craig and Chua (1990), Hossain et al. (2005), Gaudin et al. (2011), Chakraborty and Kumar (2015), Kaiser (2017), and Keawsawasvong (2022) have contributed to the understanding and development of this foundation type. Fig. 6.1 illustrates a typical conical footing application supporting ocean engineering structures (Byrne and Houlsby, 2003; Fan et al., 2021; Nguyen et al., 2022).

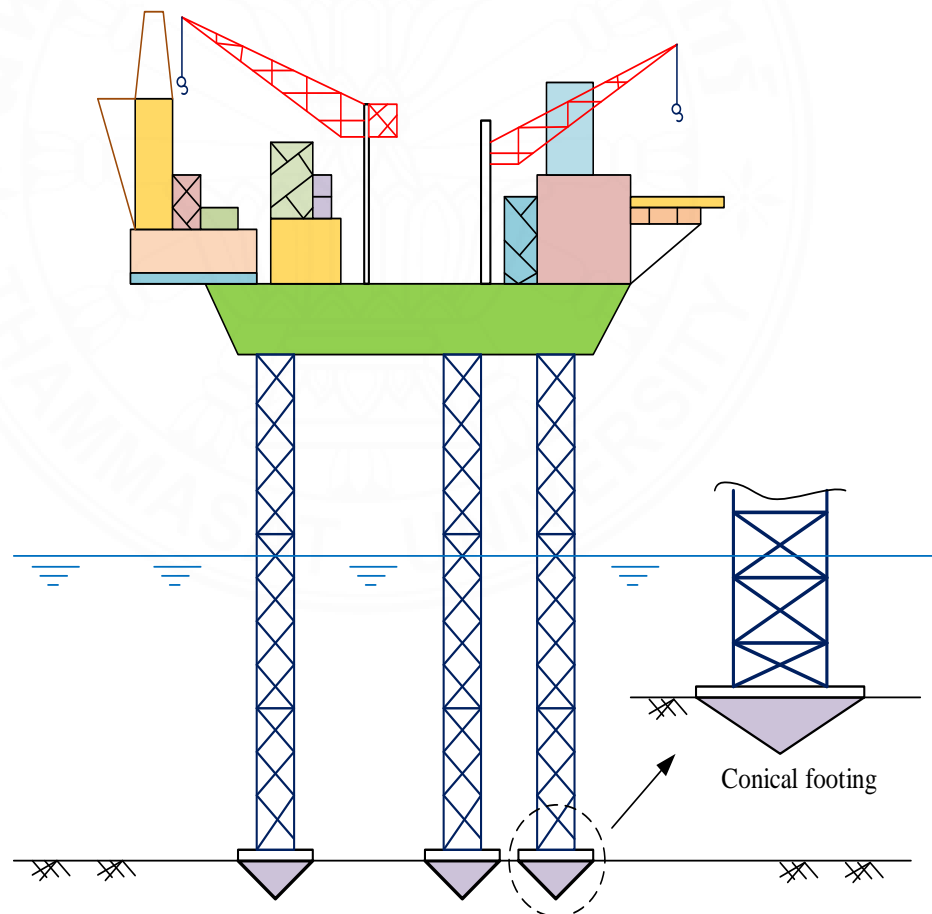


Figure 6.1 The application of conical foundation on ocean engineering systems

Several early studies have examined the performance of conical foundations under various static load conditions. Cassidy and Houlsby (2002) utilized

the method of characteristics (MoC) to study conical foundations in cohesionless soil, while Houlsby and Martin (2003) employed this technique for purely cohesive soils. White et al. (2008) and Hu et al. (2016) explored bearing capacity issues of conical footings considering different base roughness and apex angles. Khatri and Kumar (2009), as well as Chakraborty and Kumar (2016), employed finite element limit analysis (FELA) to calculate bearing capacity solutions for conical footings on cohesionless soil. Furthermore, Chakraborty and Kumar (2015) used FELA to derive bearing capacity factors for conical footings on cohesive-frictional soil, a method also adopted by Keawsawasvong (2022) and Nguyen et al. (2022) to determine bearing capacity factors for conical foundations on anisotropic and heterogeneous clay. Very recently, Tadayon et al. (2024) conducted experimental tests to examine conical foundation behavior on sand. Phuor et al. (2022) proposed finite element analysis (FEA) to assess the bearing capacity of rough conical foundations in cohesive-frictional soils.

While skirted shallow foundations have been thoroughly investigated under different loading conditions, including V , H , and M , as highlighted in studies by Bransby and Randolph (1998), Gourvenec and Randolph (2003), Gourvenec (2008), Bransby and Yun (2009), Taiebat and Carter (2000), Mana et al. (2013) Liu et al. (2014), Shen et al. (2016), Dunne and Martin (2017), Fiumana et al. (2019), Feng et al. (2014), Du et al. (2022), Taiebat and Carter (2010), and Birid and Choudhury (2022), very little research has focused on conical foundations under combined loading.

Chapter 6 aims to explore the three-dimensional effects of clay anisotropy on V - H - M failure envelopes for conical foundations with varying shapes. Following the previous research by Birid and Choudhury (2022), Gourvenec and Randolph (2003), and Shen et al. (2017), an innovative approach is used to determine the failure envelope capacity of conical foundations embedded in anisotropic clays. The numerical framework involves three-dimensional finite element limit analysis (3D FELA) with the AUS model. Several machine learning techniques such as the CATBoost, XGBoost, and GBM models are utilized to investigate the impact of each parameter on the capacity factor, which can be valuable for practitioners assessing the capacity of conical foundations under combined loading conditions.

6.2 Problem statement

A schematic representation of a conical foundation is shown in Fig. 6.2. The foundation is subjected to vertical force (V), horizontal force (H), and bending moment (M) for assessing the combined V - H - M failure envelope on anisotropic clay. The conical foundations are treated as a rigid material, and the cone apex angle (β) varies by adjusting cone height while keeping the footing diameter constant. It has a diameter of D , a surface area $A = \pi D^2/4$, and a variable cone apex angle (β) ranging from 90° to 180° . The current study considers a rough interface between the foundation and the soil.

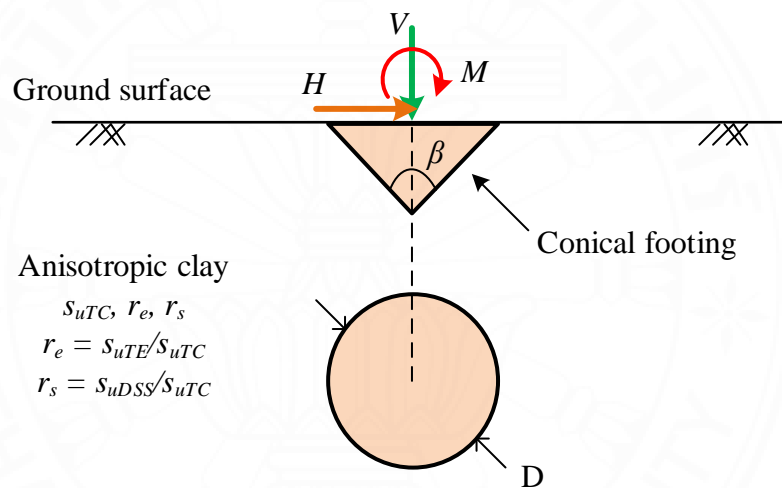


Figure 6.2 Problem definition of determining the failure envelope of a conical foundation subjected to general loading conditions

Three dimensionless load parameters, such as $V/s_{uTC}A$, $H/s_{uTC}A$, and $M/s_{uTC}AD$, are defined to create V - H - M failure envelopes. The process has been widely used in previous studies by Tan (1990), Gourvenec and Randolph (2003), Birid and Choudhury (2022), and Chen et al. (2022).

The dimensionless method introduced by Butterfield (1999) is utilized, and it enables the derivation of normalized output results (V - H - M) for conical foundations subject to various loading conditions in anisotropic clay, as shown in Eq. (6.1).

$$\frac{V}{s_{uTC}A}, \frac{H}{s_{uTC}A}, \frac{M}{s_{uTC}AD} = f(\beta, r_e) \quad (6.1)$$

where β represents the cone apex angle and r_e denotes the anisotropic strength ratio. The study examines the effects of these parameters with the different values of β at 90, 120, 150, and 180 degrees, while r_e ranges from 0.5 to 1 in increments of 0.1.

To construct a 3D failure envelope using dimensionless variables (V/s_{uTCA} , H/s_{uTCA} , $M/s_{uTCA}D$), the dimensionless vertical load factor, V/s_{uTCA} , is split into two components: the ratio of vertical load mobilization levels (V/V_0) and V_0/s_{uTCA} , as described in Eq. (6.2).

$$\frac{V}{s_{uTCA}A} = \frac{V}{V_0} \times \frac{V_0}{s_{uTCA}A} \quad (6.2)$$

The value of V_0 represents the maximum load that a conical footing can sustain under pure vertical loading (pure V) for each soil profile.

6.3 Methodology

6.3.1 Finite element limit analysis (3D FELA)

The FELA technique in the OptumG3 software (Krabbenhoft et al., 2015) is utilized in this study. Fig. 3 presents a typical adaptive mesh for a conical foundation on clay. The conical footing is represented by rigid elements, while the clay layer by solid elements that are in contact with the rigid-perfectly plastic AUS material with an associated flow rule. The interface between the foundation bottom and soil is assumed to be rough with full bonding. Various soil types with anisotropic parameters ($r_e = 0.5, 0.6, 0.7, 0.8, 0.9, \text{ and } 1$) are considered. It is to ensure that the chosen domain size is large enough to mitigate boundary effects. The soil domain extends 7D (seven times of the diameter D) in width and length and 4D beneath the surface. Standard boundaries are given to the sides where the velocities in the normal direction of each face are fixed. The top ground surface is allowed to move freely with unrestricted velocity boundary. Fixed support is applied to the base boundary of the model, ensuring a full restraint in all directions. See Fig. 6.3 for the adaptive mesh and boundary conditions.

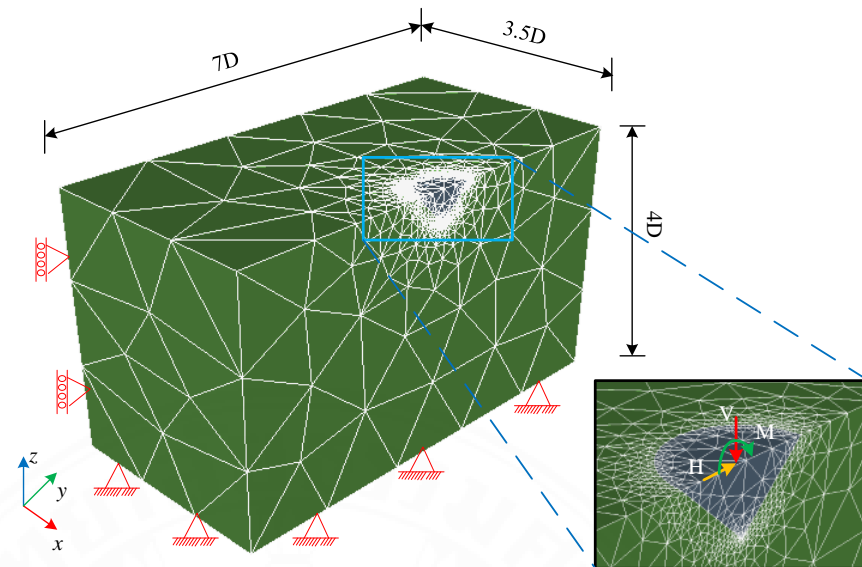


Figure 6.3 The issue area features an adaptive mesh structure and boundary limitations

Moreover, the current study utilizes auto-mesh adaptivity methodology to improve result accuracy, particularly in areas where shear dissipation differs significantly. As discussed by Ciria et al. (2008) and Ali (2017), this technique involves increasing the number of elements using three adaptive refinement steps. Starting with 5000 elements, the mesh ends with 10000 elements. This approach, introduced by Sloan (2013), enhances result accuracy by bracketing these bounds, enabling the estimation of an exact value.

Regarding the $V-H-M$ solution process, the current investigation conducts individual analyses for each failure point along the path (Tan, 1990; Gourvenec and Randolph, 2003; Taiebat and Carter, 2000). Note that the limiting vertical loads correspond to different parameter values, as presented in Table 1. The unit moment (1 kNm/m) was applied along the center line of the conical footing, as illustrated in Fig. 6.4.

Table 6.1 Dimensionless ultimate vertical load

r_e	0.5	0.6	0.7	0.8	0.9	1
$\beta = 90^0$	5.122	5.351	5.61	5.825	6.03	6.198
$\beta = 120^0$	4.989	5.273	5.501	5.709	5.887	6.032
$\beta = 150^0$	4.943	5.272	5.519	5.725	5.903	6.044
$\beta = 180^0$	4.948	5.282	5.576	5.756	5.936	6.059

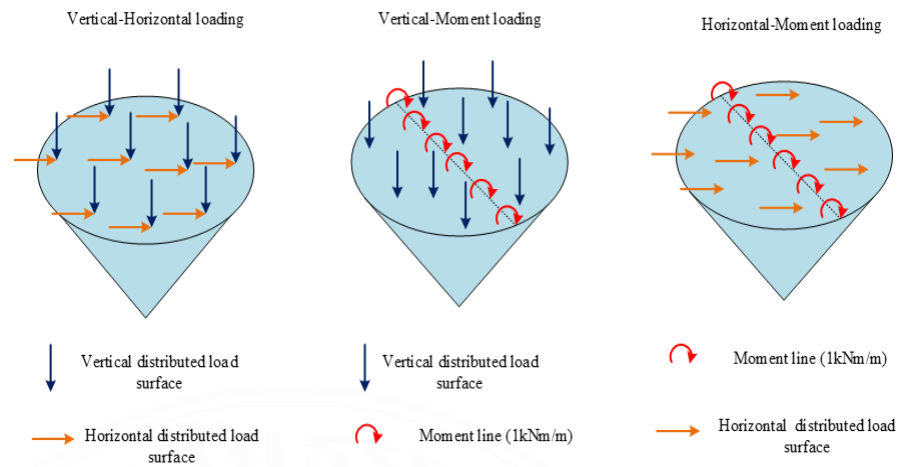


Figure 6.4 Examination of combined loading patterns involving V-H, V-M, and H-M loadings (after Birid and Choudhury, 2022)

The $V-H-M$ failure envelope is generated based on the $H-M$ analysis (Gourvenec, 2007; Chen et al., 2022). The contour of the 3D failure envelope corresponding to the vertical load cross-section. At a given value of V/V_0 , it can be seen as a 2D failure envelope in the $H-M$ space (H/s_{uTCA} , M/s_{uTCAD}).

To build a 3D failure envelope (V/V_0 , H/s_{uTCA} , M/s_{uTCAD}), the 2D failure envelope (H/s_{uTCA} , M/s_{uTCAD}) is first determined at four cross-sections of $V/V_0 = 0, 0.25, 0.5, \text{ and } 0.75$. In this study, the value of α is selected within the ranges from 0 to 180 degrees, serving as the loading constraint for the FELA. Note that the values of (V_0 , H , and M) are determined using the FELA model. In total, there are 960 ($4 \times 6 \times 4 \times 10$) analysis cases with ranges of (β , r_e , V/V_0 , α) to calculate (H/s_{uTCA} , M/s_{uTCAD}), as shown in Table. 6.2.

Table 6.2 Values of input parameters

Variable	Selected values
β	$90^0, 120^0, 150^0, 180^0$
r_e	0.5, 0.6, 0.7, 0.8, 0.9, 1
V/V_0	0, 0.25, 0.5, 0.75
α	$0^0, 15^0, 30^0, 60^0, 90^0, 100^0, 120^0, 140^0, 160^0, 180^0$

The normalized failure envelopes for conical foundations can be built based on the ultimate values V_0 , H_0 , and M_0 and presented as V/V_0 , H/H_0 , and M/M_0 ,

respectively (Gourvenec and Randolph, 2003; Gourvenec, 2008; Birid and Choudhury, 2022).

Using a similar approach to Bransby and Randolph (1998) and Yun and Bransby (2007), a limited set of simple mechanisms was employed. Figure 6.5 illustrates these mechanisms for a conical foundation. The optimal mechanisms for values of H slightly below or above the value corresponding to M lead to a backward (opposite to H) and forward translation of the foundation, along with rotation.

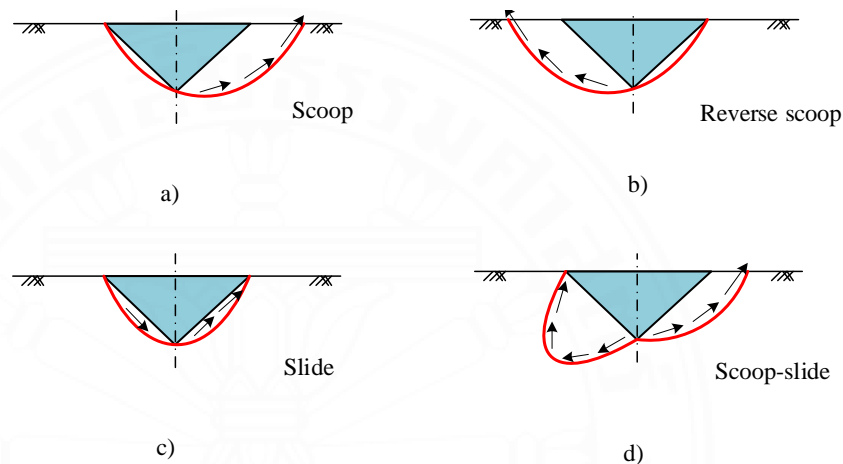


Figure 6.5 Examination of the failure mechanisms for H-M loading with (a) scoop, (b) reverse scoop, (c) slide, (d) scoop-slide

6.3.2 Boosting algorithm (CATBoost, XGBoost, GBM)

CATBoost is an innovative machine learning algorithm. It was first introduced by Dorogush et al. (2018) and further elucidated by Prokhorenkova et al. (2018) to address the challenge of dealing with categorical features, as noted by Hancock and Khoshgoftaar (2020). The tree expansion process maintains a level-wise growth pattern across all leaf nodes, as highlighted by Li et al. (2019). Moreover, CATBoost mitigates issues such as gradient bias and prediction shift, thereby reducing the likelihood of overfitting, as discussed by Hancock and Khoshgoftaar (2020) and Zhang et al. (2020). CATBoost employs a standard method of improving Greedy TS (Target-based Statistics) by incorporating prior distribution terms to enhance its performance (Prokhorenkova et al., 2018), as outlined in Eq. (6.3)

$$x_{\delta p,k} = \frac{\sum_{j=1}^{p-1} [x_{\delta j,k} = x_{\delta p,k}] \times Y_{\delta j} + \lambda P}{\sum_{j=1}^{p-1} [x_{\delta j,k} = x_{\delta p,k}] + \lambda} \quad (6.3)$$

where P represents an additional prior term, and λ typically denotes a positive weight coefficient. This initial term signifies the previous probability of positive instances in classification tasks. More details of the works can be found in Huang et al. (2019) and Kim et al. (2022).

Extreme Gradient Boosting (XGBoost) has become increasingly popular since the influential research works published by Chen and Guestrin (2016) and Kim et al. (2022). As a result, XGBoost was frequently used in successful machine learning competition solutions, particularly on platforms like Kaggle (Sheridan et al., 2016). The model function is defined by Fathipour-Azar (2021) in Eq. (6.4).

$$\hat{y}_T = \sum_{t=1}^T f_t(x_i) \quad (6.4)$$

where T indicates the total number of regression trees, $f_t(x_i)$ denotes the output from the t^{th} tree, and \hat{y}_t represents the predicted value generated by the XGBoost model.

Gradient Boosting Machine (GBM) is a widely employed supervised machine learning technique introduced by Friedman (2001). It is versatile and has a role to play in both regression and classification tasks across various disciplines, including geotechnical engineering (Zhou et al., 2016; Touzani et al., 2018; Qi et al., 2018; Chen et al., 2022; Schapire, 2003; Roe et al., 2005). Its fundamental principle involves iteratively enhancing predictions by blending numerous simple models termed weak learners (Natekin and Knoll, 2013). Each weak learner's contribution to the final prediction is determined through a gradient optimization process aimed at minimizing the overall error of the robust learner (Aurelien, 2018). Through continuous training, errors decrease progressively (Friedman, 2001). The architecture of the boosting algorithm is depicted in Fig. 6.6.

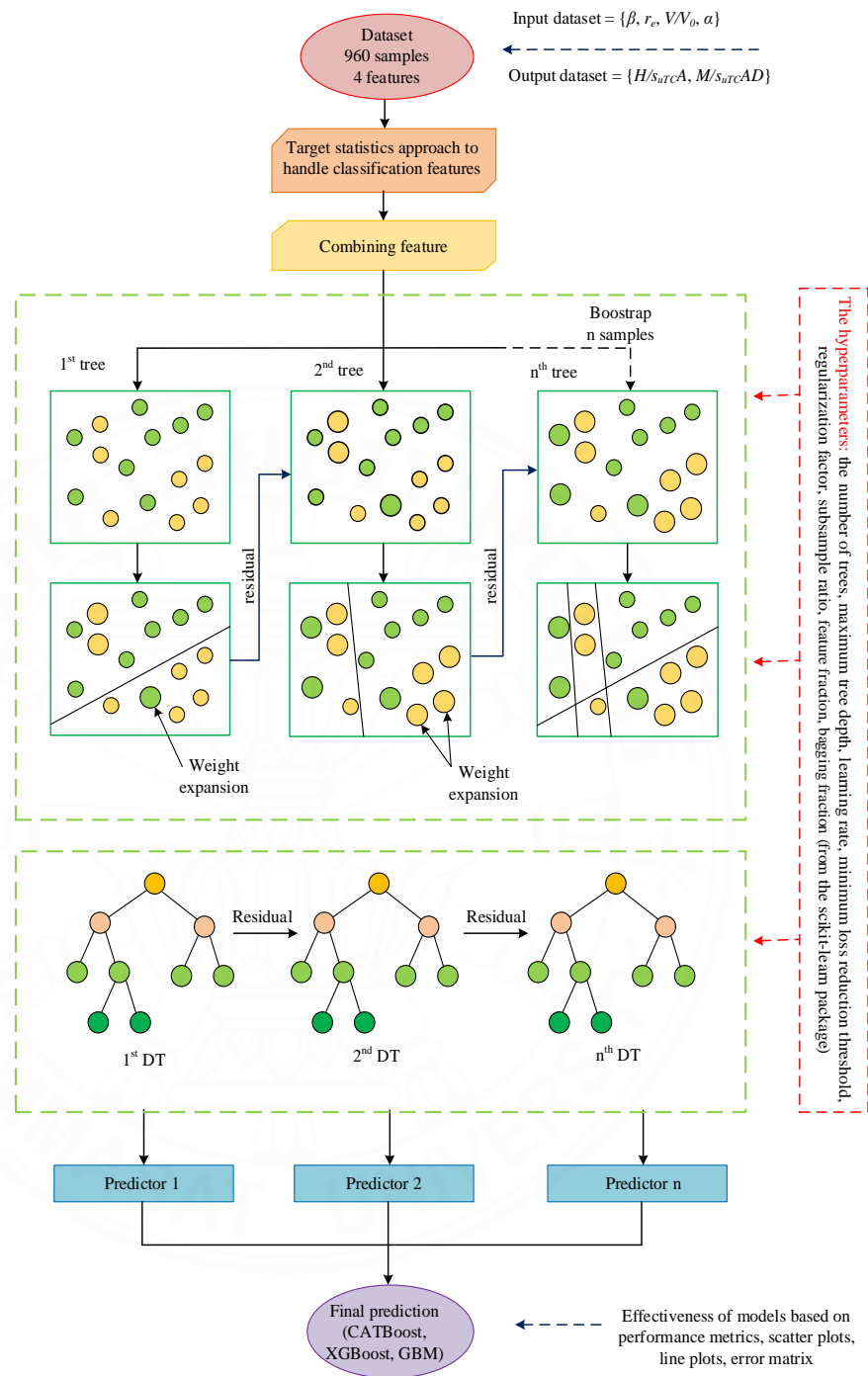
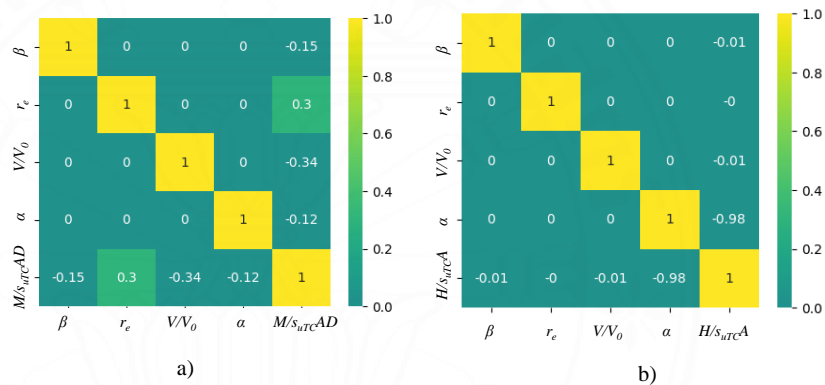


Figure 6.6 The architecture of the boosting models

The dataset for training the CATBoost, XGBoost, and GBM models was split into 70% for training (672 data points) and 30% for testing (288 data points). Table 6.3 details the statistical characteristics of each set, including the ranges, means, and standard deviations (SD). Furthermore, Fig. 6.7 displays the correlation heatmap matrix plotted for each input and output variable.

Table 6.3 Statistical properties of the training and testing datasets

Input parameters	Training set (70% data)				Testing set (30% data)			
	Min	Max	Mean	SD	Max	Min	Mean	SD
β	90	180	135.27	33.25	180	90	134.38	34.18
r_e	0.5	1.0	0.751	0.171	1.0	0.5	0.748	0.171
V/V_0	0	0.75	0.368	0.28	0.75	0	0.38	0.277
α	0	180	87.22	59.48	180	0	94.81	57.25
Output parameters	Training set (70% data)				Testing set (30% data)			
	Min	Max	Mean	SD	Min	Max	Mean	SD
H/s_{uTCA}	-3.353	3.178	0.106	0.902	-2.632	3.353	0.009	0.848
M/s_{uTCAAD}	0	0.649	0.313	0.191	0	0.65	0.321	0.182

Figure 6.7 Correlation heatmap for (a) M/s_{uTCAAD} , (b) H/s_{uTCA}

The effectiveness of CATBoost, XGBoost, and GBM machine learning methods in predicting the V-H-M failure envelope is assessed using six performance metrics. These metrics include the coefficient of determination (R^2), weighted mean absolute percentage error (WMAPE), root mean square error (RMSE), variance account factor (VAF), Willmott's index of agreement (WI), and maximum absolute error (MAE) (Willmott, 1984; Jiang et al., 2021; Zhou et al., 2020). To ascertain the model that provides the most reliable predictions and best fits the particular issue, rank analysis is utilized in this study (Pradeep et al., 2021).

The error matrix, like a confusion matrix or heatmap, adeptly condenses the evaluation of a machine learning model's efficacy. Scatter plots and line plots are versatile tools to illustrate connections between observed and forecasted values (Kumar et al., 2024). A Taylor diagram, alternatively called a Taylor plot, is a visual tool designed to compare several models against a reference dataset (Taylor,

2001). By showcasing multiple performance measures concurrently, the Taylor diagram streamlines the evaluation of model precision.

6.4 Results and comparison

6.4.1 Verification

To verify the numerical results produced in this study, Figure 6.8 compares the vertical bearing capacity factor (V/s_{uTCA}) assessment for various conical foundations on anisotropic clays. In Fig. 6.8a, our results are compared with those of Keawsawasvong (2022) for cases with ($r_e = 0.5$ to 0.9 and $\beta = 90$ to 180 degrees). The comparison shows a close alignment between present results and Keawsawasvong (2022) across all scenarios, with differences ranging from 4 to 6%. Similarly, in Fig. 6.8b, numerical results of ($\beta = 90$ to 180 degrees, $r_e = 1$) are compared with those of Houlsby and Martin (2003) using the method of characteristics as well as Keawsawasvong (2022) using the axisymmetric FELA method. The excellent agreement can be attributed to the use of the Tresca failure criterion for isotropic clays with $r_e = 1$. Overall, our results closely match those published ones, giving confidence for the parametric studies in anisotropic clay.

Comparisons are further made in relation to the normalized failure envelopes under $V-H$, $V-M$, and $H-M$ load combinations. These are shown in Figs. 6.9a to 6.9c where our results are compared with those in Gourvenec and Randolph (2003), Taiebat and Carter (2000), and Taiebat and Carter (2010) for conical footings on isotropic clay ($\beta = 180^\circ$, $r_e = 1$). Despite that different failure criteria were employed in each method, our results closely align with those of Gourvenec and Randolph (2003), Taiebat and Carter (2000), and Taiebat and Carter (2010).

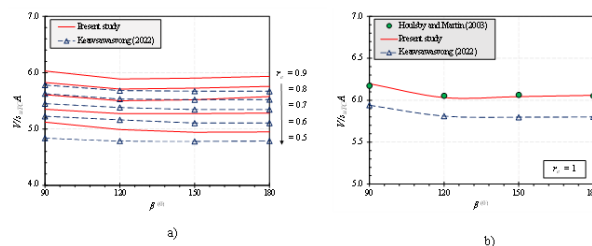


Figure 6.8 Comparison of results with those by Keawsawasvong (2022) and Houlsby and Martin (2003): (a) anisotropic clay and (b) isotropic clay

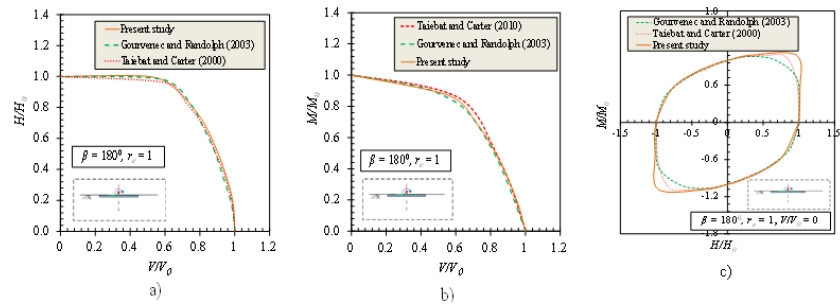


Figure 6.9 Comparison of results with published solutions: (a) V-H loadings, (b) V-M loading, (c) H-M loading

6.4.2 FELA results

Fig. 6.10 presents the variations in failure envelopes for conical foundations on anisotropic clay surfaces subjected to *V-H* loading. Numerical results are for varying cone apex angle ($\beta = 180, 150, 120,$ and 90 degrees) and anisotropic ratio ($r_e = 0.5$ to 1). Four observations can be made from inspecting the figure: (1) for a pure vertical loading (i.e., $H/s_{uTCA} = 0$), the greater the value of r_e , the larger the vertical limit load factor V/s_{uTCA} ; (2) for a pure horizontal loading (i.e., $V/s_{uTCA} = 0$), the horizontal limit load H/s_{uTCA} increases with the higher value of r_e ; (3) the smaller the apex angle β , the larger the area of failure envelope; (4) the larger the value of r_e , the greater the area of failure envelope.

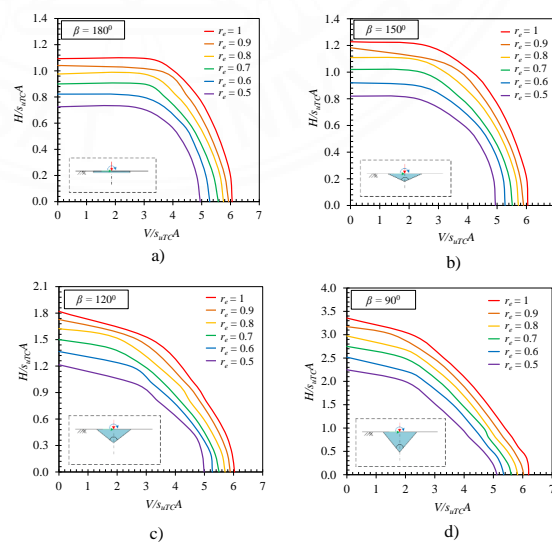


Figure 6.10 The failure envelope of conical footing under V-H loadings: (a) $\beta = 180^0$, (b) $\beta = 150^0$, (c) $\beta = 120^0$, (d) $\beta = 90^0$

Fig. 6.12 presents the various failure envelopes under V - M loading combinations for cone apex angle $\beta = (180, 150, 120, \text{ and } 90 \text{ degrees})$ and anisotropic ratios $r_e = (0.5 \text{ to } 1)$. Three observations are made based on the numerical results: (1) for a pure moment action (i.e., $V/s_{uTC A} = 0$), the greater the value of r_e , the larger the moment limit factor $M/s_{uTC AD}$; (2) for a pure vertical loading (i.e., $M/s_{uTC AD} = 0$), the greater the value of r_e , the larger the vertical limit load $V/s_{uTC A}$; (3) the larger the value of r_e , the greater the area of failure envelope.

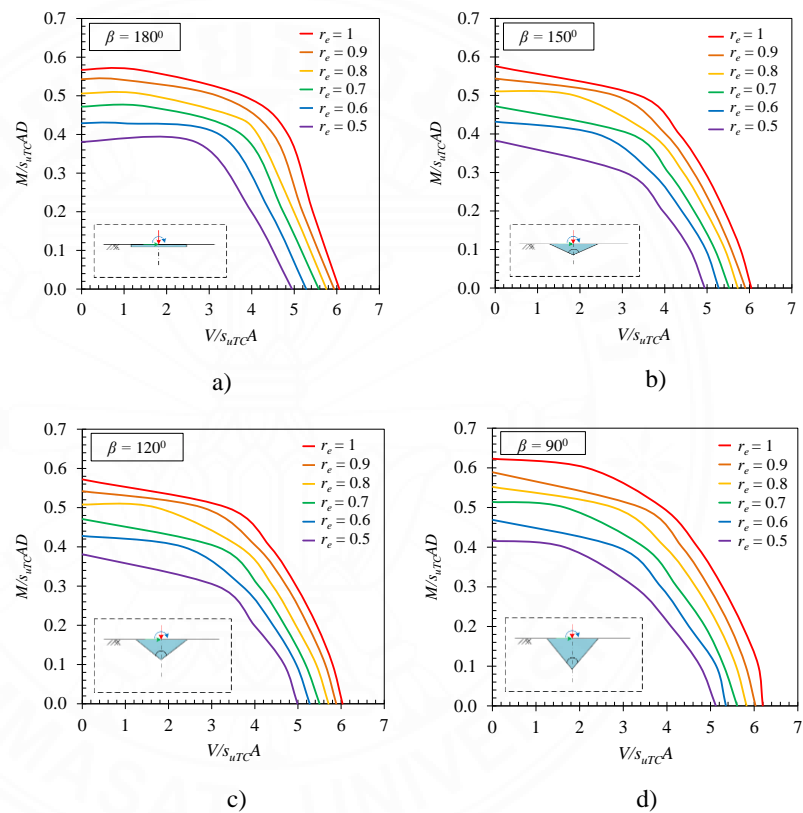


Figure 6.11 The conical footing failure envelope under V - M loadings: (a) $\beta = 180^0$, (b) $\beta = 150^0$, (c) $\beta = 120^0$, (d) $\beta = 90^0$

Fig. 6.12 presents the variations in failure envelopes under H - M loading combinations at the level vertical load of $V/V_0 = 0.25$. The horizontal capacity $H/s_{uTC A}$ decreases with increasing β . Also, note that the moment capacity $M/s_{uTC AD}$ and horizontal capacity $H/s_{uTC A}$ increase with increasing r_e for all conical geometries. The resulting contours for conical foundations with the cone apex angle $\beta = 150$ degrees and $r_e = 0.6, 0.8, 0.9, \text{ and } 1$ are presented in Figure 6.13 for practical design uses. It is

also noticeable that the shape and size of the envelopes for conical foundations depend on V/V_0 .

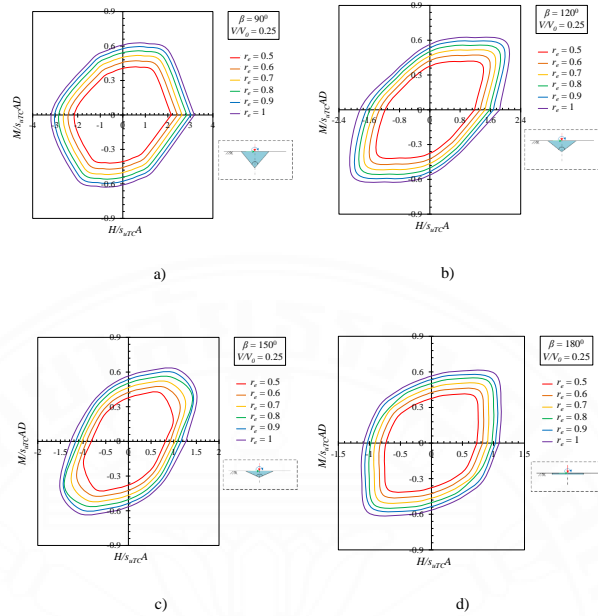


Figure 6.12 The failure envelope of conical footing under H-M loadings at $V/V_0 = 0.25$ with (a) $\beta = 90^\circ$, (b) $\beta = 120^\circ$, (c) $\beta = 150^\circ$, (d) $\beta = 180^\circ$

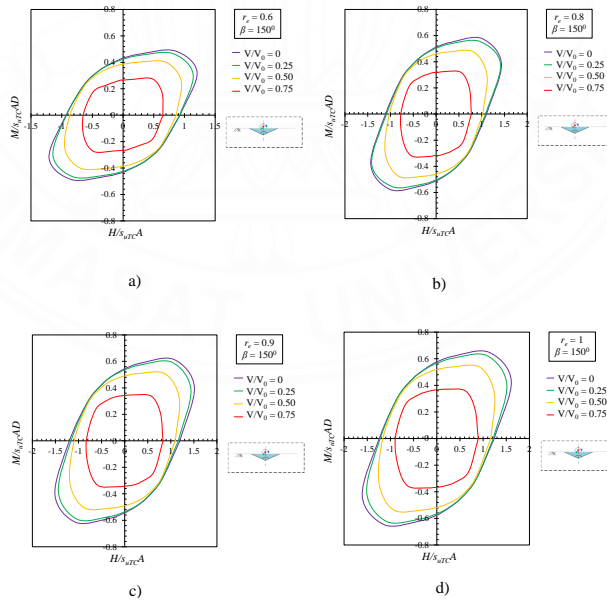


Figure 6.13 Two dimensions illustrating the collective failure loads for a conical foundation with $\beta = 150^\circ$ and (a) $r_e = 0.6$, (b) $r_e = 0.8$, (c) $r_e = 0.9$, (d) $r_e = 1$

Further, by integrating these failure surfaces with the reflecting negative bending moments and horizontal loads, a comprehensive representation of

failure surfaces within the V - H - M space is shown in Fig. 6.14 and 6.15. Figure 6.14(a-d) illustrates the 3D failure envelope (V/V_0 , $H/s_{uTC A}$, $M/s_{uTC AD}$) in the cases of $\beta = 120^\circ$ and $r_e = 0.5, 0.7, 0.8$, and 1 , respectively. The size of the 3D failure envelope becomes more significant when the value of r_e increases. The 3D failure surfaces for the cases $r_e = 0.6$ and $\beta = 90, 120, 150$, and 180 degrees are illustrated in Fig. 6.15. The shape and size of the 3D failure envelope becomes smaller when the value of β increases.

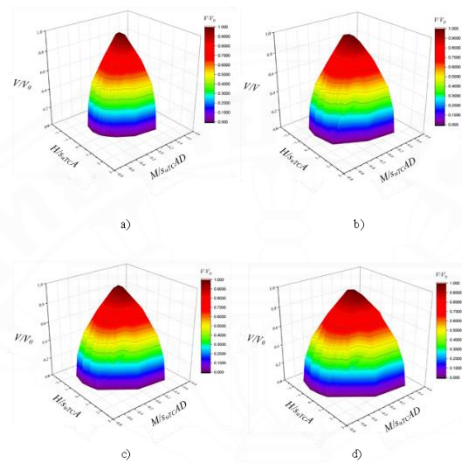


Figure 6.14 A three-dimensional graphical depiction illustrating the combining failure loads for a conical footing with $\beta = 120^\circ$, and (a) $r_e = 0.5$, (b) $r_e = 0.7$, (c) $r_e = 0.8$, (a) $r_e = 1$

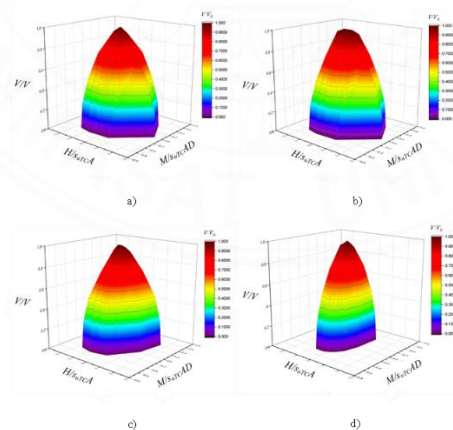


Figure 6.15 A three-dimensional graphical depiction illustrating the combining failure loads for a conical footing with $r_e = 0.6$, and (a) $\beta = 90^\circ$, (b) $\beta = 120^\circ$, (a) $\beta = 150^\circ$, $\beta = 180^\circ$

Using shear power dissipation, Fig. 6.16 demonstrates a series of possible failure mechanisms under various combinations of V , H , and M loads, both

positive and negative, for cases where $r_e = 0.7$, $\beta = 180^\circ$, and $V/V_0 = 0.75$. Six cases are investigated, corresponding to different values of α angles, including $\alpha = 0^\circ$, 15° , 30° , 90° , 140° , and 160° . At $\alpha = 0^\circ$, a pure horizontal mechanism is developed with the rigid translation of soil occurring in the bottom of the conical foundation, and H_0 is mobilized in this case. A pure bending moment failure is observed at $\alpha = 90^\circ$, where the ultimate moment M_0 is mobilized.

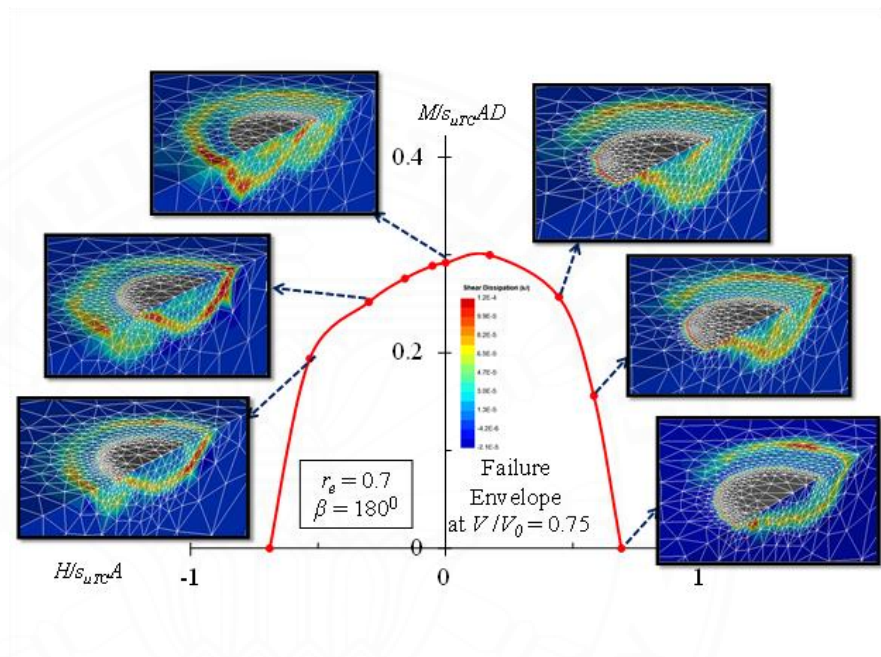


Figure 6.16 Failure mechanism of a 2D failure envelope of a conical foundation under general loading for $r_e = 0.7$, $\beta = 180^\circ$, and $V/V_0 = 0.75$

Figure 6.17(a-c) illustrates the comparison of failure mechanisms under different combinations of horizontal loads and bending moments, specifically for conditions where $r_e = 0.9$, $V/V_0 = 0.5$, and $\beta = 90, 120$, and 150 degrees, respectively. At $\alpha = 0^\circ$, a pure sliding mechanism occurs, where soil rigidly translates at the base of the footing due to interface conditions, and H_0 is activated. As α reaches 90 degrees, the plastic zone expands, resulting in a scoop-slide mechanism (see Fig. 6.7d). When α approaches 180 degrees, the shear plane transforms from scoop-slide to reverse scoop mechanism at the back and bottom of the foundation for all cases of $\beta = 90, 120$, and 150 degrees (refer to Fig. 6.7b and 6.7d).

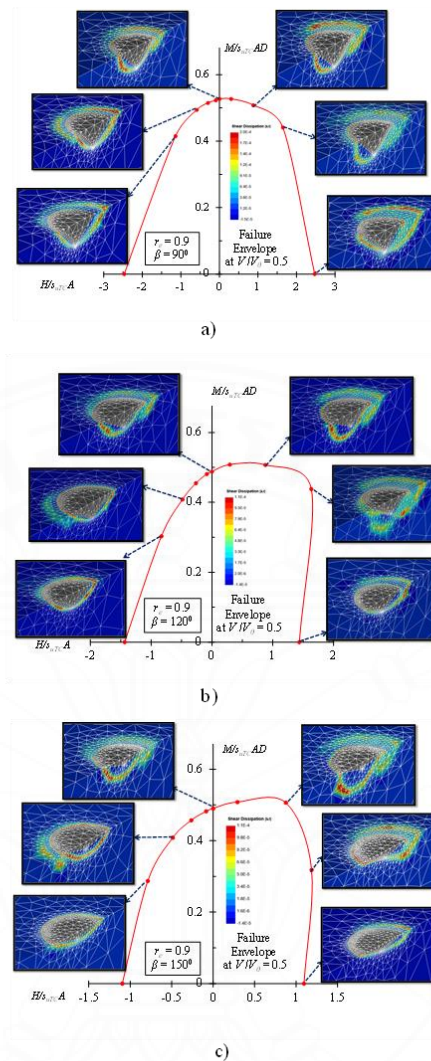


Figure 6.17 Failure mechanism of a 2D failure envelope of the conical footing under general loading for $r_e = 0.9$, $V/V_0 = 0.5$, with (a) $\beta = 90^\circ$, (b) $\beta = 120^\circ$, (c) $\beta = 150^\circ$

6.4.3 Machine learning results

In this section machine learning results are discussed in detail. With a total of 960 datasets containing x and their corresponding y values for the probability of the failure envelope (H/s_{uTCA} , $M/s_{uTCA}D$). A series of regression plots comparing the results of 3D FELA with those of CATBoost, XGBoost, and GBM models are presented in Fig. 6.18 for both the training and testing phases. The closeness of predicted values for CATBoost to the equality line is noticeable, with a remarkable R^2 value of 0.99996 for the training set, indicating superior performance and reliability over other models.

Line plots for the CATBoost, XGBoost, and GBM models are presented in Figs. 6.19(a-c). These plots demonstrate similar data fitting among the models, suggesting their performance probabilities are evenly matched. Furthermore, Fig. 6.20 presents Taylor diagrams for the training and testing stages in the cases of H/s_{uTCA} and M/s_{uTCA} . The CATBoost, XGBoost, and GBM models demonstrate strong performance in both phases, positioning them closer to the reference point. This superiority is evident in Fig. 6.20a, where the dots representing CATBoost, XGBoost, and GBM coincide, indicating their comparable performance; however, CATBoost shows a slight edge in both the training and testing phases.

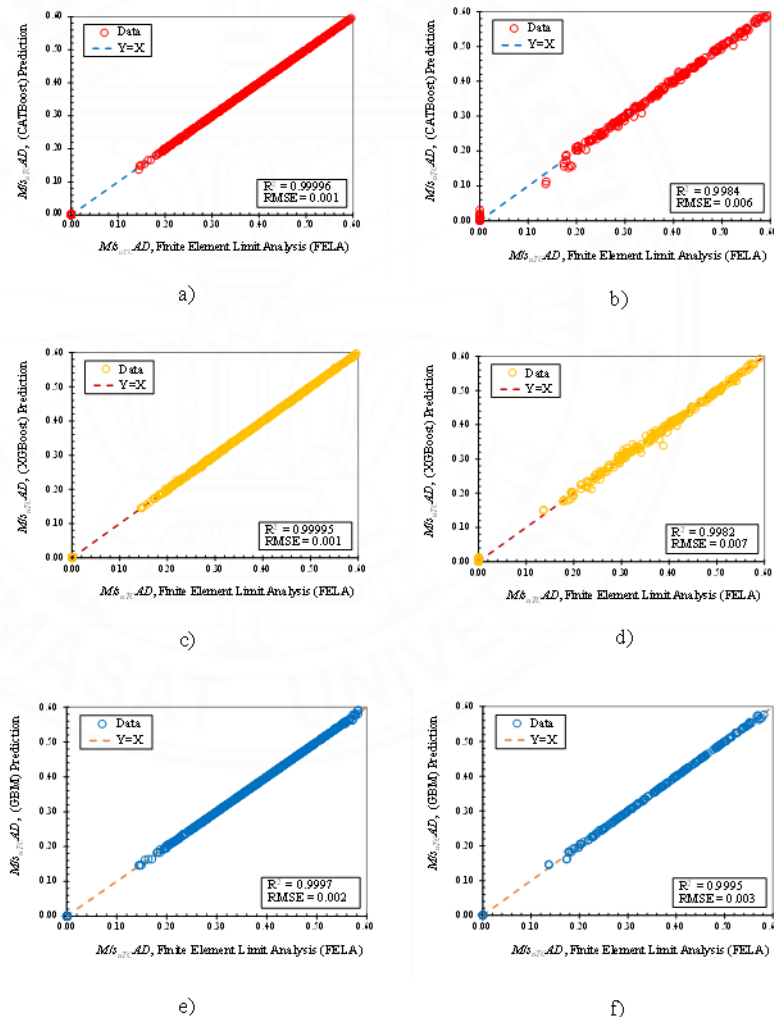


Figure 6.18 Comparison of the FELA with those from: a) CATBoost training, b) CATBoost testing, c) XGBoost training, d) XGBoost testing, e) GBM training, and f) GBM testing

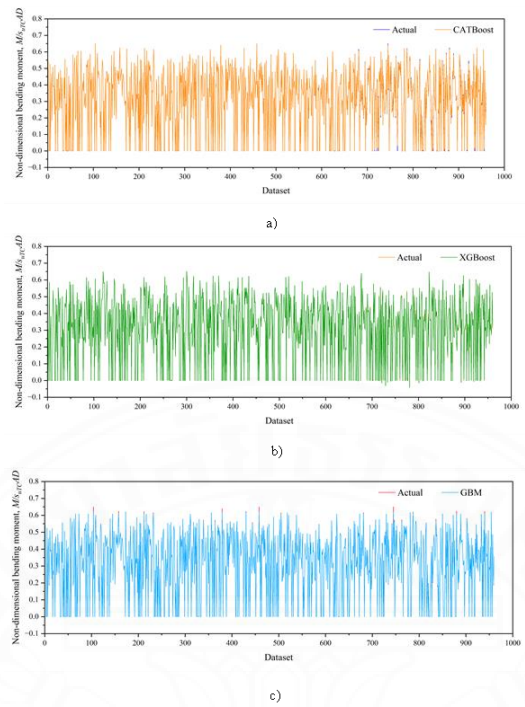


Figure 6.19 Performance of machine learning model utilizing line plot for a) CATBoost, b) XGBoost, and c) GBM

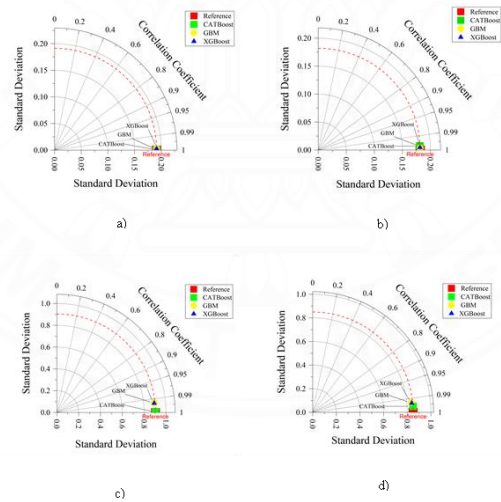


Figure 6.20 Taylor chart for a) M/s_{uTCAD} training, b) M/s_{uTCAD} testing, c) H/s_{uTCA} training, d) H/s_{uTCA} testing

6.5 Conclusion

It was found that the failure envelopes of conical foundations exhibit symmetry under vertical-horizontal ($V-H$) and vertical-moment ($V-M$) planes.

Generally, a bigger failure envelope often results from an increase in either the anisotropic ratio (r_e) or the cone apex angle (β). As r_e changes from 0.5 to 1, the size of the $H/s_{uTC}A$ - $M/s_{uTC}AD$ space in the 3D failure envelopes dramatically rises for various levels of vertical loadings ($V/V_0 = 0, 0.25, 0.5, 0.75$).

CATBoost is the most efficient method in predicting the 3D failure envelope of conical foundations on anisotropic clay under combined loadings (V - H - M), achieving high accuracy with $R^2 = 99.99\%$.



CHAPTER 7

CONCLUSION

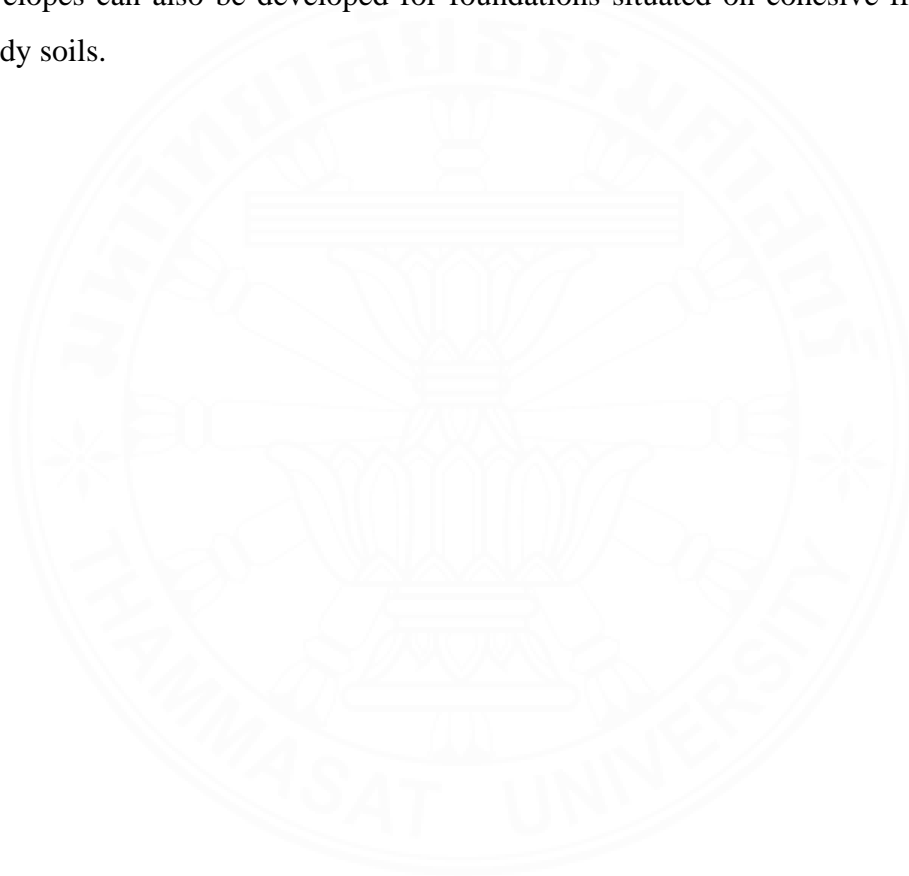
7.1 Summary

Failure envelopes of strip, ring and conical foundations in anisotropic clay under general loadings ($V-H-M$) have been effectively studied in this thesis using advanced finite element limit analysis (FELA) as well as the machine learning methods of ANN, ANN-ICA, ANN-ALO, ANN-ABC, CATBoost, XGBoost and GBM. The normalized factors of ($V-H-M$) for foundations were determined by considering two dimensionless input parameters; namely the shape factor (e.g., r_i/r_o , β) and the anisotropic factor (r_e). Extensive comparisons were made between the present solutions and those published previously. It was found that the failure envelopes of foundations exhibit symmetry under vertical-horizontal ($V-H$) and vertical-moment ($V-M$) planes. However, asymmetry was observed in the failure zones under ($H-M$) planes across all shapes and anisotropic ratios. Generally, a bigger failure envelope often results from an increase in either the anisotropic ratio (r_e) or the shape ratio. As r_e changes from 0.5 to 1, the size of the $H-M$ space in the 3D failure envelopes dramatically rises for various levels of vertical loadings (V/V_0).

In regards to the machine learning model applications, machine learning models were used to build realistic engineering tools for the construction of failure envelopes in both two dimensions ($H-M$) and three dimensions (V , H , and M). Comparisons among the boosting models have demonstrated that machine learning is the most efficient method in predicting the 3D failure envelope of foundations on anisotropic clay under combined loadings ($V-H-M$), achieving high accuracy. It is important to emphasize that this thesis focuses on the failure envelope capacity of foundations due to the absence of design equations predicting the failure envelope of footings using machine learning methods.

7.2 Suggestion

This thesis demonstrates promising results in terms of predictive accuracy and computational efficiency across various practical scenarios. It further enables the establishment of a failure envelope for footings under combined loading conditions, which can be valuable for practitioners in the field. The present study underscores the novelty and importance of its significance in foundation designs. In the future, failure envelopes can also be developed for foundations situated on cohesive-frictional and sandy soils.



REFERENCES

1. Abdi, R., de Buhan, P., and Pastor, J. (1994). Calculation of the critical height of homogenized reinforced soil wall: a numerical approach. *Int. J. Numer. Anal. Methods Geomech.*, 18:485-505.
2. Abdollahi F, Hosseini S, Sabet M, Esmaeili-Faraj SM, Amiri F (2021) A novel study of the gas lift process using an integrated production/injection system using artificial neural network approach. *Modeling Earth Systems and Environment*, 7, 2101-2112
3. Ahmad F, Hussain A, Ansari MA (2022) Development of ANN model for the prediction of discharge coefficient of an arced labyrinth side weir. *Modeling Earth Systems and Environment*, 9, 1835-1842
4. Ahmad, M., Ahmad, F., Wróblewski, P., Al-Mansob, R.A., Olczak, P., Kamiński, P., Safdar, M., Rai, P., 2021. Prediction of Ultimate Bearing Capacity of Shallow Foundations on Cohesionless Soils: A Gaussian Process Regression Approach. *Appl. Sci.* 11, 10317.
5. Ali, A., Lyamin, A. V., Huang, J., Li, J.H., Cassidy, M.J., Sloan, S.W., 2017. Probabilistic Stability Assessment Using Adaptive Limit Analysis and Random Fields. *Acta Geotech.* 12, 937–948.
6. Andersen, K. H. 2009. Bearing capacity under cyclic loading - offshore, along the coast and on land. *Canadian Geotechnical Journal*, 46, 513-535.
7. Andersen, K. H., Murff, J. D., Randolph, M., Clukey, E. C., Erbrich, C. T., Jostad, H., Hansen, B., Aubeny, C. P., Sharma, P., and Supachawarote, C. (2005). Suction anchors for deepwater applications. In Cassidy, M. J. and Gourvenec, S. M., editors, *Front. Offshore Geotech.*, volume 1, pages 1-30. Taylor & Francis, Perth, Australia.
8. Arama, A.Z., Yucel. M., Akin. M. S., Dalyan. I. (2021). A comparative study on the application of artificial intelligence networks versus regression analysis for the prediction of clay plasticity. *ArabianJournal of Geosciences*, 14-534.
9. Armaghani, D.J., Momeni, E., Abad, S.V.A.N.K., Khandelwal, M., 2015. Feasibility of ANFIS model for prediction of ground vibrations resulting from quarry blasting. *Environ. Earth. Sci.* 74, 2845–2860.

10. Atashpaz-Gargari, E., Lucas, C., 2007. Imperialist competitive algorithm: an algorithm for optimization inspired by imperialistic competition. In: 2007 IEEE Congress on Evolutionary Computation, CEC 2007. 4661–4667.
11. Aurélien, G., 2018. Hands-On Machine Learning with Scikit-Learn, Keras, and TensorFlow: Concepts, Tools, and Techniques to Build Intelligent Systems, Hanvit Media: Seoul, Korea.
12. Basheer IA, Hajmeer M (2000) Artificial neural networks: fundamentals, computing, design, and application. *J Microbiol Methods* 43(1):3-31.
13. Beale MH, Hagan MT, Demuth HB (2010) Neural network toolbox 7. User's Guide, MathWorks, 2
14. Belytschko, T. and Hodge, P. (1970). Plane stress limit analysis by finite elements. *J. Eng. Mech. Div.*, 96:931-944.
15. Benmebarek, S., Remadna, M.S., Benmebarek, N., Belouar, L., 2012. Numerical evaluation of the bearing capacity factor N_γ of ring footings. *Comput. Geotech.* 44 (6), 132–138.
16. Bharti, J.P., Mishra, P., Moorthy, U., Sathishkumar, V.E., Cho, Y., Samui, P., 2021. Slope stability analysis using RF, GBM, CART, BT and XGBoost. *Geotech Geol Eng* 39:3741–3752
17. Birid, K., Choudhury, D., 2021. Undrained bearing capacity factor N_C for ring foundations in cohesive soil. *Int. J. Geomech.* 21 (2), 06020038.
18. Birid, K., Choudhury, D., 2022. Failure envelopes for ring foundations resting on Tresca soil under combined loading. *Journal of Geotechnical and Geoenvironmental Engineering.* 148 (11), 04022088.
19. Bolton MD, Lau CK (1993) Vertical Bearing Capacity Factors for Circular and Strip Footings on Mohr-Coulomb Soil. *Canadian Geotechnical Journal*, 30, 1024-1033
20. Bottero, A., Negre, R., Pastor, J., and Turgeman, S. (1980). Finite element method and limit analysis theory for soil mechanics problems. *Comput. Methods Appl. Mech. Eng.*, 22:131–149.
21. Boushehrian, J.H., Hataf, N., 2003. Experimental and numerical investigation of the bearing capacity of model circular and ring footings on reinforced sand. *Geotextiles and Geomembranes.* 21, 241–256.

22. Bransby, M.F., Randolph, M.F., 1998. Combined loading of skirted foundations. *Geotechnique*. 48 (5), 637–655.
23. Bransby, M.F., Yun, G.J., 2009. The undrained capacity of skirted strip foundations under combined loading. *Geotechnique*. 59 (2), 115–125.
24. Breiman, L., 2017. *Classification and regression trees*. Routledge.
25. Brinch Hansen J (1970) A revised and extended formula for bearing capacity. *Dan. Geotech. Inst. Bull*, 28, 5–11
26. Brinch Hansen, J., 1970. A revised and extended formula for bearing capacity. *Danish Geotechnical Institute Bulletin*. 28, 5–11.
27. Butterfield R (1999) Dimensional analysis for geotechnical engineering. *Géotechnique*, 49(2), 357–366
28. Butterfield R, Gottardi G (1994) A complete three-dimensional failure envelope for shallow footings on sand (technical note). *Géotechnique*, 44(1), 181-184
29. Butterfield R, Ticof J (1979) Design parameters for granular soils (discussion contribution). *Proc. 7th European Conf. on Soil Mech. and Foundation Eng*, Brighton, 4, 259-261
30. Butterfield, R. (1981). Another look at gravity platform foundations, CISM course on Soil Mech. Fndn. Engng. in Offshore Technology, Udine.
31. Butterfield, R. (1993). A new approach to safety factors for shallow foundations: load combination factors as a basis for risk assessment, ICE Conf. on risk and reliability in ground engineering, Thomas Telford, London, pp. 112-125.
32. Butterfield, R., Houlsby, G. T. & Gottardi, G. (1997). Standardised sign conventions and notation for generally loaded foundations. *Géotechnique* 47(5), 1051-1054.
33. Byrne, B. W. 2000. *Investigations of suction caissons in dense sand*. University of Oxford.
34. Byrne, B., Houlsby, G., 2003. Foundations for offshore wind turbines. *Philos Trans R Soc Lond Ser A Math Phys Eng Sci* 361 (1813), 2909–2930
35. Casagrande, A., Carillo, N., 1944. Shear failure of anisotropic soils. *Contributions to Soil Mechanics (BSCE)*. 1941–1953, 122–135.
36. Cassidy, M., Houlsby, G., 2002. Vertical bearing capacity factors for conical foundations on sand. *Geotechnique* 52 (9), 687–692.

37. Chakraborty, D., Kumar, J., 2016. The size effect of a conical footing on N_{γ} . *Comput Geotech.* 76, 212–221.
38. Chakraborty, M. and Kumar, J. (2015). Lower-bound axisymmetric formulation for geomechanics problems using nonlinear optimization. 06014024(8):1-8.
39. Chakraborty, M., Kumar, J., 2015. Bearing capacity factors for a conical footing using lower- and upper-bound finite elements limit analysis. *Can Geotech J.* 52, 2134–2140.
40. Chanda, D., Nath, U., Saha, R., Haldar, S., 2021. Development of Lateral Capacity Based Envelopes of Piled Raft Foundation Under Combined V-M-H Loading. *International Journal of Geomechanics.* 21 (6), 0402175.
41. Chen, H., Shen, Z., Wang, L., Qi, C., Tian, Y., 2022. Prediction of undrained failure envelopes of skirted circular foundations using gradient boosting machine algorithm. *Ocean Engineering.* 258 (6), 111767.
42. Chen, L., Li, J., Li, Q., Feng, Y., 2021. Strengthening mechanism of studs for embedded-ring foundation of wind turbine tower. *Energies.* 14 (3), 710.
43. Chen, L., Liu, G., 2018. Upper bound solutions of vertical bearing capacity of skirted mudmat in sand. *Applied Ocean Research.* 73 (5), 100-106.
44. Chen, T., Guestrin, C., 2016. Xgboost: A scalable tree boosting system. In *Proceedings of the 22nd acm sigkdd international conference on knowledge discovery and data mining.* 785-794.
45. Chen, Z., Wang, J., Wang, Y., Yin, J.-H., and Haberfield, C. (2001). A three-dimensional slope stability analysis method using the upper bound theorem Part II: numerical approaches, applications and extensions. *Int. J. Rock Mech. Min. Sci.*, 38(3):379–397.
46. Cherif K, Yahia N, Bilal B (2023) Erosion potential model-based ANN-MLP for the spatiotemporal modeling of soil erosion in wadi Saida watershed. *Model. Earth Syst. Environ.* 9, 3095–3117.
47. Ciria, H., Peraire, J., Bonet, J., 2008. Mesh adaptive computation of upper and lower bounds in limit analysis. *Int. J. Numer. Methods Eng.* 75, 899–944.
48. Cox, A. D., Eason, G. & Hopkins, H. G. (1961). Axially symmetric plastic deformations in soils. *Phil. Trans. Royal Soc. London, Series A*, 25, 1-45.

49. Craig, W.H., Chua, K., 1990. Deep penetration of spudcan foundations on sand and clay. *Géotechnique*. 40 (4), 541–556.
50. Das BM, Larbi-Cherif S (1983) Bearing capacity of two closely-spaced shallow foundations on sand. *Soil and Foundation*, 1-7
51. Davis EH, Christian JT (1971) Bearing capacity of anisotropic cohesive soil. *Journal of Soil Mechanics and Foundation Division*, 97(5), 753–769
52. Davis, E. H. & Booker, J. R. 1973. The effect of increasing strength with depth on the bearing capacity of clays. *Geotechnique*, 23, 551-563.
53. Dean, E. T. R., James, R. G., Schofield, A. S., Tan, F. S. C. & Tsukamoto, Y. (1992). The bearing capacity of conical footings on sand in relation to the behaviour of spudcan footings of jack-ups. *Predictive Soil Mechanics (Proc. Wroth Memorial Sym., Oxford)*, 230-253. London: Thomas Telford.
54. Dessi, D., Sanchez-Alayo, D., Shabani, B., Ali-Lavroff, J., 2023. Bow slamming detection and classification by Machine Learning approach. *Ocean Engineering*. 287, 115646.
55. DNV 1992. Classification notes No.30.4. Foundations. Det Norske Veritas.
56. Dong, X., Guo, M., Wang, S., 2023. Inclination prediction of a giant open caisson during the sinking process using various machine learning algorithms. *Ocean Engineering*. 269, 113587.
57. Dongare AD, Kharde RR, Kachare AD (2012) Introduction to artificial neural network. *Int J Eng Innov Technol (IJEIT)* 2(1):189–194.
58. Dorogush, A.V., Ershov, V., Gulin, A., 2018. CatBoost: Gradient boosting with categorical features support. *arXiv:1810.11363*
59. Drucker, D., Prager, W., and Greenburg, H. (1952). Extended limit design theory for continuous media. *Q. Appl. Math.*, 9:381-389.
60. Du, Y., Qian, S., Fu, X., Chen, H., Li, G., 2022. New model for predicting the bearing capacity of large strip foundations on soil under combined loading. *Int. J. Geomech.* 22 (5), 04022055.
61. Du, Y., Qian, S., Fu, X., Chen, H., Li, G., 2022. New model for predicting the bearing capacity of large strip foundations on soil under combined loading. *Int. J. Geomech.* 22 (5), 04022055

62. Dunne, H.P., Martin, C.M., 2017. Capacity of rectangular mudmat foundations on clay under combined loading. *Geotechnique*. 67 (2), 168–180
63. El Sawwaf, M., Nazir, A., 2012. Behavior of eccentrically loaded small-scale ring footings resting on reinforced layered soil. *J. Geotech. Geoenviron. Eng.* 138 (3), 376–384.
64. Ellers, F. S. (1982). Advanced offshore oil platforms, *Scientific American* 246(4): 31-41.
65. Fan, Y., Wang, J., Feng, S., 2021. Effect of spudcan penetration on laterally loaded pile groups. *Ocean Eng.* 221, 108505.
66. Fathipour Azar, H., 2021. Data driven estimation of joint roughness coefficient. *J. Rock Mech. Geotech. Eng.* 13, 1428–1437.
67. Feng X, Randolph MF, Gourvenec S, Wallerand R (2014) Design approach for rectangular mudmats under fully three-dimensional loading. *Geotechnique*, 64(1), 51–63
68. Fiumana, N., Bienen, B., Govoni, L., Gourvenec, S., Cassidy, M.J., Gottardi, G., 2019. Combined loading capacity of skirted circular foundations in loose sand. *Ocean Eng.* 183, 57–72.
69. Friedman, J., 2001. Greedy function approximation: a gradient boosting machine. *Ann. Stat.* 29 (5), 1189–1232.
70. Gaudin, C., Cassidy, M.J., Bienen, B., Hossain, M.S., 2011. Recent contributions of geotechnical centrifuge modelling to the understanding of jack-up spudcan behaviour. *Ocean Eng.* 38 (7), 900–914
71. Gholami, V., Sahour, H., 2022. Simulation of rainfall-runoff process using an artificial neural network (ANN) and field plots data. *Theor. Appl. Climatol.* 147, 1–12.
72. Gottardi G, Butterfield R (1993) On the bearing capacity of surface footings on sand under general planar load. *Soils Found*, 33(3), 68–79
73. Gottardi, G. & Houlsby, G. T. (1995). Model Tests of Circular Footings on Sand Subjected to Combined Loading. Report no. OUEL 2071/95, Oxford University Engineering Laboratory.
74. Gottardi, G., Houlsby, G. T. & Butterfield, R. (1997). The plastic response of circular footings on sand under general planar loading. Report no. QUEL 2143/97, Oxford University Engineering Laboratory.

75. Gottardi, G., Houlsby, G. T. & Butterfield, R. 1999. Plastic response of circular footings on sand under general planar loading. *Geotechnique*, 49, 453-469.
76. Gourvenec S (2007) Failure envelopes for offshore shallow foundations under general loading. *Geotechnique*, 57, 715-728
77. Gourvenec S (2008) Effect of embedment on the undrained capacity of shallow foundations under general loading. *Geotechnique*, 58(3), 177–185
78. Gourvenec, S. & Steinpreis, M. 2007. Undrained limit states of shallow foundations acting in consort. *International Journal of Geomechanics*, 7, 194-205.
79. Gourvenec, S. 2007a. Failure envelopes for offshore shallow foundations under general loading. *Geotechnique*, 57, 715-728.
80. Gourvenec, S. 2007b. Shape effects on the capacity of rectangular footings under general loading. *Geotechnique*, 57, 637-646.
81. Gourvenec, S. M. & Mana, D. S. K. 2011. Undrained vertical bearing capacity factors for shallow foundations. *Geotechnique Letters*, 1, 101 - 108.
82. Gourvenec, S., Barnett, S., 2011. Undrained failure envelope for skirted foundations under general loading. *Géotechnique* 61 (3), 263–270.
83. Gourvenec, S., Randolph, M. & Kingsnorth, O. 2006. Undrained bearing capacity of square and rectangular footings. *International Journal of Geomechanics*, 6, 147-157.
84. Gourvenec, S.M., Randolph, M.R., 2003. Effect of strength non-homogeneity on the shape and failure envelopes for combined loading of strip and circular foundations on clay. *Géotechnique* 53(6), 575–586.
85. Goutham D.R., Krishnaiah., A.J. (2021). Application of artificial neural networking technique to predict the geotechnical aspects of expansive soil: a review. *International Journal Engineering and Manufacturing*, 6, 48-53.
86. Green, A. P. 1954. The plastic yielding of metal junctions due to combined shear and pressure. *Journal of the Mechanics and Physics of Solids*, 2, 197-211.
87. Griffiths, D. V. (1982). Computation of bearing capacity factors using finite elements. *Géotechnique* 32(3), 195-202.
88. Gzodev, A. (1960). Determination of the collapse load for statically determinate systems undergoing plastic deformations (Translation by R.M. Haythornthwaite). *Int. J. Mech. Sci.*, 1(4):332-335.

89. H.G. Poulos. (1988). *Marine Geotechnic*, Unwin Hyman, London.
90. Hagan MT, Menhaj MB (1994) Training feedforward networks with the Marquardt algorithm. *IEEE transactions on Neural Networks*, 5(6), 989-993
91. Hagan, M.T., Menhaj, M.B., 1994. Training feedforward networks with the Marquardt algorithm. *IEEE Trans. Neural Netw.* 5 (6), 989–993.
92. Hancock, J.T., Khoshgoftaar, T.M., 2020. CatBoost for big data: An interdisciplinary review. *J. Big Data*. 7, 94.
93. Hansen, B. (1970). A revised and extended formula for bearing capacity, *Bulletin of Danish Geotechnical Institute*, Copenhagen 28: 5-11.
94. Hataf, N., Razavi, M.R., 2003. Model test and finite element analysis of bearing capacity of ring footings on loose sand. *Iran J. Sci. Technol. Trans. B.* 27 (B1), 47–56.
95. Hossain, M.S., Hu, Y., Randolph, M.F., White, D.J., 2005. Limiting cavity depth for spudcan foundations penetrating clay. *Géotechnique*. 55(9), 679–690.
96. Houlsby, G., Martin, C., 2003 Undrained bearing capacity factors for conical foundations on clay. *Geotechnique* 53 (5), 513–520.
97. Houlsby, G.T., Puzrin, A.M., 1999. The bearing capacity of a strip footing on clay under combined loading. *Proc R Soc Lond Ser A* 455, 893–916.
98. Hu, P., Stanier, S.A., Wang, D., Cassidy, M.J., 2016. Effect of footing shape on penetration in sand overlying clay. *Int J Phys Model Geotech.* 16 (3), 119–133.
99. Huang, G., Wu, L., Ma, X., Zhang, W., Fan, J., Yu, X., Zeng, W., Zhou, H., 2019. Evaluation of CatBoost method for prediction of reference evapotranspiration in humid regions. *Journal of Hydrology*. 574, 1029-1041.
100. Ibrahim AS, Musa AA, Abdulfatah AY, Idris A (2022) Developing soft-computing regression model for predicting soil bearing capacity using soil index properties. *Modeling Earth Systems and Environment*, 9, 1223-1232
101. Ibsen, L.B., Barari, A., Larsen, K.A., 2014. Adaptive plasticity model for bucket foundations. *J. Eng. Mech.* 140, 361–373.
102. Jiang, Z. X., Xu, H. Y., Chen, H., Gao, B., Jia, S. J., Zhou, J., 2021. Indirect determination approach of blast-induced ground vibration based on a hybrid SSA optimized GP-based technique. *Advances in Civil Engineering*. 1–14.

103. Jitchaijaroen, W., Wipulanusat, W., Keawsawasvong, S., Chavda, J. T., Ramjan, S., Sunkpho, J., 2023. Stability evaluation of elliptical tunnels in natural clays by integrating FELA and ANN. *Results in Engineering*. 19, 101280.
104. Kaiser, M.J., 2017. The jackup rig construction market in the US gulf coast. *Ships Offshore Struct.* 12 (5), 662–678.
105. Kapadia D, Jariwala N (2021) Prediction of tropospheric ozone using artificial neural network (ANN) and feature selection techniques. *Modeling Earth Systems and Environment*, 8, 2183-2192
106. Karaboga, D., 2005. An idea based on honey bee swarm for numerical optimization. Technical Report-TR06, Department of Computer Engineering, Engineering Faculty, Erciyes University.
107. Keawsawasvong S, Ukritchon B (2016) Three-dimensional interaction diagram for the undrained capacity of inverted T-shape strip footings under general loading. *International Journal of Geotechnical Engineering*, 12(2), 133-146
108. Keawsawasvong, S. and Ukritchon, B. (2016). Finite element limit analysis of pullout capacity of planar caissons in clay. *Comput. Geotech.*, 75:12–17.
109. Keawsawasvong, S., 2022. Bearing capacity of conical footings on clays considering combined effects of anisotropy and non-homogeneity. *Ships. Offsh. Struct.* 1–12.
110. Keawsawasvong, S., Sangjinda, K., Jitchaijaroen, W., Alzabeebee, S., Suksiripattanapong, C., Sukkarak, R. (2023). Soft Computing-Based Models for Estimating the Ultimate Bearing Capacity of an Annular Footing on Hoek–Brown Material. *Arabian Journal for Science and Engineering*. 1–8.
111. Keawsawasvong, S., Shiau, J., Ngamkhanong, C., Lai, V.Q, Thongchom, C., 2022. Undrained stability of ring foundations: axisymmetry, anisotropy, and nonhomogeneity. *Int. J. Geomech.* 22 (1), 04021253.
112. Keawsawasvong, S., Ukritchon, B., 2016. Three-dimensional interaction diagram for the undrained capacity of inverted T-shape strip footings under general loading. *Int J Geotech Eng* 12 (2),133–146.
113. Keshavarz, A., Kumar, J., 2017. Bearing capacity computation for a ring foundation using the stress characteristics method. *Comput. Geotech.* 89 (9), 33–42.

114. Khatri, V.N., Kumar, J., 2009. Bearing capacity factor N (for a rough conical footing). *Geomech Eng.* 1 (3), 205–218.
115. Kim, B., Lee, D.E., Hu, G., Natarajan, Y., Preethaa, S., Rathinakumar, A. P., 2022. Ensemble machine learning-based approach for predicting of FRP–concrete interfacial bonding. *Mathematics.* 10 (2), 231.
116. Krabbenhoft K, Galindo-Torres SA, Zhang X, Krabbenhoft J (2019) AUS: Anisotropic undrained shear strength model for clays. *International Journal for Numerical and Analytical Methods in Geomechanics*, 43(17), 2652-2666
117. Krabbenhoft K, Lyamin A, Krabbenhoft J (2015) Optum computational engineering (OptumG2). Available on: www.optumce.com
118. Krabbenhoft, K. (2018). *OptumG2: theory*. Optum computational engineering. Copenhagen, Denmark.
119. Krabbenhoft, K., Galindo-Torres, S.A., Zhang, X., Krabbenhoft, J., 2019. AUS: Anisotropic undrained shear strength model for clays. *International Journal for Numerical and Analytical Methods in Geomechanics.* 43 (17), 2652-2666.
120. Krabbenhøft, K., Lyamin, A. V., and Sloan, S. W. (2008). Three-dimensional Mohr- Coulomb limit analysis using semidefinite programming. *Commun. Numer. Methods Eng.*, 24(11):1107-1119.
121. Krabbenhøft, K., Lyamin, A., and Krabbenhøft, J. (2015). *Optum computational engineering (OptumG2)*.
122. Kumar A, Chauhan VB, Kumar P (2023) Integration of AFELA and machine learning for analysis of shallow foundation over horseshoe tunnel in rock mass. *Modeling Earth Systems and Environment*
123. Kumar J, Ghosh P (2007) Ultimate bearing capacity of two interfering rough strip footings. *International Journal of Geomechanics*, 7, 53-62
124. Kumar M, Kumar V, Rajagopal BG, Samui P, Burman A (2023) State of art soft computing based simulation models for bearing capacity of pile foundation: a comparative study of hybrid ANNs and conventional models. *Modeling Earth Systems and Environment*, 9, 2533-2551
125. Kumar, B., Samui, P., 2008. Application of ANN for predicting pore water pressure response in a shake table test. *Int. J. Geotech. Eng.* 2, 153–160.

126. Kumar, D.R., Samui, P., Burman, A., 2022. Prediction of probability of liquefaction using hybrid ANN with optimization techniques. *Arabian Journal of Geosciences*. 12 (20), 1-21.
127. Kumar, D.R., Wipulanusat, W., Sunkpho, J., Keawsawasvong, S., Jitchaijaroen, W., Samui, P., 2024. Machine Learning Approaches for the Prediction of the Seismic Stability of Unsupported Rectangular Excavation. *Engineered Science*.
128. Kumar, J. and Chakraborty, M. (2014). Upper-bound axisymmetric limit analysis using the Mohr-Coulomb yield criterion, finite elements, and linear optimization. *J. Eng. Mech.*, 140(1982):06014012.
129. Kumar, J., Chakraborty, M., 2015. Bearing capacity factors for ring foundations. *J. Geotech. Geoenviron. Eng.* 141 (10), 06015007.
130. Kumar, J., Ghosh, P., 2005. Bearing capacity factor N_γ for ring footings using the method of characteristics. *Canadian Geotechnical Journal*. 42, 1474–1484.
131. Kumar, S., Kumar, D. R., Wipulanusat, W., & Keawsawasvong, S. (2024). Development of ANN-based metaheuristic models for the study of the durability characteristics of high-volume fly ash self-compacting concrete with silica fume. *Journal of Building Engineering*, 94, 109844.
132. Ladd CC, DeGroot DJ (2003) Recommended practice for soft ground site characterization. Arthur Casagrande Lecture. In *Proceedings of the 12th Panamerican Conference on Soil Mechanics and Geotechnical Engineering*, Cambridge
133. Ladd, C.C., 1991. Stability evaluations during stage construction. *Journal of Geotechnical Engineering*. 117 (4), 540–615.
134. Lai F, Zhang N, Liu S, Sun Y, Li Y (2021b). Ground movements induced by installation of twin large diameter deeply-buried caissons: 3D numerical modeling. *Acta Geotech* 1–29.
135. Lai VQ, Nguyen DK, Banyong R, Keawsawasvong S (2021a). Limit analysis solutions for stability factor of unsupported conical slopes in clays with heterogeneity and anisotropy. *Int J Comput Mater Sci Eng* 2150030.
136. Lai VQ, Shiao J, Promwichai T, Limkatanyu S, Banyong R, Keawsawasvong S (2023) Modelling soil stability in wide tunnels using FELA and multivariate adaptive regression splines analysis. *Modeling Earth Systems and Environment*, 9, 2993-3008

137. Law KT (1978) Undrained strength anisotropy in embankment stability analysis. *Canadian Geotechnical Journal*, 15(2), 306-309.
138. Le, L.T., Nguyen, H., Dou, J., Zhou, J., 2019. A comparative study of PSO-ANN, GA-ANN, ICA-ANN, and ABC-ANN in estimating the heating load of buildings' energy efficiency for smart city planning. *Applied Sciences*. 9 (13).
139. Lee, J.K., Jeong, S., Lee, S., 2016. Undrained bearing capacity factors for ring footings in
140. Li, A., Merifield, R., and Lyamin, A. (2009). Limit analysis solutions for three dimensional undrained slopes. *Comput. Geotech.*, 36(8):1330-1351.
141. Li, C., Ke, L., He, J., Chen, Z., Jiao, Y., 2019. Effects of mechanical properties of adhesive and CFRP on the bond behavior in CFRP-strengthened steel structures. *Composite Structures*. 211, 163-174.
142. Lim, K., Li, A., and Lyamin, A. (2015). Three-dimensional slope stability assessment of two-layered undrained clay. *Comput. Geotech.*, 70(2015):1-17.
143. Liu, M., Yang, M., Wang, H., 2014. Bearing behavior of wide-shallow bucket foundation for offshore wind turbines in drained silty sand. *Ocean Eng.* 82, 169–179.
144. Liu, M., Yang, M., Wang, H., 2014. Bearing behavior of wide-shallow bucket foundation for offshore wind turbines in drained silty sand. *Ocean Eng.* 82, 169–179.
145. Liu, R., Yuan, Y., Fu, D., Sun, G., 2021. Geotechnical capacities of large-diameter cylindrical foundations in clay under general loadings. *Appl. Ocean Res.* 117, 102951.
146. Lo, K.Y., 1965. Stability of slopes in anisotropic soils. *Journal of the Soil Mechanics and Foundation Division*. 31, 85-106.
147. Lysmer, J. (1970). Limit analysis of plane problems in soil mechanics. *J. Soil Mech. Found. Div.*, 96(4):1311-1334.
148. Makrodimopoulos, A. and Martin, C. M. (2007). Upper bound limit analysis using simplex strain elements and second-order cone programming. *Int. J. Numer. Anal. Methods Geomech.*, 31(6):835-865.
149. Mana, D.K.S., Gourvenec, S., Martin, C.M., 2013. Critical skirt spacing for shallow foundations under general loading. *J. Geotech. Geoenviron. Eng.* 139 (9), 1554–1566.

150. Marquardt, D.W., 1963. An algorithm for least-squares estimation of nonlinear parameters. *J. Soc. Ind. Appl. Math.* 11 (2), 431–441.
151. Martin CM (1994) Physical and numerical modelling of offshore foundations under combined loads. DPhil thesis, University of Oxford, UK
152. Martin CM, and Houlsby GT (2001) Combined loading of spudcan foundations on clay: numerical modelling. *Géotechnique*, 51(8), 687–699
153. Martin CM, Houlsby GT (2000) Combined loading of spudcan foundations on clay: Laboratory tests. *Geotechnique*, 50, 325-338
154. Martin, C. M. and Makrodimopoulos, A. (2008). Finite-element limit analysis of Mohr-Coulomb materials in 3D using semidefinite programming. *J. Eng. Mech.*, 134(4):339–347.
155. Meyerhof, G. G. (1953). The bearing capacity of foundations under eccentric and inclined loads. *Proc. 3rd Int. Conf. on Soil Mech. and Foundation Eng.*, Zurich, 1, 440-445.
156. Meyerhof, G. G. (1956). Rupture surfaces in sand under oblique loads (discussion), *Journal of soil mechanics*, ASCE 82(SM3).
157. Meyerhof, G. G. (1961). The ultimate bearing capacity of wedge shaped foundations. *Proc. 5th Int. Conf. on Soil Mech, and Foundation Eng.*, Paris, 2, 105-109.
158. Meyerhof, G. G. (1963). Some recent research on the bearing capacity of foundations. *Canadian Geotechnical Journal* 1(1), 16-26.
159. Mirjalili, S., 2015. The ant lion optimizer. *Adv. Eng. Softw.* 83, 80–98.
160. Mirjalili, S., Jangir, P., Saremi, S., 2017. Multi-objective ant lion optimizer: a multi-objective optimization algorithm for solving engineering problems. *Appl. Intell.* 46, 79–95.
161. Montrasio, L. & Nova, R. (1997). Settlements of shallow foundations on sand: geometrical effects. *Géotechnique* 47(1), 49-60.
162. Murff, J. D. 1994. Limit analysis of multi-footing foundation systems. *Proceedings of the 8th International Conference on Computer Methods and Advances in Geomechanics. Part 1 (of 4), May 22 - 28 1994. Morgantown, WV, United states: A.A. Balkema.*

163. Narasimhulu, N., Kumar, D.V.A., Kumar, M.V., 2020. LWT based ANN with ant lion optimizer for detection and classification of high impedance faults in distribution system. *J. Electr. Eng. Technol.* 15, 1631–1650.
164. Natekin, A., Knoll, A., 2013. Gradient boosting machines, a tutorial. *Front. Neurorob.* 7, 1–21.
165. Nayyeri, S., Hajali, M., Shdid, C.A., 2016. Ring foundation on elastic subgrade: An analytical solution for computer modelling using the Lagrangian multiplier method. *Int. J. Numer. Anal. Methods Geomech.* 40 (14), 2017–2030.
166. Nguyen, D.K., Nguyen, T.P., Keawsawasvong, S., Lai, V.Q., 2021. Vertical uplift capacity of circular anchors in clay by considering anisotropy and non-homogeneity. *Transp. Infrastruct. Geotechnol.*
167. Nguyen, D.K., Nguyen, T.P., Ngamkhanong, C., Keawsawasvong, S., Lai, V.Q., 2023. Bearing capacity of ring footings in anisotropic clays: FELA and ANN. *Neural Computing and Applications.* 1-22.
168. Nguyen, H.D., Lee, Y.J., LaFave, J.M., Shin, M., 2023. Seismic fragility analysis of steel moment frames using machine learning models. *Engineering Applications of Artificial Intelligence.* 126, 106976.
169. Nguyen, V.C., Keawsawasvong, S., Nguyen, D.K., Lai, V.Q., 2022. Machine learning regression approach for analysis of bearing capacity of conical foundations in heterogenous and anisotropic clays. *Neural Computing and Applications.* 35, 3955–3976.
170. Nova R, Montrasio L (1991) Settlements of shallow foundations on sand. *Géotechnique* 41(2), 243- 256
171. Pan Q, Dias D (2016) Face stability analysis for a shield-driven tunnel in anisotropic and nonhomogeneous soils by the kinematical approach. *International Journal of Geomechanics*, 6(3), 04015076
172. Panomchaivath, S., Jitchaijaroen, W., Banyong, B., Keawsawasvong, S., Sirimontree, S., Jamsawang, P., 2023. Prediction of undrained lateral capacity of free-head rectangular pile in clay using finite element limit analysis and artificial neural network. *Engineered Science.* 24, 923.
173. Pastor, J., Thai, T.-H., and Francescato, P. (2000). New bounds for the height limit of a vertical slope. *Int. J. Numer. Anal. Methods Geomech.*, 24(2):165–182.

174. Payan, M., Fathipour, H., Hosseini, M., Chenari, R.J., Shiau, J., 2022. Lower Bound Finite Element Limit Analysis of Geo-Structures with Non-Associated Flow Rule. *Computers and Geotechnics*. 147 (2), 104803.
175. Pedregosa, F., Varoquaux, G., Gramfort, A., Michel, V., Thirion, B., Grisel, O., Blondel, M., Prettenhofer, P., Weiss, R., Dubourg, V., Vanderplas, J., 2011. Scikit-learn: Machine learning in Python. *The Journal of machine Learning research*. 12, 2825-2830.
176. Phuor, T., Harahap, I.S., Ng, C-Y., 2022. Bearing capacity factors for rough conical foundation by viscoplasticity finite-element analysis. *Int. J. Geomech* 22 (1), 04021266.
177. Pradeep, T., Bardhan, A., Samui, P.. 2021. Prediction of rock strain using soft computing framework. *Innovative Infrastructure Solutions*. 7(1), 1–24.
178. Prandtl, L. (1921). *Über die eindringungsfestigkeit plastischer baustoffe und die festigkeit von schneiden*. *Proceedings of the Royal Society of London. Series A, Mathematical and Physical Sciences*, 233, 267-287.
179. Prokhorenkova, L., Gusev, G., Vorobev, A., Dorogush, A.V., Gulin, A., 2018. CatBoost: Unbiased boosting with categorical features. *Adv. Neural Inf. Process. Syst.* 31, 6638–6648.
180. Qi, C., Fourie, A., Zhao, X., 2018. Back-analysis method for slope displacements using gradient-boosted regression tree and firefly algorithm. *J. Comput. Civ. Eng.* 32 (5), 04018031.
181. Qi, C., Fourie, A., Zhao, X., 2018. Back-analysis method for slope displacements using gradient-boosted regression tree and firefly algorithm. *J. Comput. Civ. Eng.* 32 (5), 04018031.
182. Qi, C., Tang, X., 2018. Slope stability prediction using integrated metaheuristic and machine learning approaches: a comparative study. *Comput. Ind. Eng.* 118, 112–122.
183. Rabi, M., Ferreira, F.P.V, Abarkan, I., Limbachiya, V., Shamass, R., 2023. Prediction of the cross-sectional capacity of cold-formed CHS using numerical modelling and machine learning. *Results in Engineering*. 17, 100902.
184. Randolph, M. F. & Puzrin, A. M. 2003. Upper bound limit analysis of circular foundations on clay under general loading. *Geotechnique*, 53, 785-796.

185. Randolph, M. F., Cassidy, M. J., Gourvenec, S. & Erbrich, C. 2005. Challenges of offshore geotechnical engineering. International symposium on frontiers in offshore geotechnics. Perth.
186. Reddy AS, Rao KV (1981) Bearing capacity of strip footing on anisotropic and nonhomogeneous clays. *Soils and Foundations*, 21(1), 1-6
187. Reddy, Y.R., 2017. Applications of artificial intelligence and machine learning in geotechnical engineering. *Int. J. Emerg. Technol. Innov. Res.* 2349–5162.
188. Remadna, M.S., Benmebarek, S., Benmebarek, N., 2017. Numerical evaluation of the bearing capacity factor N_c of circular and ring footings. *Geomechanics and Geoengineering*. 12 (1), 1–13.
189. Roe, B.P., Yang, H., Zhu, J., et al., 2005. Boosted decision trees as an alternative to artificial neural networks for particle identification. *Nucl. Instrum. Methods Phys. Res., Sect. A* 543 (2), 577–584.
190. Roscoe KH, Schofield AN (1957) The stability of short pier foundations in sand: discussion. *Br. Weld. J*, January, 12–18
191. Saha, M.C., 1978. Ultimate bearing capacity of ring footings on sand. M.Eng. Thesis. UP, University of Roorkee, India.
192. Saint-Fleur BE, Allier S, Lassara E (2023) Towards a better consideration of rainfall and hydrological spatial features by a deep neural network model to improve flash floods forecasting: case study on the Gardon basin, France. *Model. Earth Syst. Environ*, 9, 3693–3708
193. Salencon, J., Pecker, A., 1995. Ultimate bearing capacity of shallow foundations under inclined and eccentric loads. Part I: purely cohesive soil. *Eur J Mech A/Solids* 14 (3), 349–375.
194. Sangjinda, K., Kumar, D. R., Keawsawasvong, S., Wipulanusat, W., Jamsawang, P., 2024. Novel neural network-based metaheuristic models for the stability prediction of rectangular trapdoors in anisotropic and non-homogeneous clay. *Advances in Engineering Software*. 193, 103668.
195. Schapire, R.E., 2003. The Boosting Approach to Machine Learning: An Overview. *Nonlinear Estimation and Classification*. Springer, New York, pp. 149–171.

196. Shams SR, Jahani A, Moeinaddini M, Khorasani N (2020) Air carbon monoxide forecasting using an artificial neural network in comparison with multiple regression. *Modeling Earth Systems and Environment*, 6, 1467-1475
197. Shen, Z., Feng, X., Gourvenec, S., 2016. Undrained capacity of surface foundations with zero-tension interface under planar V-H-M loading. *Comput. Geotech.* 73, 47–57.
198. Shen, Z., Feng, X., Gourvenec, S., 2017. Effect of interface condition on the undrained capacity of subsea mudmats under six-degree-of-freedom loading. *Geotechnique* 67 (4), 338–349.
199. Sheridan, R.P., Wang, W.M., Liaw, A., Ma, J., Gifford, E.M., 2016. Extreme gradient boosting as a method for quantitative structure–activity relationships. *Journal of chemical information and modeling*, 56 (12), 2353-2360.
200. Shiau, J., Al-Asadi, F., 2023. Stability analysis of twin circular tunnels using shear strength reduction method. *Géotechnique Letters* 10 (2), 311-319.
201. Shiau, J., Keawsawasvong, S., 2022. Producing undrained stability factors for various tunnel shapes. *International Journal of Geomechanics* 22 (8), 06022017.
202. Shiau, J., Keawsawasvong, S., Yodsomjai, W., 2023. Determination of support pressure for the design of square box culverts. *International Journal of Geomechanics* 23 (1), 06022035.
203. Shiau, J., Lai, V.Q., Keawsawasvong, S., 2022. Multivariate adaptive regression splines analysis for 3D slope stability in anisotropic and heterogenous clay. *J. Rock Mech. Geotech. Eng.*
204. Shiau, J., Sams, A., Al-Asadi, F., Hassan., M.M., 2018. Stability charts for unsupported plane strain tunnel headings in homogeneous undrained clay, *GEOMATE Journal* 14 (41), 19-26
205. Shiau, J.S., Yu, H.S., 2000. Shakedown analysis of flexible pavements, *Proc. of the John Booker Memorial Symposium* (ed DW Smith & JP Carter), 643-653
206. Shield, R. T. (1955). On the plastic flow of metals under conditions of axial symmetry. *Proc. Royal Soc. London, Series A*, 233, 267-287.

207. Sirimontree, S., Keawsawasvong, S., Ngamkhanong, C., Seehavong, S., Sangjinda, K., 2022. Neural network-based prediction model for the stability of unlined elliptical tunnels in cohesivefrictional soils. *Buildings*. 12 (4), 444.
208. Sloan, S. and Kleeman, P. (1995). Upper bound limit analysis using discontinuous velocity fields. *Comput. Methods Appl. Mech. Eng.*, 127(1-4):293–314.
209. Sloan, S.W., 2013. Geotechnical stability analysis. *Géotechnique*. 263 (7), 531–572
210. Su SF, Liao HJ, Lin YH (1998) Base stability of deep excavation in anisotropic soft clay. *Journal of Geotechnical and Geoenvironmental Engineering*, 124(9), 809–819
211. Tadayon, A., Eslami, A., Fakharian, K., 2024. Geotechnical behavior of conical and skirted foundations through experimental and numerical assessment. *Transportation Infrastructure Geotechnology*.
212. Taiebat HA, Carter JP (2002) Bearing capacity of strip and circular foundations on undrained clay subjected to eccentric loads. *Ge´otechnique*, 52(1), 61–64
213. Taiebat, H. A., Carter, J.P., 2000. Numerical studies of the bearing capacity of shallow foundations on cohesive soil subjected to combined loading. *Géotechnique* 50 (4), 409–418.
214. Taiebat, H. A., Carter, J.P., 2010. A failure surface for circular footings on cohesive soils. *Géotechnique* 60 (4), 265–273.
215. Tan, F. S. C. (1990). Centrifuge and theoretical modelling of conical footings on sand, University of Cambridge, U. K.
216. Tan, F.S., 1990. Centrifuge and theoretical modelling of conical footings on sand. PhD thesis, Cambridge University, UK.
217. Taylor, K.E., 2001. Summarizing multiple aspects of model performance in a single diagram. *Journal of Geophysical Research: Atmospheres*. 106 (D7), 7183–7192.
218. Terzaghi, K. (1943). *Theoretical Soil Mechanics*, John Wiley & Sons, Inc.
219. Touzani, S., Granderson, J., Fernandes, S., 2018. Gradient boosting machine for modeling the energy consumption of commercial buildings. *Energy Build.* 158, 1533–1543.

220. Tran, D.T., Onjaipurn, T., Kumar, D.R., Chim-Oye, W., Keawsawasvong, S., Jamsawang, P., 2024. An eXtreme Gradient Boosting prediction of uplift capacity factors for 3D rectangular anchors in natural clays. *Earth Science Informatics*.
221. Tran, D.T., Tran, M.N., Lai, V.Q., Keawsawasvong, S., 2023. Advanced FELA-ANN framework for developing 3D failure envelopes for strip foundations on anisotropic clays. *Model. Earth Syst. Environ.* 10 (2), 2375–2392.
222. Ukritchon B, Keawsawasvong S (2020) Undrained lower bound solutions for end bearing capacity of shallow circular piles in non-homogeneous and anisotropic clays. *Int. J. Numer. Anal. Meth. Geomech.* 44(5), 596–632.
223. Ukritchon B, Whittle AJ, Sloan SW (1998) Undrained limit analysis for combined loading of strip footings on clay. *J. Geotech. Geoenviron. Engng ASCE*, 124(3), 265–276
224. Ukritchon B, Whittle AJ, Sloan SW (2003) Undrained stability of braced excavations in clay. *Journal of Geotechnical and Geoenvironmental Engineering*, 129(8), 738–755
225. Ukritchon, B. and Keawsawasvong, S. (2016). Undrained pullout capacity of cylindrical suction caissons by finite element limit analysis. *Comput. Geotech.*, 80(9):301–311.
226. Ukritchon, B., Keawsawasvong, S., 2020. Undrained lower bound solutions for end bearing capacity of shallow circular piles in non-homogeneous and anisotropic clay. *International Journal for Numerical and Analytical Methods in Geomechanics*. 44 (5), 596-632.
227. Vesic AS (1975) Bearing capacity of shallow foundations. H. F. Winterkorn & H. Y. Fang (eds), *Foundation Engineering Handbook*, Van Nostrand, New York, 121–147
228. Vulpe C, Bienen B, Gaudin C (2013) Predicting the undrained capacity of skirted spudcans under combined loading. *Ocean Engng*, 74, 178–188
229. White, D.J., The, K.L., Leung, C.F., Chow, Y.K., 2008. A comparison of the bearing capacity of flat and conical circular foundations on sand. *Géotechnique*. 58 (10), 781–792.
230. Willmott, C. J., 1984. On the evaluation of model performance in physical geography. *Spatial Statistics and Models*. 443–460.

231. Xiao, Y., Zhao, M., Zhao, H., 2018. Undrained stability of strip footing above voids in two-layered clays by finite element limit analysis. *Computers and Geotechnics*. 97, 124-133
232. Yang XL, Du DC (2016) Upper bound analysis for bearing capacity of nonhomogeneous and anisotropic clay foundation. *KSCE Journal of Civil Engineering*, 20(7), 2702-2710
233. Yang, H., Shen, Z., and Wang, J. (2003). 3D lower bound bearing capacity of smooth rectangular surface footings. *Mech. Res. Commun.*, 30(5):481–492.
234. Yodsomjai, W., Keawsawasvong, S., Lai, V.Q., 2021a. Limit analysis solutions for bearing capacity of ring foundations on rocks using Hoek–Brown failure criterion. *Int. J. Geosynth. Ground. Eng.* 7 (2), 29.
235. Yodsomjai, W., Keawsawasvong, S., Senjuntichai, T., 2021b. Undrained stability of unsupported conical slopes in anisotropic clays based on AUS failure criterion. *Transportation Infrastructure Geotechnology*. 8 (3).
236. Yu, H. S., Sloan, S. W., and Kleeman, P. W. (1994). A quadratic element for upper bound limit analysis. *Eng. Comput.*, 11(3):195–212.
237. Yu, L., Yang, Q., Zhang, J., 2018. Undrained bearing capacity of irregular T-bar by the lower bound method in clay. *Applied Ocean Research*. 105 (12), 102409.
238. Yun, G., Bransby, M.F., 2007. The horizontal-moment capacity of embedded foundations in undrained soil. *Can. Geotech. J.* 44(4), 409–424.
239. Zhang W (2019) *MARS applications in geotechnical engineering systems*. Springer, Beijing.
240. Zhang W, Li Y, Wu C, Li H, Goh ATC, Liu H (2020) Prediction of lining response for twin tunnels constructed in anisotropic clay using machine learning techniques. *Undergr Space*.
241. Zhang W, Zhang R, Goh ATC (2018) MARS inverse analysis of 954 soil and wall properties for braced excavations in clays. *Geomech Eng* 16(6):577–588.
242. Zhang W, Zhang Y, Goh ATC (2017) Multivariate adaptive regression splines for inverse analysis of soil and wall properties in braced excavation. *Tunn Undergr Sp Tech* 64:24–33.

243. Zhang Y, Bienen B, Cassidy MJ, Gourvenec S (2011) The undrained bearing capacity of a spudcan foundation under combined loading in soft clay. *Marine Struct*, 24(4), 459–477
244. Zhang, H., Chen, L., Wei, Z.Q., 2020. Abnormal Traffic Detection Technology Based on Data Augmentation and Model Update. *Netinfo Secur.* 20, 66–74.
245. Zhang, P., Jin, Y., Yin, Z., Yang, Y., 2020. Random forest based artificial intelligent model for predicting failure envelopes of caisson foundations in sand. *Appl. Ocean Res.* 101, 102223.
246. Zhang, R., Zhao, H., Wu, G., 2022. FELA investigation of eccentrically-loaded footing on parallel tunnels constructed in rock masses. *Computers and Geotechnics.* 153: 105102.
247. Zhao, L., Wang, J.H., 2008. Vertical bearing capacity for ring footings. *Computers and Geotechnics.* 35, 292–304.
248. Zhao, Z, Zhang, H, Shiau, J, Du, W, Ke, L, Wu, F, Bao, X. 2024. Failure envelopes of rigid tripod pile foundation under combined vertical-horizontal-moment loadings in clay. *Applied Ocean Research*, 150, 104131.
249. Zhao, Zihao, Zhang, Hao, Ke, Lijun, Zhao, Guoqing, Meng, Suyun, Wu, Fengyuan and Shiau, Jim. 2022. Effect of loading eccentricity on the ultimate lateral resistance of twin-piles in clay. *Soils and Foundations.* 62 (2), pp. 1-14.
250. Zhou H, Xu H, Yu X, Guo Z, Zheng G, Yang X (2021) Evaluation of the bending failure of columns under an embankment loading. *Int J Geomech* 21(7):04021112
251. Zhou, J., Asteris, P. G., Armaghani, D. J., Pham, B., 2020. Prediction of ground vibration induced by blasting operations through the use of the bayesian network and random forest models. *Soil Dynamics and Earthquake Engineering*, 139, Article 106390.
252. Zhou, J., Li, E., Wang, M., Chen, X., Shi, X., Jiang, L., 2019. Feasibility of stochastic gradient boosting approach for evaluating seismic liquefaction potential based on SPT and CPT case histories. *J. Perform. Constr. Facil.* 33 (3), 04019024.
253. Zhou, J., Li, X., Mitri, H.S., 2015. Comparative performance of six supervised learning methods for the development of models of pillar stability. *Nat. Hazards* 79 (1), 291–316.

254. Zhou, J., Li, X., Mitri, H.S., 2016. Classification of rockburst in underground projects: comparison of ten supervised learning methods. *J. Comput. Civ. Eng.* 30 (5), 04016003.
255. Zhuang, J., Yin, Z., Kotronis, P., Li, Z., 2019. Advanced numerical modelling of caisson foundations in sand to investigate the failure envelope in the H-M-V space. *Ocean Eng.* 190, 106394.



BIOGRAPHY

Name	DUY TAN TRAN
Date of Birth	April 08, 1996
Educational Attainment	<p>Academic Year 2019: Bachelor Degree of Civil Engineering, Ho Chi Minh City University of Transport, Vietnam</p> <p>Academic Year 2022: Master Degree of Civil Engineering, Ho Chi Minh City University of Technology, Vietnam</p> <p>Academic Year 2025: Doctor Degree of Civil Engineering, Thammasat University, Thailand</p>

Publications

Tran, D.T., Tran, M.N., Lai, V.Q., Keawsawasvong, S., 2024. Advanced FELA-ANN framework for developing 3D failure envelopes for strip foundations on anisotropic clays. *Modeling Earth Systems and Environment* 10: 2375–2392.

Tran, D.T., Shiau, J., Kumar, D.R., Lai, V.Q., Keawsawasvong, S., 2025. Optimization of ANN using metaheuristic algorithms for predicting failure envelope of ring foundations on anisotropic clay. *Applied Ocean Research* 154: 104375

Tran, D.T., Shiau, J., Lai, V.Q., Keawsawasvong, S., 2025. Stability of conical foundations on anisotropic clay: A comprehensive three-dimensional study on V-H-M failure envelopes. *Computers and Geotechnics* 177: 106906.

Tran, D.T., Shiau, J., Keawsawasvong, S., Jamsawang, P., 2025. Developing failure envelopes of strip anchors under combined V-H-M loadings using FELA and ADABOOST models. *Ocean Engineering* 320: 120305.

Tran, D.T., Shiau, J., Keawsawasvong, S., Jamsawang, P., 2024. Failure envelopes of embedded foundations under V-H-M loadings in anisotropic clays using optimised ANFIS algorithms. *Marine Georesources & Geotechnology*.

Tran, D.T., Keawsawasvong, S., Kumar, J., 2023. Stability Charts for Limiting Horizontal Normal Pressure on Cohesive–Frictional Backfill for Deep Contiguous I-Shaped Piled Walls. *International Journal of Geosynthetics and Ground Engineering* 9: 44.

Tran, D.T., Onjaipurn, T., Kumar, D.R., Chim-Oye, W., Keawsawasvong, S., Jamsawang, P., 2024. An eXtreme Gradient Boosting prediction of uplift capacity factors for 3D rectangular anchors in natural clays. *Earth Science Informatics* 17: 2027–2041.

Tran, D.T., Kumar, D.R., Keawsawasvong, S., Wipulanusat, W., Jamsawang, P., 2024. Innovative approaches for predicting seismic stability of circular and rectangular tunnels in cohesive-frictional soils using machine learning and finite element limit analysis. *Modeling Earth Systems and Environment*.

Domphoeun, R., Tran, D.T., Keawsawasvong, S., Jamsawang, P., 2024. Coupling 3DFELA with XGBoost Model for Undrained Stability Prediction of Supported Rectangular Excavations in Anisotropic Clays. *International Journal of Geosynthetics and Ground Engineering* 10: 76.

Promwichai, T., Tran, D.T., Nguyen, T.S., Keawsawasvong, S., Jamsawang, P., 2025. Probabilistic analysis of the bearing capacity of spatially random Hoek–Brown rock masses by integrating finite element limit analysis, random field theory, and XGBoost models. *Earth Science Informatics* 18: 33.